Characterization of Strain in Core-Shell Nanowires:

A Raman Spectroscopic Study

by

Rachna Singh

A Dissertation Presented in Partial Fulfillment
of the Requirements for the Degree
Doctor of Philosophy

Approved September 2011 by the
Graduate Supervisory Committee:

José Menéndez, Chair
Jeffery Drucker
Fernando Ponce
Kong-Thon Tsen
Peter Bennett

ARIZONA STATE UNIVERSITY

December 2011

ABSTRACT

Raman scattering from Ge-Si core-shell nanowires is investigated theoretically and experimentally. A theoretical model that makes it possible to extract quantitative strain information from the measured Raman spectra is presented for the first time. Geometrical and elastic simplifications are introduced to keep the model analytical, which facilitates comparison with experimental results. In particular, the nanowires are assumed to be cylindrical, and their elastic constants isotropic. The simple analytical model is subsequently validated by performing numerical calculations using realistic nanowire geometries and cubic, anisotropic elastic constants. The comparison confirms that the analytic model is an excellent approximation that greatly facilitates quantitative Raman work, with expected errors in the strain determination that do not exceed 10%.

Experimental Raman spectra of a variety of core-shell nanowires are presented, and the strain in the nanowires is assessed using the models described above. It is found that all structures present a significant degree of strain relaxation relative to ideal, fully strained Ge-Si core-shell structures. The analytical models are modified to quantify this strain relaxation.

DEDICATION

For

Spriha and Kamesh

ACKNOWLEDGMENTS

I express my sincerest gratitude to my advisor, Prof. José Menéndez, for his invaluable assistance, support and guidance in this research. Prof Menendez's enthusiasm and aspiration for last four years has helped me to perform this research. I hope to emulate his abilities in my forthcoming research career.

On a personal note, I would like to thank Dr. Christian Powelleit, for assisting in the necessary Raman training. He has been a source of constant encouragement.

I express my deepest gratitude to Prof. Jeff Drucker and his team members especially Dr Eric Dailey of ASU for sample preparation and the computer simulations without which this research wound not have been successful. I would also like to thank Prof. Fernando Ponce, Prof. Peter Bennett and Prof. Kong-Thon Tsen for being in my committee and supporting me.

I would like to thank all my graduate students especially Xiang Chen, Hermann Azemtsa Donfack, and Somilkumar Rathi for their discussions and support.

Last but not the least I would like to thank Spriha and Kamesh for their constant support and encouragement.

TABLE OF CONTENTS

Page

CHAPTER Page

CHAPTER Page

APPENDIX Page

LIST OF TABLES

LIST OF FIGURES

Figure Page

INTRODUCTION

1.1 Background on nanowires

Work in the field of Nanotechnology has been done for centuries, but only recently a few areas of this field have been recognized. In 1857 Michael Faraday[1] performed one of the first experiments with nanoparticles. He examined the interaction of light with gold colloids and also observed the ruby color of the colloids. In 1985, Turkevich J. found that the average size of the gold colloids was 6 ± 2 nm.[2] Michael Faraday's observation was presumably the first scientific observation and introduction to quantum size effects.

Over the past few decades scientists have made impressive progress in the research of semiconductor nanostructures, by progressing from the study of the electronic, optical and transport properties of bulk semiconductors to the analysis of the same properties in reduced size systems. Examples include two dimensional quantum-well systems, one dimensional nanowire and zero dimensional quantum dots.

Semiconducting nanowires are nowadays attractive for nanoscience[3,4] research along with nanotechnology[5,6,7] applications. Compared with other nanosize materials, nanowires have two quantum confined directions with one unrestrained direction.[3] Quantum confinement in the nanowire causes the energy levels to be

different from the traditional continuum of energy bands found in bulk materials. Accordingly, in the limit of small diameters nanowires are observed to exhibit different optical, electrical, and magnetic properties relative to their bulk counterparts. The unique properties of nanowires also hold promise from an application perspective because some of the material's parameters can be independently restrained or enhanced non–linearly.

Nanowires are mostly synthesized by a bottom–up fabrication technique. Vapor–Liquid–Solid (VSL) is one of the most popular growth methods. In 1964, Wager and Eliss[8,9] first fabricated micrometer–sized Si whiskers from the Vapor–Liquid–Solid(VSL). The VSL technique has now become a widely used method for generating semiconductor nanowires from a wide variety of pure elemental semiconductors[10,11,12](group IV) to III–V[13,14,15] semiconductors.

In the late 1980s, Wharam[16] and Wees[17] researched the electronic transport properties of nanowires and found that if the nanowire's diameter is comparable to the Fermi wavelength of the electron, the conductance is quantized and each quantum state contributes an integral number of $2e^2/\hbar$ to the electrical conductance. The study of thermoelectric properties started as early as 1993 by Hicks *et. al..*[18,19] Both theoretically[20] and experimentally[21] it was shown that lattice thermal conductivity decreased by more than 90%, a

significant advantage for thermoelectricity, which is characterized by the figure of merit $ZT = \sigma S^2 T / \kappa$ where S is the Seebeck Coeffecient, T is the average temperature, σ is the electrical conductivity and κ is the thermal conductivity. Bi nanowires became an important material to study the magneto resistive properties of nanowires. In 2000, the Dresselhaus[22] group performed extensive study on the nanowire's magneto resistance properties. Recent research[23] shows that magneto resistivity is similar to electric resistance at low temperatures. The research of transport properties also took place at same time. Studies of the optical properties[24] of nanowires have shown that if the wire's diameter is less than the effective Bohr radius, excitonic behavior can be observed at room temperature in the photoluminescence or absorption peak spectra. Therefore recent studies have demonstrated the potential for nanowires to achieve new and useful properties and to advance the nanowire applications.

At the beginning of 21st century researchers started to fabricate nanowire electronic devices, diodes, transistors, logic gates etc. and realized that nanowires can be used in miniaturization of conventional devices in a cost–effective way. Over the last ten years, researchers have shown tremendous progress in the development of nanowires for applications in nanoelectronics. One of the first functional nanoscale devices was fabricated by Cui *et al.*[25] Te and Zn doped n and p – type

Indium phosphide nanowires were used to assemble $p-n$ junction diodes. Later Cui *.et al.*[26] assembled passive $p-n$junction diodes, bipolar transistors and inverter-like nanostructures from boron and phosphorous doped silicon nanowires. Gallium Nitride(GaN) nanowires were next used by Huang *et al*[27] and Kim *et al*[28] to develop nanoscale devices which lead to the fabrication of Nanowire FETs and Schottky diodes from a single crystal of GaN nanowire. During the last five years, IBM[29,30,31,32] has carried out extensive research in the formulation of nanoelectronics based on nanowires. One of their major advances is the construction of different Nanowire FET architectures[29,30,31,32] which has led to the realization that the performance of nanowire FETs depend largely on their diameter. It has been found that nanowires with small diameters show better device functionality and performance. A nanowire thermoelectric device was first demonstrated by Li *et al.,*[33] who suggested an array of Silicon nanowires with low thermal conductivity, which would help in fabrication of cooling and energy–harvesting ICs. In 2008 it was found that etched Silicon nanowires[34] have enhanced thermoelectric performance and hence have potential for applications in thermoelectric cooling processes. Nanowires also hold promise in the fabrication of optoelectronic devices.[35,36]

In an era of developing technology, nanowire hetrostructures[37] evolved in the early 21st century and are now being fabricated in industry. With the development of hetrostructures, the issue of strain in nanowires[38] was introduced. In the literature, stress–strain studies are mostly restricted to simple nanowires. Sadowski[39] et. al. have done comprehensive ab initio study to analyze the uniaxial strain effect on the nanowire and Liang[40] *et al.* studied strain in Si-Ge core-shell structures with the assumption of similar elastic constants for both core and shell. Recently Søndergaard[41] et. al. calculated the strain field in GaP core and GaAs shell nanowires using the continuum elasticity theory. A more detailed work has been presented by Grönqvist[42] et. al.. Grönqvist[42] et. al., computed the strain field distributions in the core-shell nanowire using both the continuum theory of elasticity and valence field force model.

1.2 Motivation

Core-shell semiconductor nanowires open up interesting opportunities for their potential applications in nanoelectronics and nanooptics.[6,43,44,45] A significant characteristic of these structures is the presence of large strains developed due to lattice mismatch between the core and shell materials.[46,41,42,47] Strain modifies the phonon frequencies in anharmonic crystal lattices, which can then be used to

monitor the strain spectroscopically, mainly via Raman scattering. However, the methodology to extract strain values from core-shell nanowires spectroscopic measurements is not yet established. The strain tensors from the core-shell nanowires have complex symmetries and are position-dependent. Raman spectroscopy is potentially a useful tool for the study of strain in nanowires because of it can be applied in various environments and geometries.[48] It also provides a simple, quick, non-destructive approach to study the vibrational properties of the nanowire with a good spatial resolution. Unfortunately, extracting strain values from Raman measurements on nanowires are far more complex than using Raman spectroscopy to measure strain in epitaxial two-dimensional films— a traditional application for which the Raman approach to the determination of strain is well established. A preliminary strain study has been conducted by Laneuville[49] et. al. who used Raman spectroscopy on single nanowire and then estimated the strain exerted by the AlN shell on the GaN core using a simplified model that neglects the in-plane strain. In general, we found a lack of realistic, quantitative studies of strain in nanowires heterostructures using micro-Raman spectroscopy. This was the main motivation to study the vibrational properties of semiconductor nanowires, with emphasis on using micro-Raman spectroscopy as a method to analyze strain effects in core-shell

nanowires both experimentally and theoretically. In this dissertation we develop a continuum model of the strain and compare it with realistic computer simulations using the commercial package ABAQUS. The next step was to develop the theory of the strain-dependent modifications of optical phonons of semiconductors, which was later adapted to the case of core-shell nanowires. Finally, Raman spectra of the nanowires were computed and analyzed in terms of scattering selection rules. The theoretical results were then compared with the micro-Raman experimental results with emphasis on strain relaxation.

1.3 Dissertation Outline

Chapter 2 introduces the basic elasticity theory of solids. It is followed by the discussion of strain effects in core-shell nanowires. Sections 2.3 and 2.4 describe a more realistic solution of the core–shell nanowire. In these sections some of the assumptions of the Section 2.2 are removed and a relaxation term is introduced.

Chapter 3 starts with a review of lattice vibrations. Section 3.2-3.4 describes the classical, semi classical and quantum theory of Raman scattering. In the latter two sections Raman selection rules and the experimental set-up are described.

Chapter 4 discusses a simplified continuum model of the core-shell nanowire. Section 4.1 deals with the problem of optical phonon in <110>- and <111>-oriented nanowires. The latter sections describe the simulations of the Raman spectra due to strain effect in nanowires with different polarizations.

Chapter 5 discusses the strain predicted by the numerical method with the strain obtained from our analytical model, and later we compute the Raman spectrum corresponding to the numerical strain model by averaging over the nanowire cross section.

Chapter 6 discusses the experimental Raman data on the nanowires and compares with the predictions from the analytical strain model that includes the strain relaxation term.

Chapter 7 summarizes the results of strain effects on Raman spectra of core-shell nanowire.

CHAPTER 2

STRAIN EFFECTS IN CORE-SHELL NANOWIRE

2.1 Introduction

The strain distribution[47] in core–shell nanowires can be computed analytically under the assumption of isotropic elastic properties and cylindrical geometry. Within the isotropic material and cylindrical geometry approximations, the solution of the elastic problem represented by core-shell nanowires is a variant of the standard "shrink-fit" problem discussed in elasticity textbooks. Liang *et al.*[40] used this approach to solve the Si-Ge core-shell elastic problem under the assumption that the average Young modulus E and average Poisson ratio ν are the same for both materials. Liang's approximation is too crude for Raman calculations, so we extend their model by assigning the different Si and Ge Young moduli. The Poisson ratio is kept the same, since the ratios of elastic constants are nearly the same for Si and Ge, and hence their corresponding Poisson ratios are very similar for any arbitrary crystallographic orientation.

2.2 Review of theory of elasticity in solids

Deformations[50] in solid structures are caused when stress is applied. Hooke's Law gives a proportionality relation between stress and

deformation. It states that when the deformation is in the elastic limit, the strain ε is directly proportional to the stress, which is given by

$$\sigma = c\varepsilon, \tag{2.1}$$

where c is the elastic stiffness constant.

The generalized form of Hooke's law is given by

$$\sigma_{ij} = \sum_{kl} c_{ijkl}\varepsilon_{kl}, \tag{2.2}$$

where σ_{ij} and ε_{kl} are the components of the stress and strain tensors, respectively and the c_{ijkl} denote the 81 components of the elastic stiffness fourth-order tensor. Since the stress as well as the strain tensors are symmetric, it follows that

$$c_{ijkl} = c_{jikl} = c_{ijlk} = c_{jilk}. \tag{2.3}$$

When a unit volume deforms by differential amounts $d\varepsilon_j$, the free energy change due to the work done by the stresses on the element is expressed as

$$dF = dW = \sum_{i} \sigma_{ij} d\varepsilon_{ij} = \sum_{ij}\sum_{kl} c_{ijkl}\varepsilon_{kl} d\varepsilon_{ij}. \tag{2.4}$$

Thus

$$\frac{\partial^2 F}{\partial\varepsilon_{ij}\partial\varepsilon_{kl}} = c_{ijkl}. \tag{2.5}$$

Since the free energy is a state function, the order of the derivatives is immaterial, and therefore

$$c_{ijkl} = c_{klij}. \tag{2.6}$$

The permutation of the first and last two suffixes of c_{ijkl} make it possible to introduce a contracted index notation such that $c_{ijkl} = c_{mn}$, with the following correspondence:

Table(2.1): Relationship between four-index and contracted notation.

ij or kl	11	22	33	23,32	31 ,13	12 ,21
m or n	1	2	3	4	5	6

Moreover, because of the symmetries in Eq.(2.3), we can identify 7 with 4, 8 with 5, and 9 with 6, so that Eq. (2.2) can be written in matrix form as

$$\begin{pmatrix} \sigma_{11} \\ \sigma_{22} \\ \sigma_{33} \\ \sigma_{23} \\ \sigma_{13} \\ \sigma_{12} \end{pmatrix} = \begin{pmatrix} c_{11} & c_{12} & c_{13} & c_{14} & c_{15} & c_{16} \\ c_{12} & c_{22} & c_{23} & c_{24} & c_{25} & c_{26} \\ c_{13} & c_{23} & c_{33} & c_{34} & c_{35} & c_{36} \\ c_{14} & c_{24} & c_{34} & c_{44} & c_{45} & c_{46} \\ c_{15} & c_{25} & c_{35} & c_{45} & c_{55} & c_{56} \\ c_{16} & c_{26} & c_{36} & c_{46} & c_{65} & c_{66} \end{pmatrix} \begin{pmatrix} \varepsilon_{11} \\ \varepsilon_{22} \\ \varepsilon_{33} \\ 2\varepsilon_{23} \\ 2\varepsilon_{13} \\ 2\varepsilon_{12} \end{pmatrix}. \qquad (2.7)$$

This 6x6 symmetric matrix has 21 independent constants. Hence in matrix notation, we can rewrite Hooke's law as

$$\sigma_i = \sum_j c_{ij}\varepsilon_j \quad (i, j = 1,2.....6), \qquad (2.8)$$

where σ_i and ε_i are the reduced form of stress and strain in the 6×6 matrix.

Additional reductions in the number of independent constants can be obtained from crystal symmetry considerations. The coordinate

transformation equation for the stress and strain components is expressed as

$$\sigma'_{mn} = \sum_{ij} l_{im} l_{jn} \sigma_{ij} \tag{2.9}$$

and

$$\varepsilon'_{mn} = \sum_{ij} l_{im} l_{jn} \varepsilon_{ij}, \tag{2.10}$$

where l_{ij}'s, are the direction cosines between the $(x_1, x_2, x_3) \rightarrow unprimed$ and $(x'_1, x'_2, x'_3) \rightarrow primed$ coordinate system If the inverse transformation equation of Eq.(2.9) is substituted into Eq.(2.2), we obtain

$$\sum_{mn} l_{im} l_{jn} \sigma'_{mn} = \sum_{kl} c_{ijkl} \varepsilon_{kl}. \tag{2.11}$$

Therefore from Eq. (2.9), Eq. (2.10) and Eq.(2.11), we get

$$\sum_{lk} \left[\sum_{mn} \sum_{qr} c'_{mnqr} l_{im} l_{jn} l_{kq} l_{lr} - c_{ijkl} \right] \varepsilon_{kl} = 0. \tag{2.12}$$

Since this must be valid for arbitrary values of the ε_{kl} , we obtain the transformation rule for the elastic constants as

$$c_{ijkl} = \sum_{mn} \sum_{qr} c'_{mnqr} l_{im} l_{jn} l_{kq} l_{lr}. \tag{2.13}$$

This confirms that the elastic constants c_{ijkl} are the components of a fourth rank tensor. The 21 independent elastic constants can be simplified by considering the symmetry conditions found in a cubic structure. Rotations of 180° and 90° about the cubic *x, y*, and *z* axes are

cubic symmetry elements, and by applying Eq. (2.13) to these rotations, we obtain $c_{11} = c_{22} = c_{33}$, $c_{12} = c_{21} = c_{23} = c_{32} = c_{13} = c_{31}$ and $c_{44} = c_{55} = c_{66}$. All the other components become zero i.e. $c_{16} = c_{15} = c_{26} = c_{24} = c_{35} = c_{34} = c_{14} = c_{56} = c_{25} = c_{46} = c_{36} = c_{45} = 0$. Thus the cubic structure has three independent elastic constants:

$$c_{ij} = \begin{pmatrix} c_{11} & c_{12} & c_{12} & 0 & 0 & 0 \\ c_{12} & c_{11} & c_{12} & 0 & 0 & 0 \\ c_{12} & c_{12} & c_{11} & 0 & 0 & 0 \\ 0 & 0 & 0 & c_{44} & 0 & 0 \\ 0 & 0 & 0 & 0 & c_{44} & 0 \\ 0 & 0 & 0 & 0 & 0 & c_{44} \end{pmatrix}. \tag{2.14}$$

If the solid is isotropic, the elastic constant tensor looks the same from any Cartesian coordinate symmetry. Therefore, considering for example a 45° rotation about the z axis (which is not a cubic symmetry element), we obtain

$$c_{44} = \frac{c_{11} - c_{12}}{2}, \tag{2.15}$$

so that the number of independent constants is reduced to two. We now define anisotropy ratio, A *as*

$$A = \frac{2c_{44}}{c_{11} - c_{12}}. \tag{2.16}$$

The deviation of A from unity measures the anisotropy of the cubic structure. The two independent elastic constants of an isotropic

medium can be rewritten in different ways. The Lame constant, λ and the shear modulus, μ are defined as

$$\lambda + 2\mu = C_{11} \tag{2.17}$$

and

$$\mu = C_{44} = \frac{c_{11} - c_{12}}{2}. \tag{2.18}$$

Hence the matrix in Eq.(2.14) can be rewritten as

$$\begin{pmatrix} \lambda+2\mu & \lambda & \lambda & 0 & 0 & 0 \\ \lambda & \lambda+2\mu & \lambda & 0 & 0 & 0 \\ \lambda & \lambda & \lambda+2\mu & 0 & 0 & 0 \\ 0 & 0 & 0 & \mu & 0 & 0 \\ 0 & 0 & 0 & 0 & \mu & 0 \\ 0 & 0 & 0 & 0 & 0 & \mu \end{pmatrix}, \tag{2.19}$$

and Eq.(2.7) reduces to

$$\begin{aligned} \sigma_{11} &= (\lambda+2\mu)\varepsilon_{11} + \lambda\varepsilon_{22} + \lambda\varepsilon_{33} \\ \sigma_{22} &= \lambda\varepsilon_{11} + (\lambda+2\mu)\varepsilon_{22} + \lambda\varepsilon_{33} \\ \sigma_{33} &= \lambda\varepsilon_{11} + \lambda\varepsilon_{22} + (\lambda+2\mu)\varepsilon_{33} \\ \sigma_{23} &= 2\mu\varepsilon_{23} \\ \sigma_{13} &= 2\mu\varepsilon_{13} \\ \sigma_{12} &= 2\mu\varepsilon_{12} \end{aligned}. \tag{2.20}$$

In addition, the Young's modulus, E and Poisson's ratio, ν can be written in terms of the Lame constant and the shear modulus as[51]

$$E = \frac{\mu(3\lambda+2\mu)}{\mu+\lambda} \tag{2.21}$$

and

$$\nu = \frac{\lambda}{2(\mu+\lambda)}. \tag{2.22}$$

In terms of the constants E and ν, Eq. (2.20) can be written as

$$\begin{aligned}
\sigma_{11} &= \frac{E}{(1+\nu)(1-2\nu)}\left[\varepsilon_{11}+\nu(\varepsilon_{22}+\varepsilon_{33}-\varepsilon_{11})\right] \\
\sigma_{22} &= \frac{E}{(1+\nu)(1-2\nu)}\left[\varepsilon_{22}+\nu(\varepsilon_{11}+\varepsilon_{33}-\varepsilon_{22})\right] \\
\sigma_{33} &= \frac{E}{(1+\nu)(1-2\nu)}\left[\varepsilon_{33}+\nu(\varepsilon_{11}+\varepsilon_{33}-\varepsilon_{33})\right] \\
\sigma_{23} &= \frac{(1+\nu)}{E}\varepsilon_{23} \\
\sigma_{13} &= \frac{(1+\nu)}{E}\varepsilon_{13} \\
\sigma_{12} &= \frac{(1+\nu)}{E}\varepsilon_{12}
\end{aligned} \tag{2.23}$$

These stress equations (Eq.(2.23)) will be used in the section [2.2] to discuss the stress-strain effect in the core-shell nanowires.

We will also need the equations of equilibrium.[52] The equations of equilibrium in Cartesian coordinates for an element with no external body forces are given by

$$\begin{aligned}
\frac{\partial\sigma_{xx}}{\partial x}+\frac{\partial\sigma_{yx}}{\partial y}+\frac{\partial\sigma_{zx}}{\partial z} &= 0 \\
\frac{\partial\sigma_{xy}}{\partial x}+\frac{\partial\sigma_{yy}}{\partial y}+\frac{\partial\sigma_{zy}}{\partial z} &= 0 \\
\frac{\partial\sigma_{xz}}{\partial x}+\frac{\partial\sigma_{yz}}{\partial y}+\frac{\partial\sigma_{zz}}{\partial z} &= 0
\end{aligned} \tag{2.24}$$

Consequently, the equations of equilibrium[52] in cylindrical coordinates are given by

$$\begin{aligned}
&\frac{\partial \sigma_{rr}}{\partial r}+\frac{\sigma_{rr}-\sigma_{\theta\theta}}{r}+\frac{1}{r}\frac{\partial \sigma_{r\theta}}{\partial \theta}+\frac{\partial \sigma_{zr}}{\partial z}=0 \\
&\frac{\partial \sigma_{r\theta}}{\partial r}+\frac{2\sigma_{r\theta}}{r}+\frac{1}{r}\frac{\partial \sigma_{\theta\theta}}{\partial \theta}+\frac{\partial \sigma_{z\theta}}{\partial z}=0 \\
&\frac{\partial \sigma_{rz}}{\partial r}+\frac{\sigma_{rz}}{r}+\frac{1}{r}\frac{\partial \sigma_{\theta z}}{\partial \theta}+\frac{\partial \sigma_{zz}}{\partial z}=0
\end{aligned} \quad . \tag{2.25}$$

2.3 The Ge-Si core-shell nanowire

For the study of strain effects in in core-shell nanowires we consider a cylindrical geometry, in which c is the radius of the core region and a the outer radius of the shell. For concreteness and because this is our experimental case, we will assume that the core material is Ge and the shell material is Si, but the results derived here are also valid for the reverse situation. The nanowire to be consider is schematically illustrated in Fig. 2.1 below

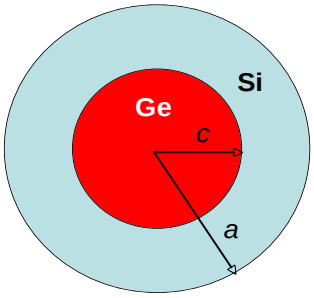

Fig(2.1):The cylindrical geometry of the core-shell nanowire. The internal radius is given by c and the external radius by a.

We start with the assumption that the elastic constants of Si and Ge are same. As mentioned above, this is not a very good approximation, but it is done to reproduce the result in Liang *et al.*[40] We choose the z axis along the nanowire axis and the origin at the center of the core. Because of the cylindrical symmetry of the nanowire and the fact that the atomic planes are aligned, we can write

$$\begin{aligned} u_r(r,\theta,z) &\equiv u_r(r) \\ u_\theta(r,\theta,z) &\equiv 0 \\ u_z(r,\theta,z) &\equiv u_z(z) \end{aligned} \quad , \tag{2.26}$$

where u_r, u_θ and u_z are the displacements in r, θ and z direction. This implies that the normal and shear strains can be written as

$$\begin{aligned} &\varepsilon_{rr} = \frac{\partial u_r}{\partial r}; \quad \varepsilon_{\theta\theta} = \frac{u_r}{r}; \quad \varepsilon_{zz} = \frac{\partial u_z}{\partial z}; \\ &\varepsilon_{r\theta} = 0; \quad \varepsilon_{zr} = 0; \quad \varepsilon_{\theta z} = 0. \end{aligned} \tag{2.27}$$

For an isotropic material the stress and strain equations in Eq.(2.23) are valid for any coordinate system. Hence the stress and

strain in cylindrical coordinates are related by following equations[53] :

$$\begin{aligned}
\sigma_{rr} &= \frac{E}{(1+\nu)(1-2\nu)}\left[(1-\nu)\varepsilon_{rr} + \nu(\varepsilon_{\theta\theta} + \varepsilon_{zz})\right] \\
\sigma_{\theta\theta} &= \frac{E}{(1+\nu)(1-2\nu)}\left[(1-\nu)\varepsilon_{\theta\theta} + \nu(\varepsilon_{rr} + \varepsilon_{zz})\right] \\
\sigma_{zz} &= \frac{E}{(1+\nu)(1-2\nu)}\left[(1-\nu)\varepsilon_{zz} + \nu(\varepsilon_{rr} + \varepsilon_{\theta\theta})\right] \\
\sigma_{\theta z} &= \frac{(1+\nu)}{E}\varepsilon_{\theta z} \\
\sigma_{rz} &= \frac{(1+\nu)}{E}\varepsilon_{rz} \\
\sigma_{r\theta} &= \frac{(1+\nu)}{E}\varepsilon_{r\theta}.
\end{aligned} \tag{2.28}$$

Using Eq.(2.27) in Eq. (2.28), we can write, $\sigma_{rz} = \sigma_{r\theta} = \sigma_{z\theta} = 0$

Therefore the equilibrium equations in Eq.(2.25) can be written as

$$\begin{aligned}
&\frac{\partial \sigma_{rr}}{\partial r} + \frac{\sigma_{rr} - \sigma_{\theta\theta}}{r} = 0 \\
&\frac{1}{r}\frac{\partial \sigma_{\theta\theta}}{\partial \theta} = 0 \\
&\frac{\partial \sigma_{zz}}{\partial z} = 0.
\end{aligned} \tag{2.29}$$

Now substituting Eq.(2.28) and Eq.(2.27) into Eq.(2.29), the differential equation satisfied by the displacements is

$$\frac{d^2 u_r}{dr^2} + \frac{1}{r}\frac{du_r}{dr} - \frac{u_r}{r^2} = 0\,. \tag{2.30}$$

To solve Eq.(2.30) we let $g(r) = r\,u(r)$, hence Eq.(2.30) can be written as

$$\frac{d}{dr}\left(\frac{1}{r}g'(r)\right) = 0\,. \tag{2.31}$$

Thus $g'(r)/r = 0$ is a constant and then

$$u_r = C_1 r + \frac{C_2}{r} \rightarrow \varepsilon_{rr} = C_1 - \frac{C_2}{r^2}. \tag{2.32}$$

Similarly, $\varepsilon_{\theta\theta} = \frac{u_r}{r} = C_1 + \frac{C_2}{r^2}$

$$\varepsilon_{\theta\theta} = \frac{u_r}{r} = C_1 + \frac{C_2}{r^2}. \tag{2.33}$$

Combining Eq.(2.32) and Eq.(2.33) we have $\varepsilon_{rr} + \varepsilon_{\theta\theta} = 2C_1 = constant$. Hence using this in Eq. (2.26) for σ_{zz}, we obtain

$$u_z = \varepsilon_{zz} z \ , \tag{2.34}$$

with ε_{zz} as constant.

There are six integration constants to be determined are $C_1^i, C_2^i, \varepsilon_{zz}^i$ and $C_1^o, C_2^o, \varepsilon_{zz}^o$, where superscripts *i* and *o* refers to inner (Ge) and outer (Si) cylinder respectively. The constant C_2^o must be zero, because the strain cannot diverge for $r = 0$. Hence we are reduced to 5 constants, and the required five boundary conditions[40] are

$$\begin{aligned}
&\sigma_{rr}^i(c) = \sigma_{rr}^o(c) \\
&\sigma_{rr}^o(a) = 0 \\
&\sigma_{zz}^o\left(a^2 - c^2\right) + \sigma_{zz}^i c^2 = 0, \\
&u_r^i(c) - u_r^o(c) = c\varepsilon_{misfit} \\
&u_z^i(l) - u_z^o(l) = l\varepsilon_{misfit}
\end{aligned} \tag{2.35}$$

where $\varepsilon_{misfit} = (a_{Si} - a_{Ge})/a_{Ge}$, in which a_{Ge} and a_{Si} are the lattice constant of Ge and Si respectively and l is the half-length of the

cylinder. In Eq.(2.35) the first condition makes the pressure continuous across the interface. The second condition stipulates that the external pressure is zero. The third condition insures that the net force in the z direction is zero at any plane perpendicular to the z axis. The fourth condition is identical to those in "shrink-fit" problems discussed in elasticity textbooks, and forces the displacement to accommodate the length mismatch between the two materials. The same is valid for the last condition. Since the first three conditions are expressed in terms of the stresses and not on the displacements, we need to find the corresponding expression for the stresses. Hence substituting Eq.(2.32) and Eq.(2.33) into Eq.(2.28) we have,

$$\begin{aligned}\sigma_{rr}^{i} &= \frac{E}{(1+\nu)(1-2\nu)}\left[(1-\nu)\varepsilon_{rr}^{i}+\nu(\varepsilon_{\theta\theta}^{i}+\varepsilon_{zz}^{i})\right] \\ &= \frac{E}{(1+\nu)(1-2\nu)}\left[(1-\nu)C_{1}^{i}+\nu(C_{1}^{i}+\varepsilon_{zz}^{i})\right]. \\ &= \frac{E}{(1+\nu)(1-2\nu)}\left[C_{1}^{i}+\nu\varepsilon_{zz}^{i}\right] \\ &= -P\end{aligned} \tag{2.36}$$

We notice that σ_{rr} is constant, so that it must be equal to its value at the boundary $r=c$, which is denoted as $-P$, where P is the misfit strain-induced pressure. Similarly, for $\sigma_{\theta\theta}^{i}$ we get,

$$\begin{aligned}\sigma_{\theta\theta}^{i} &= \frac{E}{(1+\nu)(1-2\nu)}\left[(1-\nu)\varepsilon_{\theta\theta}^{i}+\nu(\varepsilon_{rr}^{i}+\varepsilon_{zz}^{i})\right] \\ &= -P.\end{aligned} \tag{2.37}$$

Therefore inside the cylinder $\sigma_{\theta\theta}$ is also constant. Finally we have,

$$\begin{aligned}\sigma_{zz}^{i} &= \frac{E}{(1+\nu)(1-2\nu)}\left[(1-\nu)\varepsilon_{zz}^{i} + \nu(\varepsilon_{rr}^{i} + \varepsilon_{\theta\theta}^{i})\right] \\ &= \frac{E}{(1+\nu)(1-2\nu)}\left[(1-\nu)\varepsilon_{zz}^{i} + 2\nu C_1^{i}\right].\end{aligned} \tag{2.38}$$

Now using the first two boundary conditions, the stress for the outer shell becomes

$$\begin{aligned}\sigma_{rr}^{o}(a) &= \frac{E}{(1+\nu)(1-2\nu)}\left[(1-\nu)\varepsilon_{rr}^{o} + \nu(\varepsilon_{\theta\theta}^{o} + \varepsilon_{zz}^{o})\right] \\ &= \frac{E}{(1+\nu)(1-2\nu)}\left[C_1^0 - (1-2\nu)\frac{C_2^0}{a^2} + \nu\varepsilon_{zz}^{o}\right] \\ &= 0,\end{aligned} \tag{2.39}$$

$$\begin{aligned}\sigma_{rr}^{o}(c) &= \frac{E}{(1+\nu)(1-2\nu)}\left[(1-\nu)\varepsilon_{rr}^{o} + \nu\left(\varepsilon_{\theta\theta}^{o} + \varepsilon_{zz}^{o}\right)\right] \\ &= \frac{E}{(1+\nu)(1-2\nu)}\left[C_1^0 - (1-2\nu)\frac{C_2^0}{c^2} + \nu\varepsilon_{zz}^{o}\right] \\ &= -P,\end{aligned} \tag{2.40}$$

and

$$\begin{aligned}\sigma_{zz}^{o} &= \frac{E}{(1+\nu)(1-2\nu)}\left[(1-\nu)\varepsilon_{zz}^{o} + \nu(\varepsilon_{rr}^{o} + \varepsilon_{\theta\theta}^{o})\right] \\ &= \frac{E}{(1+\nu)(1-2\nu)}\left[(1-\nu)\varepsilon_{zz}^{o} + 2\nu C_1^{0}\right].\end{aligned} \tag{2.41}$$

Combining Eq. (2.39) and Eq. (2.40) we obtain,

$$C_2^0 = \frac{Pa^2}{E}\frac{(1+\nu)}{a^2/c^2 - 1}$$

and (2.42)

$$C_1^0 + \nu\varepsilon_{zz}^{o} = \frac{P}{E}\frac{(1+\nu)(1-2\nu)}{a^2/c^2 - 1}.$$

Rearranging Eq.(2.36) we have

$$C_1^i + \nu\varepsilon_{zz}^i = -P\frac{(1+\nu)(1-2\nu)}{E} \tag{2.43}$$

Using Eq.(2.34) and the fourth condition in Eq.(2.35) , we get

$$\varepsilon_{zz}^i - \varepsilon_{zz}^o = \varepsilon_{misfit}. \tag{2.44}$$

Also with simple algebra, when applied to the third condition of Eq. (2.35) to Eq.(2.38) and Eq. (2.41) we get

$$(1-\nu)\left[\varepsilon_{zz}^o\left(a^2-c^2\right)+\varepsilon_{zz}^i c^2\right]+2\nu\left[C_1^0\left(a^2-c^2\right)+C_1^i c^2\right]=0. \tag{2.45}$$

From Eq. (2.42) and Eq. (2.43) we find

$$C_1^0\left(a^2-c^2\right)+C_1^i c^2 = -\nu\left(a^2-c^2\right)\varepsilon_{zz}^o - \nu c^2\varepsilon_{zz}^i. \tag{2.46}$$

On substituting Eq.(2.46) into Eq.(2.45) we obtain

$$\varepsilon_{zz}^o\left(a^2-c^2\right)+\varepsilon_{zz}^i c^2 = 0. \tag{2.47}$$

Combining with Eq.(2.44) we get,

$$\varepsilon_{zz}^o = -\frac{c^2}{a^2}\varepsilon_{misfit}$$

and (2.48)

$$\varepsilon_{zz}^i = \left(1-\frac{c^2}{a^2}\right)\varepsilon_{misfit} \quad .$$

Hence the constants C_2^0 , C_1^0 and C_1^i in Eq.(2.42) and Eq.(2.43) can be written as

$$C_2^0 = \frac{Pa^2}{E}\frac{(1+\nu)}{a^2/c^2-1},$$

$$C_1^0 = \frac{P}{E}\frac{(1+\nu)(1-2\nu)}{a^2/c^2-1} + \frac{\nu c^2}{a^2}\varepsilon_{misfit}$$

and (2.49)

$$C_1^i = -P\frac{(1+\nu)(1-2\nu)}{E} - \nu\left(1-\frac{c^2}{a^2}\right)\varepsilon_{misfit}.$$

In the final step we have to find P in terms of ε_{misfit}. For this we use the fourth condition of Eq.(2.35). Substituting Eq.(2.47) and Eq.(2.48) into Eq.(2.32), we get

$$u_r^i(c) = C_1^i c = \left[-\frac{P}{E}(1+\nu)(1-2\nu) - \nu\left(1-\frac{c^2}{a^2}\right)\varepsilon_{misfit}\right]c$$

and (2.50)

$$u_r^o(c) = C_1^o c + \frac{C_2^o}{c} = \left[\frac{P}{E}\frac{(1+\nu)(1-2\nu)}{a^2/c^2-1} + \frac{\nu c^2}{a^2}\varepsilon_{misfit}\right]c + \left[\frac{Pa^2}{E}\frac{(1+\nu)}{a^2/c^2-1}\right]\frac{1}{c}.$$

Therefore, using the fourth condition of Eq.(2.35) $u_r^i(c) - u_r^o(c) = c\varepsilon_{misfit}$. We obtain P as,

$$P = -\frac{E\varepsilon_{misfit}\left(1-\frac{c^2}{a^2}\right)}{2(1-\nu)}. \quad (2.51)$$

Substituting P from Eq. (2.51)into Eq. (2.49) we obtain the C_2^0 , C_1^0

and C_1^i coefficients and hence the corresponding values of the strain for the core and shell as

$$\varepsilon_{rr}^{i} = C_1^i = \varepsilon_{misfit}\left(1-\frac{c^2}{a^2}\right)\frac{1-3\nu}{2(1-\nu)}, \tag{2.52}$$

$$\varepsilon_{\theta\theta}^{i} = C_1^i = \varepsilon_{misfit}\left(1-\frac{c^2}{a^2}\right)\frac{1-3\nu}{2(1-\nu)}, \tag{2.53}$$

$$\varepsilon_{zz}^{i} = \left(1-\frac{c^2}{a^2}\right)\varepsilon_{misfit} \tag{2.54}$$

and

$$\varepsilon_{rr}^{o} = C_1^o - \frac{C_2^o}{r^2} = \frac{\varepsilon_{misfit}}{2(1-\nu)}\left(\frac{c^2}{a^2}\right)\left[(3\nu-1)+(1+\nu)\frac{a^2}{r^2}\right], \tag{2.55}$$

$$\varepsilon_{\theta\theta}^{o} = C_1^o + \frac{C_1^o}{r^2} = \frac{\varepsilon_{misfit}}{2(1-\nu)}\left(\frac{c^2}{a^2}\right)\left[(3\nu-1)-(1+\nu)\frac{a^2}{r^2}\right], \tag{2.56}$$

$$\varepsilon_{zz}^{o} = -\frac{c^2}{a^2}\varepsilon_{misfit}\,. \tag{2.57}$$

Comparing with equations (8) and (9) in Liang's paper, we notice that we agree on everything except the expressions in Eq.(2.56) and Eq.(2.55). The two equations in Liang's[40] paper are incorrect, probably due to a typo, as can be seen from the fact that they do not satisfy the radial and axial lattice mismatch conditions in Eq.(2.35).

2.4 A Realistic Solution to Ge-core and Si-shell Nanowire

To obtain a more realistic solution, we eliminate the restriction that the Young modulus be the same for the two materials, but keep Poisson's ratio the same. This is a good approximation for Si and Ge. Since *ratios* of elastic constants are nearly the same for these materials, their corresponding Poisson ratios are very similar for any crystallographic orientation. We also allow for the possibility, discussed in the literature, that some extra atomic planes in the Si shell might relax the strain. We thus need to redefine the boundary conditions.

Let us consider a Ge core and a Si shell, initially unstrained. The length of the Ge core is Na_{Ge}, where a_{Ge} is the Ge lattice constant and N the number of atomic planes. When the nanowire is formed, the N lattice planes in Ge will have to compress and the N lattice planes in Si will have to expand until they acquire the same length. To allow for strain relaxation, however, let us assume that there are some δN extra atomic planes in the Si shell. Then the boundary condition at the end of the nanowire is given as

$$Na_{Ge} + u_z\left(l_{Ge}\right) = \left(N + \delta N\right)a_{Si} + u_z\left(l_{Si}\right), \tag{2.58}$$

where $l_{Ge} = Na_{Ge}$ and $l_{Si} = \left(N + \delta N\right)a_{Si}$ are the unstrained positions of the end of the core and shell, respectively. Now if the lattice mismatch

is entirely accommodated by adding extra atomic planes, then the $u's$ are zero, and we get

$$\frac{\delta N_{max}}{N} = \frac{a_{Ge} - a_{Si}}{a_{Si}} \equiv -\varepsilon_{misfit}\,, \tag{2.59}$$

where we have defined an ε_{misfit} that is slightly different from the one used earlier, as now we have a_{Si} in the denominator. The value in Eq.(2.59) is the maximum possible value of δN, we can then define a relaxation parameter ρ such that

$$\frac{\delta N}{N} = -\rho\varepsilon_{misfit} \qquad 0 \le \rho \le 1\,. \tag{2.60}$$

Thus $\rho = 0$ corresponds to no relaxation and $\rho = 1$corresponds to full relaxation. Eq. (2.58) can be rewritten as

$$N a_{Ge} + l_{Ge}\varepsilon_{zz}^{i} = \left(N + \delta N\right) a_{Si} + l_{Si}\varepsilon_{zz}^{o}\,. \tag{2.61}$$

Eq. (2.61) can be rearranged and rewritten as

$$\frac{a_{Ge}}{a_{Si}}\varepsilon_{zz}^{i} - \left(1 + \frac{\delta N}{N}\right)\varepsilon_{zz}^{o} = \left(1 + \frac{\delta N}{N}\right) - \frac{a_{Ge}}{a_{Si}}\,. \tag{2.62}$$

But from Eq. (2.59) a_{Ge} / $a_{Si} = 1 - \varepsilon_{misfit}$. Hence from Eq.(2.62), we get

$$\left(1 - \varepsilon_{misfit}\right)\varepsilon_{zz}^{i} - \left(1 - \rho\varepsilon_{misfit}\right)\varepsilon_{zz}^{o} = \varepsilon_{misfit}(1 - \rho) \tag{2.63}$$

For $\rho = 1$this gives $\varepsilon_{zz}^{i} = \varepsilon_{zz}^{o}$, as expected. For $\rho = 0$we obtain the expression

$$\left(1 - \varepsilon_{misfit}\right)\varepsilon_{zz}^{i} - \varepsilon_{zz}^{o} = \varepsilon_{misfit}\,. \tag{2.64}$$

This is almost the same as Eq.(2.44) but not identical. The difference is very small and probably negligible given the approximations involved with the continuum model. So if we consider $1-e_{\text{misfit}} \approx 1-\rho e_{\text{misfit}} \approx 1$, we finally have

$$\varepsilon_{zz}^{i} - \varepsilon_{zz}^{o} = \varepsilon_{misfit}(1-\rho). \tag{2.65}$$

Within this approximation, we note that ε_{misfit} can be written as either $\varepsilon_{misfit} = \left(a_{Si} - a_{Ge}\right)/a_{Ge}$ or $\varepsilon_{misfit} = \left(a_{Si} - a_{Ge}\right)/a_{Si}$. With these new boundary conditions we recalculate the strain distribution for the core-shell nanowires.

2.5 New Strain components in Core-Shell nanowire

The strain expressions in section [2.1] are recomputed using the more realistic assumptions discussed in section [2.2] .We thus obtain

$$C_2^o = \frac{Pa^2}{E^0}\frac{(1+\nu)}{a^2/c^2 - 1} \tag{2.66}$$

$$C_1^o + \nu\varepsilon_{zz}^o = \frac{P}{E^0}\frac{(1+\nu)(1-2\nu)}{a^2/c^2 - 1}, \tag{2.67}$$

and

$$C_1^i + \nu\varepsilon_{zz}^i = -P\frac{(1+\nu)(1-2\nu)}{E^i}, \tag{2.68}$$

where E^0 and E^i are the young's modulus of shell Si and core Ge respectively. Combining these two equations and rearranging we get

$$C_1^o E^0\left(a^2/c^2-1\right)+C_1^i E^i=-\nu\varepsilon_{zz}^o E^0\left(a^2/c^2-1\right)-\nu\varepsilon_{zz}^i E^i. \qquad (2.69)$$

The equivalent of Eq.(2.45), gives the expression

$$(1+\nu)\left[\varepsilon_{zz}^o E^0\left(a^2-c^2\right)+\varepsilon_{zz}^i E^i c^2\right]+2\nu\left[C_1^o E^0\left(a^2-c^2\right)+C_1^i E^i c^2\right]=0. \qquad (2.70)$$

Now combining and solving Eq.(2.69) and Eq. (2.70) , we get

$$\varepsilon_{zz}^o E^0\left(a^2-c^2\right)+\varepsilon_{zz}^i E^i c^2=0. \qquad (2.71)$$

Combining the above Eq.(2.70) with Eq.(2.65)

$$\varepsilon_{zz}^o=-\frac{E^i c^2(1-\rho)\varepsilon_{misfit}}{E^0\left(a^2-c^2\right)+E^i c^2}$$

and (2.72)

$$\varepsilon_{zz}^i==(1-\rho)\varepsilon_{misfit}\left[\frac{E^0\left(a^2-c^2\right)}{E^0\left(a^2-c^2\right)+E^i c^2}\right].$$

Hence the coefficients in Eq. (2.66) , Eq.(2.67) and Eq.(2.68) can be written as

$$C_2^o=\frac{Pa^2}{E^0}\frac{(1+\nu)}{a^2/c^2-1}$$

$$C_1^o=\frac{P}{E^0}\frac{(1+\nu)(1-2\nu)}{a^2/c^2-1}+\nu\frac{E^i c^2(1-\rho)\varepsilon_{misfit}}{E^0\left(a^2-c^2\right)+E^i c^2},$$

and (2.73)

$$C_1^i=-P\frac{(1+\nu)(1-2\nu)}{E^i}-\nu(1-\rho)\varepsilon_{misfit}\left[\frac{E^0\left(a^2-c^2\right)}{E^0\left(a^2-c^2\right)+E^i c^2}\right]$$

The final step is to express misfit stain-induced pressure P in terms of ε_{misfit}. Hence we again use the fourth equation in Eq.(2.35). Substituting Eq. (2.73) into Eq.(2.70) we have

$$u_r^i(c) = C_1^i c$$
$$= \left[-P\frac{(1+\nu)(1-2\nu)}{E^i} - \nu(1-\rho)\varepsilon_{misfit}\left[\frac{E^0\left(a^2-c^2\right)}{E^0\left(a^2-c^2\right)+E^i c^2}\right]\right]c$$

and (2.74)

$$u_r^o(c) = C_1^o c + \frac{C_1^o}{c}$$
$$= \left[\frac{P}{E^0}\frac{(1+\nu)(1-2\nu)}{a^2/c^2-1} + \nu\frac{E^i c^2(1-\rho)\varepsilon_{misfit}}{E^0\left(a^2-c^2\right)+E^i c^2}\right]c + \left[\frac{Pa^2}{E^0}\frac{(1+\nu)}{a^2/c^2-1}\right]\frac{1}{c}.$$

Therefore using Eq.(2.35) and rearranging the term, we get the following expression

$$P\left\{\left[-\frac{(1-2\nu)}{E^i}\right] - \frac{1}{E^0}\left[\frac{(1-2\nu)c^2+a^2}{a^2-c^2}\right]\right\} = \left[\frac{(1-\rho)\nu+1}{1+\nu}\right]\varepsilon_{misfit}.$$

(2.75)

Let us now define the quantity, γ

$$\gamma = \frac{E^i}{E^0}. \tag{2.76}$$

On substituting Eq.(2.76) in Eq.(2.75), the solution for P becomes

$$P = \frac{\varepsilon_{misfit}E^i\left(a^2-c^2\right)\left\{\left[(1-\rho)\nu+1\right]/\left[1+\nu\right]\right\}}{(1-\gamma)(1-2\nu)c^2-(1-2\nu+\gamma)a^2}. \tag{2.77}$$

The new coefficients C_1^o, C_2^o and C_1^i can finally be obtained by using Eq.(2.77) in Eq.(2.75) and hence the final strain components are written by using the coefficients C_1^o, C_2^o and C_1^i in Eq.(2.32) and Eq.(2.33).

The final strain expressions for the core are:

$$\varepsilon_{rr}^i = C_1^i = -\varepsilon_{misfit}\left(a^2 - c^2\right)\left\{\frac{\left[\left(1-\rho\right)\nu + 1\right]\left(1-2\nu\right)}{\left(1-\gamma\right)\left(1-2\nu\right)c^2 - \left(1-2\nu+\gamma\right)a^2} + \frac{\nu\left(1-\rho\right)}{\left(a^2-c^2\right)+\gamma c^2}\right\},$$

$$\varepsilon_{\theta\theta}^i = C_1^i = -\varepsilon_{misfit}\left(a^2 - c^2\right)\left\{\frac{\left[\left(1-\rho\right)\nu + 1\right]\left(1-2\nu\right)}{\left(1-\gamma\right)\left(1-2\nu\right)c^2 - \left(1-2\nu+\gamma\right)a^2} + \frac{\nu\left(1-\rho\right)}{\left(a^2-c^2\right)+\gamma c^2}\right\},$$

$$\varepsilon_{zz}^i = \varepsilon_{misfit}\left(1-\rho\right)\left[\frac{\left(a^2-c^2\right)}{\left(a^2-c^2\right)+\gamma c^2}\right]. \qquad (2.78)$$

The final expressions for the shell strain are:

$$\varepsilon_{rr}^o = \frac{\varepsilon_{misfit}\left[\left(1-\rho\right)\nu+1\right]c^2}{\left(1-\gamma\right)\left(1-2\nu\right)c^2 - \left(1-2\nu+\gamma\right)a^2}\left[\left(1-2\nu\right) - \frac{a^2}{r^2}\right] + \frac{\nu\gamma c^2\left(1-\rho\right)\varepsilon_{misfit}}{\left(a^2-c^2\right)+\gamma c^2},$$

$$\varepsilon_{\theta\theta}^o = \frac{\varepsilon_{misfit}\left[\left(1-\rho\right)\nu+1\right]c^2}{\left(1-\gamma\right)\left(1-2\nu\right)c^2 - \left(1-2\nu+\gamma\right)a^2}\left[\left(1-2\nu\right) + \frac{a^2}{r^2}\right] + \frac{\nu\gamma c^2\left(1-\rho\right)\varepsilon_{misfit}}{\left(a^2-c^2\right)+\gamma c^2},$$

$$\varepsilon_{zz}^i = \frac{\varepsilon_{misfit}\gamma c^2\left(1-\rho\right)}{\left(a^2-c^2\right)+\gamma c^2}. \qquad (2.79)$$

As expected, in the limit $\gamma = 1$ and $\rho = 0$ we obtain the strain components calculated earlier assuming the same Young's modulus and no relaxation of core and shell. The expression in Eq. (2.78) and Eq.(2.79) will be used later to discuss the Raman spectra of core and shell.

CHAPTER 3

VIBRATIONAL AND RAMAN THEORY OF SEMICONDUCTORS

3.1 Introduction

In solids, the small oscillations[56,62] of atoms about the crystalline equilibrium positions can be described as a collection of independent normal modes. Applying the usual quantization conditions to these normal modes gives rise to "phonons". Lattice vibrations modulate the dielectric response of the crystal, giving rise to inelastic scattering of light, commonly known as Raman scattering. The kinematic selection rules for Raman scattering limit this process to phonons of vanishing wavevector, and since acoustic phonons have vanishing frequencies in this limit, Raman scattering is practically limited to optic vibrations with finite frequencies in the long-wavelength limit. Here we present a brief review of lattice vibrations followed by a discussion of first-order Raman scattering from a classical, semi-classical and quantum perspective. Later sections describe the Raman selection rules, optical phonons under strain and experimental set-up.

3.2 A review of lattice vibrations

The optical phonons that are detected with Raman spectroscopy appear in lattices with a base. In particular, the diamond lattice has a face-centered cubic structure[54] with two identical atoms at its two–

point basis, located at 0 and $(a/4)(\hat{x}+\hat{y}+\hat{z})$, where a is the lattice constant of the cubic unit cell. If the perfect lattice cell is described by vectors a_1, a_2, a_3, in *x, y* and *z* directions respectively then the equilibrium position vector of an atom in the basis of the primitive cell is given by

$$\bar{R}(l) = l_1\bar{a}_1 + l_2\bar{a}_2 + l_3\bar{a}_3, \tag{3.1}$$

where l_1, l_2, l_3 are integers.

Let us assume that there are N unit cells which have n atoms per unit cell with masses $m_k (k = 1,2,\ldots\ldots n)$. Also if $\bar{R}(k)$ is the position vector of the k^{th} atom in the basis of l^{th} primitive cell then the position of atom in equilibrium is defined as

$$\bar{R}(l,k) = \bar{R}(l) + \bar{R}(k), \tag{3.2}$$

where $\bar{R}(l)$ is defined in Eq.(3.1). The Cartesian components of $\bar{R}(l,k)$ are identified as $x_\alpha(l,k)(\alpha = 1,2,3)$.Now we consider the displacement[55,56] of the k^{th} atom in the l^{th} cell from its equilibrium, $x_\alpha^0(l,k)$ by $u(lk)$. The kinetic energy of the lattice is given by

$$T = \frac{1}{2}\sum_{nk\alpha} m_k \dot{u}^2(nk\alpha) \tag{3.3}$$

Within the adiabatic approximation, the total potential energy *V* of the lattice is electronic ground-state energy at a frozen position away from equilibrium. The first derivatives vanish,

$\left(\partial V / \partial x_\alpha(l,k)\right)_0 = 0$, at equilibrium, since the forces acting are zero. The second order term of the potential, which is the only contribution included within the harmonic approximation, is given by

$$V = \frac{1}{2}\sum_{nk}\sum_{n'k'}\sum_{\alpha\beta}\varphi_{\alpha\beta}\left(lk;l'k'\right)u\left(lk\right)u(lk'), \tag{3.4}$$

where $\varphi_{\alpha\beta}\left(lk;lk'\right) = \left[\frac{\partial^2 V}{\partial x_\alpha(lk)\partial x_\beta(l'k')}\right]_0$. (3.5)

The Hamiltonian, H for the crystal lattice can be written as

$$H = \frac{1}{2}\sum_{nk\alpha} m_k \dot{u}^2(nk\alpha) + \frac{1}{2}\sum_{nk}\sum_{n'k'}\sum_{\alpha\beta}\varphi_{\alpha\beta}\left(lk;l'k'\right)u\left(lk\right)u(lk'). \tag{3.6}$$

We can write the equation of motion of the k^{th} atom with mass, m_k as

$$m_k \ddot{u}_\alpha\left(lk\right) + \sum_{n'k'\beta}\varphi_{\alpha\beta}(lk;l'k')u_\beta\left(l'k'\right) = 0. \tag{3.7}$$

Since φ has the periodicity of the lattice, a plane wave solution suitable for Eq.(3.7) is given by

$$u\left(lk\right) = U(0,k)e^{i\left(\bar{q}.\bar{R}(lk)-i\omega t\right)}, \tag{3.8}$$

where $\bar{R}(lk)$ denotes the position vector of the k^{th} atom in the l^{th} primitive cell, q is the wave vector of the reciprocal lattice, and ω is the frequency of the normal mode. Applying the plane wave solution to Eq.(3.7), we get

$$m_k\omega^2 u\left(k\alpha\right) = \sum_{n'k\beta}\varphi_{\alpha\beta}(lk;l'k')u_\beta(l'k')e^{-i\bar{q}.\left[\bar{R}(lk)-\bar{R}(l'k')\right]}. \tag{3.9}$$

Normal coordinates are now introduced to simplify the above equation of motion. The normal coordinate's transformation provides a simplified form of Raman scattering theory by reducing the lattice vibrational problem to a set of independent harmonic oscillators. In the harmonic approximation, the Hamiltonian defined in Eq.(3.6) provides the solution to the vibrational problem. Thus the vibrational Hamiltonian can be written as

$$H = \frac{1}{2}\dot{\tilde{\boldsymbol{u}}}\,\boldsymbol{M}\,\dot{\boldsymbol{u}} + \frac{1}{2}\tilde{\boldsymbol{u}}\,\boldsymbol{\varphi}\,\boldsymbol{u}, \tag{3.10}$$

where $\boldsymbol{u} = u(lk)$ is a $3N \times 1$ vector for the atomic displacements from the equilibrium positions; $\boldsymbol{\varphi} = \varphi_{\alpha\beta}\left(lk; l'k'\right)$ is the $3N \times 3N$ force constant matrix, and $\boldsymbol{M} = \left(m_k \delta_{ll'} \delta_{kk'} \delta_{\alpha\beta}\right)$ is $3N \times 3N$ mass matrix. Henceforth we now define a $3N \times 3N$ matrix eigenvalue equation for harmonically interacting system consisting of N atoms as

$$\left(\boldsymbol{\varphi} - \omega_f^2 \boldsymbol{M}\right)\chi\left(f\right) = 0, \tag{3.11}$$

where ω_f is the normal mode frequency , $\chi\left(f\right) = \chi\left(lk\alpha \mid f\right)$ is the eigenvector related to the lattice motion and $f = 1,2,\ldots\ldots 3N$ labels the normal modes. As the Hamiltonian H is Hermitian, the eigenvectors satisfy the orthonormality, $\sum_{f=1}^{3N} \chi\left(f\right)\chi^{+}\left(f\right)\boldsymbol{M} = I$ and

completeness, $\chi^{+}(f)M\chi(f') = \delta_{ff'}$ relations. We now introduce the normal coordinate, d_f by

$$d_f = \chi^{+}(f)\boldsymbol{M}\boldsymbol{u} = \sum_{nk\alpha}\chi(lk\alpha \mid f)m_k u(lk\alpha). \qquad (3.12)$$

The completeness relation gives the atomic displacements, u in terms of the normal coordinates as

$$\boldsymbol{u} = \sum_f \chi(f) d_f. \qquad (3.13)$$

Hence the potential and kinetic energy in terms of normal coordinates is given by

$$V = \frac{1}{2}\sum_f \omega_f^2 d_f^2 \qquad (3.14)$$

and

$$T = \frac{1}{2}\sum_f \dot{d}_f^2 \qquad (3.15)$$

We thus have the Hamiltonian of $3N$ independent harmonic oscillators as

$$H = \frac{1}{2}\sum_f \left(\dot{d}_f^2 + \omega_f^2 d_f^2\right). \qquad (3.16)$$

Hence the equation of motion in normal co-ordinates is given by

$$\ddot{d}_f + \omega_f^2 d_f = 0. \qquad (3.17)$$

The vibrational problem is solved using quantum mechanics. We

define d_f and $\dot{d}_f$ as operators obeying the commutation relations given as

$$\left[d_f, \dot{d}_f \right] = i\hbar\delta_{ff'}. \tag{3.18}$$

For further treatment of quantum mechanics, creation, a_f and annihilation a_f^+ operators are given as $a_f = \sqrt{1/2\hbar\omega_f}\left(\dot{d}_f - i\omega_f d_f\right)$ and $a_f^+ = \sqrt{1/2\hbar\omega_f}\left(\dot{d}_f + i\omega_f d_f\right)$ respectively. The operators also satisfy the commutation relation given as $a_f a_f^+ = 1/2\hbar\omega\left[\dot{d}_f^2 + \omega_f^2 d_f - \hbar\omega_f\right]$.From the above definition of operators, the normal coordinates is written as

$$d_f = i\sqrt{\frac{\hbar}{2m}}\left(a_f - a_f^+\right). \tag{3.19}$$

We can write the Hamiltonian in Eq.(3.16)

$$H = \sum_f \hbar\omega_f \left(a_f a_f^+ + \frac{1}{2} \right). \tag{3.20}$$

The energy eigenvalues are given by

$$E_{(n_f)} = \sum_f \hbar\omega \left(n_f + \frac{1}{2} \right), \tag{3.21}$$

where $n_f = 0,1,2,.....$ is the number of phonons in mode f .

The normal mode solution for the lattice vibrations can be obtained by inserting the Bloch's waves, $\chi\left(lk\alpha \mid \bar{q}j\right) = \left(e(k\alpha \mid \bar{q}j)/\sqrt{Nm_k}\right)e^{i\bar{q}.\bar{R}(lk)}$ to Eq.(3.11) .

We can write the Eq.(3.11) as

$$\sum_{l'k'\beta} \frac{\varphi_{\alpha\beta}(lk;l'k')}{\sqrt{m_k m_{k'}}} e^{-i\bar{q}.\left[\bar{R}(lk)-\bar{R}(l'k')\right]} \bar{e}(k'\beta \mid \bar{q}j) = \omega^2(\bar{q}j) e(k\alpha \mid \bar{q}j), \quad (3.22)$$

where $\bar{e}(\bar{q}j) \equiv e(k\alpha \mid \bar{q}j)$ is the polarization vector satisfying the orthonormality and completeness relations, $e^{+}(\bar{q}j)e(\bar{q}j) = \delta_{jj'}$ where $j = 1,2,3.....3n$ labels the polarization branches.

We introduce a Dynamical Matrix, $D(\bar{q})$ given by

$$D_{\alpha\beta}(kk' \mid q) = \sum_{l'} \frac{\varphi_{\alpha\beta}(lk;l'k')}{\sqrt{m_k m_{k'}}} e^{-i\bar{q}.\left[\bar{R}(lk)-\bar{R}(l'k')\right]}. \quad (3.23)$$

The secular equation for the normal mode frequencies is written as

$$\sum_{l'\beta} \left[D_{\alpha\beta}(kk' \mid q) - \omega^2(\bar{q}j)\delta_{kk'}\delta_{\alpha\beta} \right] e(k\beta \mid \bar{q}j) = 0. \quad (3.24)$$

Also

$$\left[D(\bar{q}) - \omega^2(\bar{q}j)\mathrm{I} \right] e(\bar{q}j) = 0. \quad (3.25)$$

The necessary and sufficient condition to have a non-trivial solution is

$$\left[D(\bar{q}) - \omega^2(\bar{q}j)\mathrm{I} \right] = 0, \quad (3.26)$$

where I is the unit matrix of $3s \times 3s$ order[57]. For a particular wave-vector, q Eq.(3.26) gives $3s$ eigenvalues of $\omega^2(\bar{q}j)$.The acoustics branches correspond to the three roots that tend to zero as $q \to 0$. The remaining $3s-3$ are the optical branches which tend to a finite limit as, $q \to 0$, denoted as the Γ point of the Brillouin zone. These modes

are the only ones which can appear in first-order Raman spectra. The Fig.(3.1) below shows the phonon dispersion curve of Ge to show the triple degeneracy at Γ point.

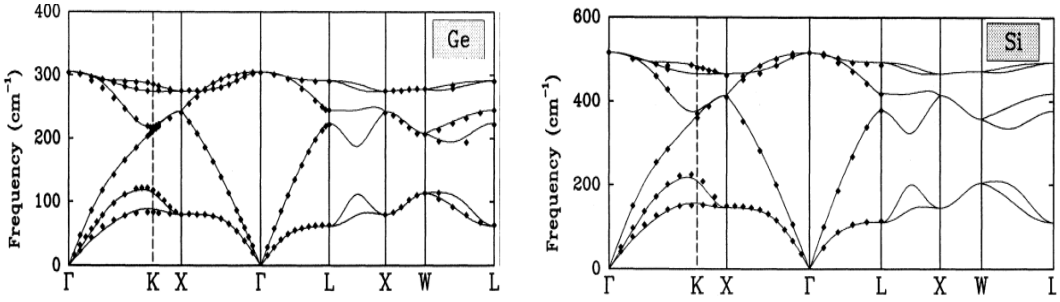

Fig(3.1): Phonon Dispersion[58] curve of Ge and Si. Copyright (1991) American Physical Society.

3.3 Classical theory of Raman Scattering

The classical theory of Raman Scattering[59] considers the appearance of an electric dipole moment induced by the electromagnetic field of the light incident on the system. This incident electric field is given by

$$E = E_L e^{-i\omega_L t} . \tag{3.27}$$

The induced dipole moment is expressed as

$$M_\alpha(t) = \sum_\beta P_{\alpha\beta} E_\beta = \sum_\beta P_{\alpha\beta}(u) E_{\beta L} e^{-i\omega_L t} , \tag{3.28}$$

where $P_{\alpha\beta}$ is the polarizabilty of the medium and ω_L is the frequency of incident light. Typically, the frequency of the incident radiation is much higher than that of the lattice vibrations but comparable to that of electronic transitions. Thus $P_{\alpha\beta}$ that appears in Eq.(3.28) is essentially the electronic polarizabilty tensor of the system. The atoms

vibrate about their equilibrium position $u=0$. This results in a variation of the polarizabilty, $P_{\alpha\beta}$ which can be expressed by expanding $P_{\alpha\beta}(u)$ about $u=0$ as

$$P_{\alpha\beta}(u)=P_{\alpha\beta}(0)+\sum_{k\gamma}\left(\frac{\partial P_{\alpha\beta}}{\partial u(k\gamma)}\right)_0 u(k\gamma)+\ldots\ldots \tag{3.29}$$

where $u(k\gamma)$ is the displacement of k^{th} atom in γ^{th} direction.

If the system vibrates such that f^{th} mode is excited, the atomic displacements can be written as

$$u(k\alpha|f)=\chi(k\alpha|f)cos\omega_f t\,. \tag{3.30}$$

where $\chi(k\alpha|f)$ defines the amplitude.

The induced polarization becomes

$$P_{\alpha\beta}(u)=P_{\alpha\beta}(0)+\frac{1}{2}\sum_{k\gamma}\left(\frac{\partial P_{\alpha\beta}}{\partial u(k\gamma)}\right)_0 \chi(k\alpha|f)\left(e^{-i\omega_f t}+e^{i\omega_f t}\right)+\ldots\ldots\ldots \tag{3.31}$$

The induced electronic dipole moment by the incident electric field can be written by substituting Eq.(3.31) into Eq.(3.28) as

$$\begin{aligned}M_\alpha(t)=&\sum_{\alpha\beta}P_{\alpha\beta}(0)E_{\beta L}e^{-i\omega_L t}\\&+\frac{1}{2}\sum_{\beta}\sum_{k\gamma}\left(\frac{\partial P_{\alpha\beta}}{\partial u(k\gamma)}\right)_0 \chi(k\alpha|f)E_{\beta L}\left(e^{-i(\omega_L+\omega_f)t}+e^{i(\omega_L-\omega_f)t}\right)+\ldots\ldots\end{aligned} \tag{3.32}$$

Eq.(3.32) shows the scattered radiation at three distinct frequencies, namely ω_L, $\omega_L + \omega_f$ and $\omega_L - \omega_f$. The first scattered frequency corresponds to elastic scattering (Rayleigh scattering), while the latter two frequencies, shifted to lower or higher frequencies correspond to inelastic scattering. The inelastic scattering is the first order Raman scattering, involving one phonon. The term $\omega_L - \omega_f$ gives the so-called Stokes scattering and $\omega_L + \omega_f$ corresponds to anti-Stokes scattering. The higher order terms in Eq.(3.32) correspond to second or higher order Raman scattering processes.

The vibrating classical dipole moment, $M_\alpha(t)$ radiates electromagnetic waves. The rate of energy flow is given by Poynting vector, $\bar{S}$ as

$$\bar{S} = \frac{\omega_L^4}{4\pi R^2 c^3} \sum_{\alpha\beta} \hat{n}_{s\alpha} \hat{n}_{s\beta} \overline{M_\alpha(t) M_\beta(t)}. \tag{3.33}$$

We obtain $\overline{M_\alpha(t) M_\beta(t)}$ from Eq.(3.28) as

$$\overline{M_\alpha(t) M_\beta(t)} = \frac{1}{4} \sum_{\gamma\mu} \left(P_{\alpha\gamma} P^*_{\beta\mu} + P^*_{\alpha\gamma} P_{\beta\mu} \right) E_{L\gamma} E_{L\mu}. \tag{3.34}$$

Hence the Poynting vector in Eq.(3.33) can be written as

$$\bar{S} = \frac{\omega_L^4}{16\pi R^2 c^3} \sum_{\alpha\beta\gamma\mu} \acute{n}_{s\alpha} \acute{n}_{s\beta} \left(P_{\alpha\gamma} P^*_{\beta\mu} + P^*_{\alpha\gamma} P_{\beta\mu} \right) E_{L\gamma} E_{L\mu}, \tag{3.35}$$

where n_s defines the polarization vector for scattered radiation at

position, R and c is the speed of light . The average power, $I(\bar{u})$ radiated per unit solid angle per unit volume is given by

$$I(\bar{u}) = \frac{\omega_L^4}{2\pi c^3} \sum_{\alpha\beta\gamma\mu} \acute{n}_{s\alpha} \acute{n}_{s\beta} P^*_{\alpha\gamma}(\bar{u}) P_{\beta\mu}(\bar{u}) E_{L\gamma} E_{L\mu} . \qquad (3.36)$$

The Eq.(3.36) would be used in the next section to discuss semi-classical theory of Raman scattering.

3.4 Semi-classical theory of Raman scattering

The semi-classical theory of Raman scattering[60] treats the lattice vibrations quantum mechanically while electromagnetic field is still a classical wave. As the atoms are free to vibrate, we consider the thermal average of the scattered intensity in Eq.(3.36) to be expressed as

$$I(\bar{u}) = \frac{\omega_L^4}{2\pi c^3} \sum_{\alpha\beta\gamma\mu} \acute{n}_{s\alpha} \acute{n}_{s\beta} \left\langle P^*_{\alpha\gamma}(\bar{u}) P_{\beta\mu}(\bar{u}) \right\rangle E_{L\gamma} E_{L\mu}. \qquad (3.37)$$

where,

$$\left\langle P^*_{\alpha\gamma}(\bar{u}) P_{\beta\mu}(\bar{u}) \right\rangle = \frac{1}{Z_{vib}} \sum_{vv'} e^{-\beta E_v} \left\langle v \mid P^*_{\alpha\gamma}(\bar{u}) \middle| v' \right\rangle \left\langle v' \middle| P_{\beta\mu}(\bar{u}) \middle| v \right\rangle , \qquad (3.38)$$

where Z_{vib} is the partition function, v is the initial and v' is the final vibrational state respectively. We now introduce a fourth rank Raman[61] tensor, $i_{\alpha\beta,\gamma\mu}(\omega)$ given as

$$i_{\alpha\beta,\gamma\mu}(\omega) = \frac{1}{Z_{vib}} \sum_{vv'} e^{-\beta E_v} \left\langle v \mid P^*_{\alpha\gamma}(\bar{u}) \middle| v' \right\rangle \left\langle v' \middle| P_{\beta\mu}(\bar{u}) \middle| v \right\rangle \delta(\omega - \omega_{vv'}). \qquad (3.39)$$

The delta function in Eq.(3.39) is given by

$$\delta(\omega-\omega_{vv'})=\frac{1}{2\pi}\int_{-\infty}^{+\infty}e^{-i(\omega-\omega_{vv'})t}dt\ . \tag{3.40}$$

Substituting Eq.(3.40) into Eq.(3.39), we obtain

$$i_{\alpha\beta,\gamma\mu}(\omega)=\frac{1}{2\pi}\int_{-\infty}^{+\infty}dte^{-i\omega t}\frac{1}{Z_{vib}}\sum_{vv'}e^{-\beta E_v}\langle v\,|\,P^*_{\alpha\gamma}(\bar{u})e^{i\omega_{vv'}t}\,|v'\rangle\langle v'|P_{\beta\mu}(\bar{u})|v\rangle, \tag{3.41}$$

where $\omega_{vv'}$ is the frequency difference between the initial and final vibrational states. The eigenvalue equation for Hamiltonian, H for any vibrational state is given by

$$H|v\rangle=E_v|v\rangle\equiv e^{\frac{iHt}{\hbar}}|v\rangle=e^{\frac{iE_vt}{\hbar}}|v\rangle\,. \tag{3.42}$$

Using Eq.(3.42) in Eq. (3.41), we have

$$i_{\alpha\beta,\gamma\mu}(\omega)=\frac{1}{2\pi}\int_{-\infty}^{+\infty}dte^{-i\omega t}\frac{1}{Z_{vib}}\sum_{vv'}e^{-\beta E_v}\langle v\,|\,e^{\frac{iHt}{\hbar}}P^*_{\alpha\gamma}(\bar{u})e^{\frac{-iHt}{\hbar}}\,|v'\rangle\langle v'|P_{\beta\mu}(\bar{u})|v\rangle \tag{3.43}$$

Using completeness relation and the Heisenberg representation:

$$\sum_{v'}|v'\rangle\langle v|=1 \tag{3.44}$$

and

$$P^*_{\alpha\gamma}(\bar{u},t)=e^{\frac{iHt}{\hbar}}P^*_{\alpha\gamma}(\bar{u})e^{\frac{-iHt}{\hbar}}, \tag{3.45}$$

the fourth rank Raman tensor in Eq.(3.43) is simplified to

$$i_{\alpha\beta,\gamma\mu}(\omega)=\frac{1}{2\pi}\int_{-\infty}^{+\infty}dte^{-i\omega t}P^{*}_{\alpha\gamma}(\bar{u},t)P_{\beta\mu}(\bar{u}). \qquad (3.46)$$

In the harmonic approximation, $P_{\alpha\gamma}(\bar{u})$ about the atomic equilibrium configuration $\bar{u}=0$ is given as

$$P_{\alpha\gamma}(\bar{u})=P_{\alpha\gamma}(\bar{0})+\sum_{k\delta}P_{\alpha\gamma}(k\delta)\bar{u}(k\delta)+\ldots\ldots\ldots \qquad (3.47)$$

where $P_{\alpha\gamma}(k\delta)=\left[\frac{\partial P_{\alpha\gamma}(\bar{u})}{\partial u(k\delta)}\right]_{u=0}$

In normal co-ordinates, $\boldsymbol{u}=\sum_{f=1}^{3N}\chi(f)d_f$ Eq.(3.47) is written as

$$P_{\alpha\gamma}(\bar{u})=P_{\alpha\gamma}(\bar{0})+\sum_{f=1}^{3N}P_{\alpha\gamma,f}d_f+\ldots\ldots\ldots \qquad (3.48)$$

where $P_{\alpha\gamma,f}=\tilde{P}_{\alpha\gamma}\chi(f)=\sum_{k\delta}P_{\alpha\gamma}(k\delta)\chi(k\delta\,|\,f)=\left[\frac{\partial P_{\alpha\gamma}}{\partial d_f}\right]_0$,is the electronic polarizabilty per unit displacement in the normal mode f. Finally we obtain the fourth rank Raman tensor as

$$i_{\alpha\gamma,\beta\mu}(\omega)=\frac{1}{2\pi}\int_{-\infty}^{+\infty}dte^{-i\omega t}\begin{bmatrix}P^{*}_{\alpha\gamma}(0)P_{\beta\mu}(0)\\ +\sum_{f}\begin{Bmatrix}P^{*}_{\alpha\gamma}(0)P_{\beta\mu,f}(0)\langle d_f\rangle\\ +P^{*}_{\alpha\gamma,f}(0)P_{\beta\mu}(0)\langle d_f(t)\rangle\end{Bmatrix}\\ +\sum_{ff'}P^{*}_{\alpha\gamma,f}P_{\beta\mu,f}\langle d_f(t)d_{f'}\rangle\end{bmatrix}. \qquad (3.49)$$

The first term in Eq. (3.49) corresponds to Rayleigh scattering. The Second and third term would vanish since $\langle d_f\rangle=0=\langle d_f(t)\rangle$. Thus the

only term which contributes to Raman scattering is the last term. The fourth rank Raman tensor corresponding to this scattering reduces to

$$I(\omega) = \frac{1}{2\pi}\int_{-\infty}^{+\infty} dt e^{-i\omega t} \sum_{ff'} P^{*}_{\alpha\gamma,f} P_{\beta\mu,f} \left\langle d_f(t) d_{f'} \right\rangle . \qquad (3.50)$$

In the harmonic approximation, the normal coordinates are given by $d_f = i\sqrt{\hbar/2m}\left(a_f e^{-i\omega_f t} - a_f^{+} e^{i\omega_f t}\right)$, where a_f and a_f^{+} are creation and annihilation operators. Therefore, if we now consider the thermal averaging of $\left\langle d_f(t) d_{f'} \right\rangle$, we find as:

$\left\langle d_f(t) d_{f'} \right\rangle = \delta_{ff'}\left(\hbar/2m\right)\left[\left(\left\langle n_f \right\rangle + 1\right)e^{-i\omega_f t} + \left\langle n_f \right\rangle e^{i\omega_f t}\right]$, where n_f is the conventional Bose-Einstein occupation function. Moreover if we apply the delta function properties given by $\delta(\omega_f + \omega) = \frac{1}{2\pi}\int_{-\infty}^{+\infty} e^{-i(\omega_f+\omega)t}$ and $\delta(\omega_f - \omega) = \frac{1}{2\pi}\int_{-\infty}^{+\infty} e^{i(\omega_f-\omega)t}$ to Eq.(3.50), the final expression for the fourth rank Raman tensor is given by

$$i_{\alpha\gamma,\beta\mu}(\omega) = \hbar\sum_{f} \frac{P^{*}_{\alpha\gamma,f} P_{\beta\mu,f}}{2\omega_f}\left[\left(\left\langle n_f \right\rangle + 1\right)\delta(\omega_f + \omega) + \left\langle n_f \right\rangle \delta(\omega_f - \omega)\right] . \qquad (3.51)$$

The term proportional to $\delta(\omega_f - \omega)$ corresponds to the Stokes scattering component and that proportional to $\delta(\omega_f + \omega)$ corresponds to anti-Stokes component of Raman Scattering. The frequency of the

electromagnetic radiation emitted by the system is $\omega_s = \omega_L \pm \omega_f$. The Stokes and anti-Stokes components correspond to emission, $(\omega_s = \omega_L - \omega_f)$ and absorption, $(\omega_s = \omega_L + \omega_f)$ of a phonon, respectively. The expression for the intensity of the scattered radiation can be written as

$$I(\bar{u}) = \frac{\hbar}{2\pi c^3} \sum_f \frac{\omega_S^4}{2\omega_f} \begin{bmatrix} \langle (n_f + 1) \rangle \delta(\omega_f + \omega) \\ + \langle n_f \rangle \delta(\omega_f - \omega) \end{bmatrix} \sum_{\alpha\beta\gamma\mu} \acute{n}_{s\alpha} \acute{n}_{s\beta} P^*_{\alpha\gamma,f}(\bar{u}) P_{\beta\mu,f}(\bar{u}) E_{L\gamma} E_{L\mu}, \tag{3.52}$$

where n_S is the scattered polarization vector .

The corresponding differential scattering cross section can be written as

$$\frac{d^2\sigma}{d\Omega d\omega_S} = \frac{\hbar}{c^4} \sum_f \frac{\omega_S^4}{2\omega_f} \left[\langle (n_f + 1) \rangle \delta(\omega_f + \omega) + \langle n_f \rangle \delta(\omega_f - \omega) \right] \left| \sum_{\alpha\beta} n_{S\alpha} P_{\alpha\beta,f} n_{L\beta} \right|^2, \tag{3.53}$$

where n_L is the incident polarization vector. The differential scattering cross-section expression will be used to describe the depolarization ratio and the selection rules of Raman scattering.

3.5 Quantum theory of Raman Scattering

The quantum theory of Raman scattering[62,63] considers the quantization of lattice vibrations and the quantization of the

electromagnetic field. The Hamiltonian of solids in an interacting with an electromagnetic field is written as

$$H = H_e + H_i + H_{ei} + H_p + H_{ip} + H_{ep}, \tag{3.54}$$

where H_e, H_i and H_p are the Hamiltonian of the electrons , ions and photons respectively. H_{ei}, H_{ip} and H_{ep} corresponds to electron-ion, ion-photon and electron-photon interactions. The ion-photon interaction is negligible if the excitation frequency is large. $H_e + H_i + H_p + H_{ei}$ are treated exactly within harmonic approximation, representing the unperturbed Hamiltonian, $H_0 = p^2/2m + V(\bar{r})$ where p is the momentum of electron and $V(\bar{r})$ is the crystalline potential experienced by the electron. The photon Hamiltonian, H_p is given by

$$H_p = \sum_k \hbar\omega_{\bar{k}} \left(a_{\bar{k}}^{+} a_{\bar{k}} + \frac{1}{2} \right). \tag{3.55}$$

We now consider the coulomb gauge[64] $(\nabla . A = 0)$, where A is the vector potential. The electric and magnetic field of the electromagnetic wave are given by Maxwell's equations as $E = -(1/c)(\partial A/\partial t)$ and $B = \nabla \times A$ respectively. Hence the expression for the wave equation of the vector potential is $\nabla^2 A - (1/c^2)(\partial^2 A/\partial t^2) = 0$ and its solution is given as

$$A(r,t) = \frac{1}{2} \sum_{\bar{k}} \left[A_{\bar{k}} e^{i(\bar{k}.\bar{r} - \omega_{\bar{k}} t)} + A_{\bar{k}}^{*} e^{-i(\bar{k}.\bar{r} - \omega_{\bar{k}} t)} \right] \hat{e}_k . \tag{3.56}$$

where $\hat{e}_k$ is a unit polarization vector .

The electric field is then

$$E(r,t) = \frac{1}{2}\sum_{\bar{k}} \frac{i\omega_{\bar{k}}}{c}\left[A_{\bar{k}} e^{i(\bar{k}.\bar{r}-\omega_{\bar{k}}t)} - A^{*}_{\bar{k}} e^{-i(\bar{k}.\bar{r}-\omega_{\bar{k}}t)} \right]\hat{e}_k. \qquad (3.57)$$

Accordingly, the quantization rules for the radiation field leads to the following expressions for the vector potential and electric field operators:

$$A(r,t) = \frac{1}{2}\sum_{\bar{k}} A(\omega_{\bar{k}})\left[a_{\bar{k}} e^{i(\bar{k}.\bar{r}-\omega_{\bar{k}}t)} + a^{+}_{\bar{k}} e^{-i(\bar{k}.\bar{r}-\omega_{\bar{k}}t)} \right]\hat{e}_k \qquad (3.58)$$

and

$$E(r,t) = \frac{1}{2}\sum_{\bar{k}} \frac{i\omega_{\bar{k}}}{c}\left[A_{\bar{k}} e^{i(\bar{k}.\bar{r}-\omega_{\bar{k}}t)} - A^{*}_{\bar{k}} e^{-i(\bar{k}.\bar{r}-\omega_{\bar{k}}t)} \right]\hat{e}_k \qquad (3.59)$$

respectively.

Here $A(\omega_{\bar{k}}) = \left(\frac{2\pi\hbar c^2}{\omega_{\bar{k}} V} \right)^{\frac{1}{2}}$ and $E(\omega_{\bar{k}}) = i\left(\frac{2\pi\hbar\omega_{\bar{k}}}{V} \right)^{\frac{1}{2}}$.

The amplitude of the quantized electric and vector potential fields is given by $|A(\omega_{\bar{k}})| = |E(\omega_{\bar{k}})|/k$. In the presence of electromagnetic field the momentum operator transforms as $p \to p + e\bar{A}/c$. The total Hamiltonian would then be given by

$$H = H_0 + H_{int}, \qquad (3.60)$$

where $H_{int} = \sum_i \frac{e}{mc} \bar{A}.\bar{p}_i$.

Within the dipole approximation the phase factor is taken $e^{\pm ik.r} \approx 1$, a plane wave solution. Hence we can write Eq.(3.59) as $E(r,t) = \sum_k i\left(2\pi\hbar\omega_k / V\right)^{1/2}\left(a_k - a_k^+\right)\hat{e}$. Also the term $\bar{A}.\bar{p}$ is similar to the perturbation term $-\bar{M}.\bar{E}$ where $\bar{M} = \sum_j q_j \bar{r}_j$, is the electric dipole moment. Hence switching from an $\bar{A}.\bar{p}$ to $-\bar{M}.\bar{E}$ formulation would give the same inelastic scattering cross section. The total Hamiltonian becomes

$$H = H_0 - \bar{M}.\bar{E}\,, \tag{3.61}$$

or

$$H = H_0 - \sum_k i\left[\frac{2\pi\hbar\omega_k}{V}\right]^{\frac{1}{2}} \bar{M}.\hat{e}\left(a_k - a_k^+\right). \tag{3.62}$$

The first order Raman scattering involves creation and destruction of two photons in ground, $|n\rangle$ and excited, $|m\rangle$ electronic state along with a phonon. Fermi's golden rule, also known as transition rate formula[65], gives

$$\Gamma = \frac{2\pi}{\hbar}\left|\sum_b \frac{\langle c|H_{\text{int}}|b\rangle\langle b|H_{\text{int}}|a\rangle}{E_a - E_b}\right|^2 \delta\left(E_c - E_a\right), \tag{3.63}$$

where the transition states $|a\rangle$, $|b\rangle$ and $|c\rangle$ are the initial, intermediate and final states respectively. Let us assume the initial photon state to be $|n_k\rangle$ and the final photon state to be $|n_{k'}\rangle$. The initial

state can be written as $|a\rangle = |n\rangle|n_k\rangle|n_{k'}=0\rangle$ with energy $E_a = E_n + n_k\hbar\omega_k$. Similarly the final state is $|c\rangle = |m\rangle|n_k - 1\rangle|n_{k'}=1\rangle$ with energy $E_c = E_m + (n_k - 1)\hbar\omega_k + \hbar\omega_{k'}$. The first and second matrix element gives two possibilities of the intermediate state. These two possibilities for the intermediate states are $|l\rangle|n_k - 1\rangle|n_{k'}=0\rangle$ and $|l\rangle|n_k\rangle|n_{k'}=1\rangle$ with energy $E_b = E_l + \hbar\omega_k(n_k - 1)$ and $E_b = E_l + \hbar\omega_k n_k + \hbar\omega_{k'}s$ respectively. Let us denote ω_L and ω_S as the incident photon and scattered frequency, the transition rate can then be written as

$$\Gamma = \frac{2\pi}{\hbar}\left(\frac{2\pi\hbar}{V}\right)^2 \sum_{k_s}\omega_L\omega_S n_k \left| \sum_l \left(\begin{array}{c} \dfrac{\langle m|\mathrm{M}.\hat{e}'|l\rangle\langle l|\bar{M}.\hat{e}|n\rangle}{E_l - E_n - \hbar\omega_L} \\ + \dfrac{\langle m|\mathrm{M}.\hat{e}'|l\rangle\langle l|\bar{M}.\hat{e}|n\rangle}{E_l - E_n + \hbar\omega_S} \end{array} \right) \right|^2 \times \delta\left(E_m - E_n - \hbar(\omega_L - \omega_S)\right). \tag{3.64}$$

The summation over k_S is converted into an integral of the form

$$\sum_{k_S} \to \left(V/(2\pi)^3\right)\iint k_S^2 dk_S d\Omega = \left(V/(2\pi c)^3\right)\iint \omega_S^2 d\omega_S d\Omega \tag{3.65}$$

The scattering rate[66] is best given as a scattering cross-section. The scattering rate is given by

$$\sigma = \frac{\hbar\omega_S\Gamma}{\left(\dfrac{c\hbar\omega_S n_k}{V}\right)} = \frac{V\Gamma}{cn_k}. \tag{3.66}$$

Hence the Raman cross-section can be written as

$$\left(\frac{d^2\sigma}{d\Omega d\omega_S}\right)_{\hat{e}\hat{e}'} = \frac{\hbar\omega_L\omega_S^3}{c^4}\left|\sum_l\left(\frac{\langle m|\bar{M}.\hat{e}'|l\rangle\langle l|\bar{M}.\hat{e}|n\rangle}{E_l - E_n - \hbar\omega_L} + \frac{\langle m|\bar{M}.\hat{e}|l\rangle\langle l|\bar{M}.\hat{e}'|n\rangle}{E_l - E_n + \hbar\omega_S}\right)\right|^2 \times\delta\left[E_m - E_n - \hbar(\omega_L - \omega_S)\right].$$

(3.67)

Using $\hbar\omega_{ln} = E_l - E_n$ and $\left[E_m - E_n - \hbar(\omega_L - \omega_S)\right] = \frac{1}{\hbar}\delta\left[\omega_{mn} - (\omega_L - \omega_S)\right]$

in Eq.(3.67) , we get

$$\left(\frac{d^2\sigma}{d\Omega d\omega_S}\right)_{\hat{e}\hat{e}'} = \frac{\omega_L\omega_S^3}{\hbar^2c^4}\left|\sum_l\left(\frac{\langle m|\bar{M}.\hat{e}'|l\rangle\langle l|\bar{M}.\hat{e}|n\rangle}{\omega_{ln} - \omega_L} + \frac{\langle m|\bar{M}.\hat{e}|l\rangle\langle l|\bar{M}.\hat{e}'|n\rangle}{\omega_{ln} + \omega_S}\right)\right|^2 \times\delta\left[\omega_{mn} - (\omega_L - \omega_S)\right]$$

(3.68)

Eq.(3.68) is the *Kramers-Heisenberg*[67] formula for differential scattering cross-section. A thermal averaging $(Av)_n$ is included over all the initial states, and then the Raman cross section is given by

$$\left(\frac{d^2\sigma}{d\Omega d\omega_S}\right)_{\hat{e}\hat{e}'} = \frac{\omega_L\omega_S^3}{\hbar^2c^4}(Av)_n\sum_m\left|\sum_l\left(\frac{\langle m|\bar{M}.\hat{e}'|l\rangle\langle l|\bar{M}.\hat{e}|n\rangle}{\omega_{ln} - \omega_L} + \frac{\langle m|\bar{M}.\hat{e}|l\rangle\langle l|\bar{M}.\hat{e}'|n\rangle}{\omega_{ln} + \omega_S}\right)\right|^2 \times\delta\left[\omega_{mn} - (\omega_L - \omega_S)\right].$$

(3.69)

The first term is known as resonant term[68] and the second as anti-resonant term. $\bar{M}.\hat{e}$ and $\bar{M}.e'$ is the electric dipole interaction for the

incident and scattered polarizations respectively. If $\omega_L \sim \omega_{\ln}$, we observe an occurrence of resonance in Raman cross-section.

3.6 Raman Selection Rules

The Raman intensity depends on the polarizations of the incident and scattered light. From Eq.(3.53),

$$I \propto \left| \sum_{\alpha\beta} n_S . P_{\alpha\beta,f} . n_L \right|^2 , \tag{3.70}$$

where $P_{\alpha\beta,f}$ is the polarizabilty derivative of the molecule; and n_L and n_s are the incident and scattered polarization vector respectively. The polarizabilty is directly proportional to electronic susceptibility, χ of the molecule as $P = \chi E$. The volume-independent Raman tensor, R is introduced such that the susceptibility derivative, χ is written in terms of R [69] as

$$\chi = \frac{1}{v_c} \sqrt{\frac{1}{\mu N}} R \tag{3.71}$$

where v_c, μ is the volume and reduced mass of primitive cell respectively. The Raman strength can now be expressed as

$$I \propto \left| n_s . R . n_L \right|^2 . \tag{3.72}$$

In diamond-structure semiconductors, the optical modes at the Γ point (k = 0) the Brillouin zone are triply degenerate, and a basis

can be chosen with modes polarized along x, y and z directions. The Raman tensor[70] for these modes is given by

$$R(x)=\begin{pmatrix}0 & 0 & 0\\ 0 & 0 & d\\ 0 & d & 0\end{pmatrix}, \tag{3.73}$$

$$R(y)=\begin{pmatrix}0 & 0 & d\\ 0 & 0 & 0\\ d & 0 & 0\end{pmatrix} \tag{3.74}$$

and

$$R(z)=\begin{pmatrix}0 & d & 0\\ d & 0 & 0\\ 0 & 0 & 0\end{pmatrix}. \tag{3.75}$$

Using *Porto* convention[71], $k_L(\hat{n}_L,\hat{n}_S)k_S$ for the scattering geometry where k_L and k_S indicates the propagation directions of incident and scattered light. $\hat{n}_L$ and $\hat{n}_S$ gives the polarization directions of incident and scattered light respectively. Consider a parallel configuration, $z(x,x)-z$ and perpendicular configuration, $z(x,y)-z$ geometries for diamond type (Si, Ge) structures. The Raman intensity for perpendicular geometry is given by

$$I_{z(x,y)-z}\propto\left|\begin{pmatrix}1 & 0 & 0\end{pmatrix}\begin{pmatrix}0 & d & 0\\ d & 0 & 0\\ 0 & 0 & 0\end{pmatrix}\begin{pmatrix}0\\ 1\\ 0\end{pmatrix}\right|^2\propto|d|^2. \tag{3.76}$$

And the Raman intensity for parallel geometry is given by

$$I_{z(x,x)-z} \propto \left| \begin{pmatrix} 1 & 0 & 0 \end{pmatrix} \begin{pmatrix} 0 & d & 0 \\ d & 0 & 0 \\ 0 & 0 & 0 \end{pmatrix} \begin{pmatrix} 1 \\ 0 \\ 0 \end{pmatrix} \right|^2 = 0. \tag{3.77}$$

3.7 Strain effects on Optical Phonon

In diamond type crystals, we observe that first order Stokes Raman spectra exhibits a single peak a Γ point. The three degenerate optical phonon at $k = 0$ are found at a frequency ω_0 , so that $\omega_0 = \omega_L - \omega_s$, where ω_L is the frequency of incident radiation and ω_s, is the frequency of scattered radiation. The application of uniaxial stress would cause shift and splitting of the degenerate optical modes. The coupled dynamical equations describing the optical modes in strain[72] is given

$$\bar{m}\ddot{u}_i = \sum_{klm} \bar{m}\left(\omega_0^2 \delta_{ik} + K_{iklm}\varepsilon_{lm}\right)u_k \tag{3.78}$$

where $\bar{m}$ is the reduced mass of the system, u_i is the relative displacement of the i^{th} component, δ_{ik} is the Kronecker delta, ε_{lm} is the applied strain and K_{iklm} are the components of the fourth rank deformation potential tensor. K_{iklm} has exactly same symmetry properties as the c_{iklm}. In suppressed index notation, K_{iklm} matrix in

Cartesian coordinates for cubic crystals are given by

$$\begin{aligned} K_{11} &= K_{22} = K_{33} = p \\ K_{12} &= K_{23} = K_{13} = q \ . \\ K_{66} &= K_{44} = K_{55} = r \end{aligned} \tag{3.79}$$

In suppressed notation we can rewrite Eq.(3.78) as

$$\ddot{u}_i = \sum_k \left(\omega_0^2 \delta_{ik} + K_{ik} \right) u_k \, . \tag{3.80}$$

Assuming the solutions of Eq.(3.80) of the form $u_i = A_i e^{i\omega t}$. We obtain

$$\sum_k \left[K_{ik} + \left(\omega_0^2 - \omega^2 \right) \delta_{ik} \right] A_k = 0 \, . \tag{3.81}$$

The non-trivial solution, if the determinant of the matrix in brackets vanishes, is given by the well-known secular equation [73]

$$\begin{vmatrix} K_{11} + \left(\omega_0^2 - \omega^2 \right) & K_{12} & K_{13} \\ K_{21} & K_{22} + \left(\omega_0^2 - \omega^2 \right) & K_{23} \\ K_{31} & K_{32} & K_{33} + \left(\omega_0^2 - \omega^2 \right) \end{vmatrix} = 0. \tag{3.82}$$

We define $\lambda = \omega^2 - \omega_0^2$, then Eq.(3.82) is given by

$$\begin{vmatrix} K_{11} - \lambda & K_{12} & K_{13} \\ K_{21} & K_{22} - \lambda & K_{23} \\ K_{31} & K_{32} & K_{33} - \lambda \end{vmatrix} = 0 \, . \tag{3.83}$$

In Cartesian coordinates the elements of the determinant in Eq. (3.83) are given by

$$\begin{aligned} K_{11} &= p\varepsilon_{11} + q\left(\varepsilon_{22} + \varepsilon_{33}\right) \\ K_{22} &= p\varepsilon_{22} + q\left(\varepsilon_{11} + \varepsilon_{33}\right) \\ K_{33} &= p\varepsilon_{33} + q\left(\varepsilon_{11} + \varepsilon_{22}\right). \\ K_{12} &= K_{21} = 2r\varepsilon_{12} \\ K_{23} &= K_{32} = 2r\varepsilon_{23} \end{aligned} \tag{3.84}$$

We will further relate the Cartesian crystal cubic coordinates of the above analysis with the cylindrical coordinates that was used in Chapter 2 to compute the strain in the nanowires in Chapter 4 and Chapter 5.

3.8 Raman Experimental Setup

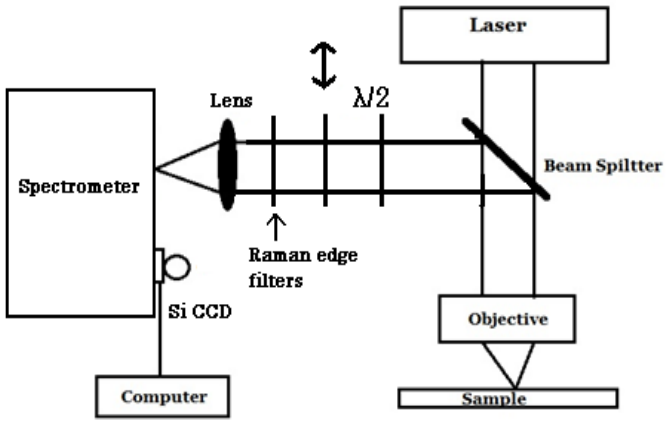

Fig.(3.2): Raman experiment set-up in the back-scattering process.

The micro-Raman experimental setup is shown in Fig (3.2). The apparatus has four important components: (1)Laser, (2) Spectrometer, (3) Objective and (4) Charged –coupled device (CCD). It is operated in

the back-scattering configuration. The photon excitation source is a single line mode of either an Argon or Krypton ion laser with wavelengths in the visible region. The incident laser excitation travels through the beam splitter, is focused on the sample by a microscope objective. The objective is a 100 X with 0.8NA and yields a spot size less than 1micron. The objective collects the scattered light where a half wave plate selects which polarization passes to the spectrometer and a Raman edge filters reject the Rayleigh scattered light. The spectrometer used is a single stage Acton 500mm Spectrometer. It has 600, 1200 and 2400 grooves/mm gratings. The collected scattered light is energy dispersed by the spectrometer and its intensity versus energy spectra is measured with a liquid nitrogen cooled Si CCD detector. The spectrum is collected with the computer using the Winspec32 [74]software.

CHAPTER 4

ANALYTICAL MODELLING OF STRAIN-INDUCED RAMAN SHIFTS IN CORE-SHELL NANOWIRE

4.1 Introduction

An analytical model[40] is now introduced to compute the Raman spectrum of Si-Ge core shell nanowires. For the calculation of the strain, the materials are assumed to be elastically isotropic. In this chapter we combine the strain calculations of Chapter 2 with the theory of strain effects on Raman frequencies from Chapter 3 to obtain simple predictions of the phonon frequencies in core-shell nanowires with axes along the <011> and <111> crystallographic directions. We start the discussion with the strain model of core-shell nanowire followed by the optical phonon discussions in core-shell nanowire with axes along the <011> and <111> directions. Later sections describe the numerical simulations and their results with discussions.

4.2 The Strain model

In chapter 2 we derived the strain equations of the core-shell nanowire[47] with different elastic properties and introduced a relaxation term of core and shell. We considered different Young's moduli for the core and shell. Also since *ratios* of elastic constants are nearly the same for Si and Ge, their corresponding Poisson ratios are

very similar for any fixed crystallographic orientation.[75] Hence we kept the Poisson's ratio to be same for the core and shell. The expressions of core and shell strains with no relaxation term i.e. $\rho = 0$ can be obtained from Eq.(2.78) and Eq.(2.79), are given by

$$\varepsilon_{rr}^{\text{core}}\left(r,\theta,z\right) = -\varepsilon_{\text{misfit}}\left(a^2 - c^2\right)\left\{\frac{\left(\nu+1\right)\left(1-2\nu\right)}{\left(1-\gamma\right)\left(1-2\nu\right)c^2 - \left(1-2\nu+\gamma\right)a^2} + \frac{\nu}{\left(a^2-c^2\right)+\gamma c^2}\right\}, \tag{4.1}$$

$$\varepsilon_{\theta\theta}^{\text{core}}\left(r,\theta,z\right) = \varepsilon_{rr}^{\text{core}}\left(r,\theta,z\right), \tag{4.2}$$

$$\varepsilon_{zz}^{\text{core}}\left(r,\theta,z\right) = \varepsilon_{\text{misfit}}\left[\frac{\left(a^2-c^2\right)}{\left(a^2-c^2\right)+\gamma c^2}\right], \tag{4.3}$$

$$\varepsilon_{rr}^{\text{shell}}\left(r,\theta,z\right) = \frac{\varepsilon_{\text{misfit}}\left(\nu+1\right)\gamma c^2}{\left(1-\gamma\right)\left(1-2\nu\right)c^2 - \left(1-2\nu+\gamma\right)a^2}\left[\left(1-2\nu\right) - \frac{a^2}{r^2}\right] + \frac{\nu\gamma c^2\varepsilon_{\text{misfit}}}{\left(a^2-c^2\right)+\gamma c^2}, \tag{4.4}$$

$$\varepsilon_{\theta\theta}^{\text{shell}}\left(r,\theta,z\right) = \frac{\varepsilon_{\text{misfit}}\left(\nu+1\right)\gamma c^2}{\left(1-\gamma\right)\left(1-2\nu\right)c^2 - \left(1-2\nu+\gamma\right)a^2}\left[\left(1-2\nu\right) + \frac{a^2}{r^2}\right] + \frac{\nu\gamma c^2\varepsilon_{\text{misfit}}}{\left(a^2-c^2\right)+\gamma c^2}, \tag{4.5}$$

$$\varepsilon_{zz}^{\text{shell}}\left(r,\theta,z\right) = -\frac{\gamma c^2\varepsilon_{\text{misfit}}}{\left(a^2-c^2\right)+\gamma c^2}. \tag{4.6}$$

The Fig. 1 shows the non-zero strain components for a Ge-Si core shell nanowire with c/a =0.6.

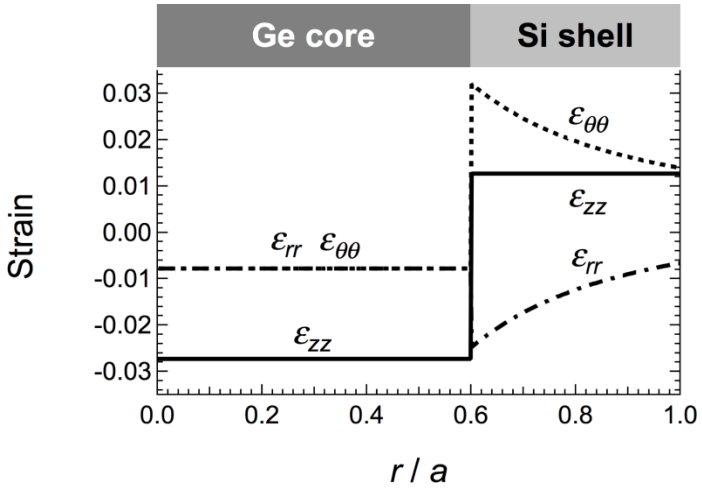

Fig.(4.1): Strain tensor components in cylindrical coordinates for a fully strained Ge-Si core shell nanowire with $c/a = 0.6$, where c is the core radius and a the outer shell radius.

Since the strain components are independent of θ, we plot them as a function of the radial coordinate r. In the core region, the strain tensor is independent of r. This perfectly uniform strain splits the triple-degenerate Γ point optical phonon mode of the diamond structure into three unique modes, which therefore become an ideal probe of the strain state of the core via Raman spectroscopy. By contrast, the off-axis shell strain components are functions r, so that the observed shell Raman spectrum is an average over the shell. In addition, shells in real nanowires tend to be quite thin, so that confinement effects on their phonon frequencies must be fully included. Because of these complications, the shell Raman spectrum is less appropriate for strain characterization. Thus we will concentrate on Raman spectra from the

core regions. The elastic constants and structural parameters were taken from Table 4.1 given below:

Table 4.1 : Structural and elastic parameters used for the computation of the strain in Si-Ge and Ge-Si core-shell nanowires.

	Lattice constant (Å)	ν (Voigt average)	E_{011} (GPa)	E_{111} (GPa)
Si	5.43086[76]	0.218[77]	169.2[78]	187.9[78]
Ge	5.6568[76]	0.200[77]	137.0[78]	154.5[78]

4.3 Optical Phonons in <011> and <111> Nanowire core

We consider nanowires grown in <011> and <111> directions. To transform the deformation potential tensor to cylindrical coordinates, we define an intermediate Cartesian system with the z–axis along the nanowire growth axis. Also the unperturbed $(K_{iklm} = 0)$ phonon eigenvectors are considered to be along

$$\begin{aligned} e_1 &= (1,0,0) \\ e_2 &= (0,1,0), \\ e_3 &= (0,0,1) \end{aligned} \tag{4.7}$$

where e_2 ,e_2 and e_3 are unit vectors for the Cartesian coordinate system relative to the cubic *x, y* and *z* axes.

We use the definition of transformation matrix, $l_{ij} = e_i . e_{(r\theta z)}$, where $e_{(r\theta z)}$ are the unit vectors in cylindrical system and e_i is analogous to Eq.(4.7) to find the transformation matrix, l_{ij}. We start first by taking the growth axis of the nanowire along the (011)

crystalline direction. We define an auxiliary coordinate system with unit vectors given as

$$\begin{aligned} e_1^{aux} &= (1,0,0) \\ e_2^{aux} &= \left(0,\frac{1}{\sqrt{2}},-\frac{1}{\sqrt{2}}\right). \\ e_3^{aux} &= \left(0,\frac{1}{\sqrt{2}},\frac{1}{\sqrt{2}}\right) \end{aligned} \tag{4.8}$$

The unit vector for the cylindrical system is written in terms of these auxiliary vectors as

$$\begin{aligned} e_r &= \cos\theta e_1^{aux} + \sin\theta e_2^{aux} \\ e_\theta &= -\sin\theta e_1^{aux} + \cos\theta e_2^{aux} \\ e_z &= e_3^{aux} \end{aligned} . \tag{4.9}$$

We thus obtain the transformation matrix as

$$\left[l_{ij}\right] = \begin{pmatrix} \cos\theta & -\sin\theta & 0 \\ \dfrac{\sin\theta}{\sqrt{2}} & \dfrac{\cos\theta}{\sqrt{2}} & \dfrac{1}{\sqrt{2}} \\ -\dfrac{\sin\theta}{\sqrt{2}} & -\dfrac{\cos\theta}{\sqrt{2}} & \dfrac{1}{\sqrt{2}} \end{pmatrix}. \tag{4.10}$$

Using Eq.(2.10) of chapter 2, and Eq.(4.10) , we have

$$\left[\varepsilon\right] = \left[1\right]\left[\varepsilon''\right]\left[1\right]^T = \begin{pmatrix} \cos\theta & -\sin\theta & 0 \\ \dfrac{\sin\theta}{\sqrt{2}} & \dfrac{\cos\theta}{\sqrt{2}} & \dfrac{1}{\sqrt{2}} \\ -\dfrac{\sin\theta}{\sqrt{2}} & -\dfrac{\cos\theta}{\sqrt{2}} & \dfrac{1}{\sqrt{2}} \end{pmatrix} \begin{pmatrix} \varepsilon_{rr} & 0 & 0 \\ 0 & \varepsilon_{\theta\theta} & 0 \\ 0 & 0 & \varepsilon_{zz} \end{pmatrix} \begin{pmatrix} \cos\theta & \dfrac{\sin\theta}{\sqrt{2}} & -\dfrac{\sin\theta}{\sqrt{2}} \\ -\sin\theta & \dfrac{\cos\theta}{\sqrt{2}} & -\dfrac{\cos\theta}{\sqrt{2}} \\ 0 & \dfrac{1}{\sqrt{2}} & \dfrac{1}{\sqrt{2}} \end{pmatrix} \tag{4.11}$$

In the core region of the nanowire, $\varepsilon_{rr}^{core} = \varepsilon_{\theta\theta}^{core}$ thus we have from Eq.(4.15)

$$\begin{pmatrix} \varepsilon_{11} & \varepsilon_{12} & \varepsilon_{13} \\ \varepsilon_{12} & \varepsilon_{22} & \varepsilon_{23} \\ \varepsilon_{13} & \varepsilon_{23} & \varepsilon_{33} \end{pmatrix} = \frac{1}{2}\begin{pmatrix} 2\varepsilon_{\theta\theta}^{core} & 0 & 0 \\ 0 & \varepsilon_{rr}^{core} + \varepsilon_{zz}^{core} & \varepsilon_{zz}^{core} - \varepsilon_{rr}^{core} \\ 0 & \varepsilon_{zz}^{core} - \varepsilon_{rr}^{core} & \varepsilon_{zz}^{core} + \varepsilon_{rr}^{core} \end{pmatrix} \quad (4.12)$$

is independent of the angle θ. Therefore, Eq.(3.83) from Section[3.7] becomes

$$\begin{vmatrix} p\varepsilon_{rr}^{core} + q\left(\varepsilon_{rr}^{core} + \varepsilon_{zz}^{core}\right) - \lambda & 0 & 0 \\ 0 & \begin{pmatrix} \frac{1}{2}p\left(\varepsilon_{rr}^{core} + \varepsilon_{zz}^{core}\right) \\ +\frac{1}{2}q\left(3\varepsilon_{rr}^{core} + \varepsilon_{zz}^{core}\right) \end{pmatrix} - \lambda & r\left(\varepsilon_{zz}^{core} - 2\varepsilon_{rr}^{core}\right) \\ 0 & r\left(\varepsilon_{zz}^{core} - 2\varepsilon_{rr}^{core}\right) & \begin{pmatrix} \frac{1}{2}p\left(\varepsilon_{rr}^{core} + \varepsilon_{zz}^{core}\right) \\ +\frac{1}{2}q\left(3\varepsilon_{rr}^{core} + \varepsilon_{zz}^{core}\right) \end{pmatrix} - \lambda \end{vmatrix} = 0 \quad (4.13)$$

This has the following eigenvalues and eigenvectors

$$\begin{aligned} \lambda_1 &= \left(p+q\right)\varepsilon_{rr}^{\text{core}} + q\varepsilon_{zz}^{\text{core}}; \quad \mathbf{u}_1' = \left(1,0,0\right) \\ \lambda_2 &= \left(\frac{1}{2}p + \frac{3}{2}q - r\right)\varepsilon_{rr}^{\text{core}} + \left(\frac{1}{2}p + \frac{1}{2}q + r\right)\varepsilon_{zz}^{\text{core}}; \quad \mathbf{u}_2' = \left(0, \frac{1}{\sqrt{2}}, \frac{1}{\sqrt{2}}\right) \\ \lambda_3 &= \left(\frac{1}{2}p + \frac{3}{2}q + r\right)\varepsilon_{rr}^{\text{core}} + \left(\frac{1}{2}p + \frac{1}{2}q - r\right)\varepsilon_{zz}^{\text{core}}; \quad \mathbf{u}_3' = \left(0, \frac{1}{\sqrt{2}}, -\frac{1}{\sqrt{2}}\right). \end{aligned} \quad (4.14)$$

Let's now consider the nanowire grown in <111> cubic directions. The our auxiliary unit vectors are given by

$$\begin{aligned}\mathbf{e}_1^{\text{aux}} &= \left(\frac{1}{\sqrt{2}}, -\frac{1}{\sqrt{2}}, 0\right) \\ \mathbf{e}_2^{\text{aux}} &= \left(\frac{1}{\sqrt{6}}, \frac{1}{\sqrt{6}}, -\frac{2}{\sqrt{6}}\right) \\ \mathbf{e}_3^{\text{aux}} &= \left(\frac{1}{\sqrt{3}}, \frac{1}{\sqrt{3}}, \frac{1}{\sqrt{3}}\right).\end{aligned} \tag{4.15}$$

We can still use Eq. (4.9) for the cylindrical coordinate unit vectors and find the transformation matrix as

$$\left[l_{ij}\right] = \begin{pmatrix} \frac{\cos\theta}{\sqrt{2}} + \frac{\sin\theta}{\sqrt{2}} & \frac{\cos\theta}{\sqrt{2}} - \frac{\sin\theta}{\sqrt{2}} & \frac{1}{\sqrt{3}} \\ \frac{\sin\theta}{\sqrt{6}} - \frac{\cos\theta}{\sqrt{2}} & \frac{\cos\theta}{\sqrt{6}} - \frac{\sin\theta}{\sqrt{2}} & \frac{1}{\sqrt{3}} \\ -\frac{\sin\theta}{\sqrt{6}} & -\frac{\cos\theta}{\sqrt{6}} & \frac{1}{\sqrt{3}} \end{pmatrix}. \tag{4.16}$$

We can proceed in the similar way and obtain the strain matrix as

$$\begin{pmatrix} \varepsilon_{11} & \varepsilon_{12} & \varepsilon_{13} \\ \varepsilon_{12} & \varepsilon_{22} & \varepsilon_{23} \\ \varepsilon_{13} & \varepsilon_{23} & \varepsilon_{33} \end{pmatrix} = \frac{1}{3}\begin{pmatrix} 2\varepsilon_{rr}^{\text{core}} + \varepsilon_{zz}^{\text{core}} & \varepsilon_{zz}^{\text{core}} - \varepsilon_{rr}^{\text{core}} & \varepsilon_{zz}^{\text{core}} - \varepsilon_{rr}^{\text{core}} \\ \varepsilon_{zz}^{\text{core}} - \varepsilon_{rr}^{\text{core}} & 2\varepsilon_{rr}^{\text{core}} + \varepsilon_{zz}^{\text{core}} & \varepsilon_{zz}^{\text{core}} - \varepsilon_{rr}^{\text{core}} \\ \varepsilon_{zz}^{\text{core}} - \varepsilon_{rr}^{\text{core}} & \varepsilon_{zz}^{\text{core}} - \varepsilon_{rr}^{\text{core}} & 2\varepsilon_{rr}^{\text{core}} + \varepsilon_{zz}^{\text{core}} \end{pmatrix} \tag{4.17}$$

which is also independent of the angular coordinate.

The eigenvalues and eigenvectors are obtained as

$$\lambda_1 = \frac{1}{3}\left(2\varepsilon_{rr}^{\text{core}} + \varepsilon_{zz}^{\text{core}}\right)\left(p+2q\right) + \frac{4}{3}r\left(\varepsilon_{zz}^{\text{core}} - \varepsilon_{rr}^{\text{core}}\right); \quad \mathbf{u}_1' = \left(\frac{1}{\sqrt{3}}, \frac{1}{\sqrt{3}}, \frac{1}{\sqrt{3}}\right)$$

$$\lambda_2 = \frac{1}{3}\left(2\varepsilon_{rr}^{\text{core}} + \varepsilon_{zz}^{\text{core}}\right)\left(p+2q\right) - \frac{2}{3}r\left(\varepsilon_{zz}^{\text{core}} - \varepsilon_{rr}^{\text{core}}\right); \quad \mathbf{u}_2' = \left(\frac{1}{\sqrt{2}}, -\frac{1}{\sqrt{2}}, 0\right) \quad .$$

$$\lambda_3 = \frac{1}{3}\left(2\varepsilon_{rr}^{\text{core}} + \varepsilon_{zz}^{\text{core}}\right)\left(p+2q\right) - \frac{2}{3}r\left(\varepsilon_{zz}^{\text{core}} - \varepsilon_{rr}^{\text{core}}\right); \quad \mathbf{u}_3' = \left(\frac{1}{\sqrt{6}}, \frac{1}{\sqrt{6}}, -\frac{2}{\sqrt{6}}\right)$$

(4.18)

Also, for the comparison of three modes in Eq.(4.14) and (4.18) with the experimental Raman spectra, the Raman intensity has to be computed. To compute Raman intensity we need to find the Raman tensor in cylindrical co–ordinates. If the displacements are chosen in the Cartesian direction, the Raman tensors are given in Section[3.6] as

$$R(x) = \begin{pmatrix} 0 & 0 & 0 \\ 0 & 0 & d \\ 0 & d & 0 \end{pmatrix}, \quad R(y) = \begin{pmatrix} 0 & 0 & d \\ 0 & 0 & 0 \\ d & 0 & 0 \end{pmatrix}, \quad R(y) = \begin{pmatrix} 0 & d & 0 \\ d & 0 & 0 \\ 0 & 0 & 0 \end{pmatrix}. \tag{4.19}$$

Raman tensors corresponding to eigenvectors in cylindrical co–ordinates are given by

$$R'(i) = \sum_j L_{ji} R_j \,, \tag{4.20}$$

where $L_{ji} = \mathbf{u}_j \cdot \mathbf{u}_i'$, a transformation matrix.

The Raman tensors in cylindrical co-ordinates for nanowires in **<011>** can be written as

$$R_r = d\begin{pmatrix} 0 & -\frac{\sin\theta}{\sqrt{2}} & \frac{\sin\theta}{\sqrt{2}} \\ -\frac{\sin\theta}{\sqrt{2}} & 0 & \cos\theta \\ \frac{\sin\theta}{\sqrt{2}} & \cos\theta & 0 \end{pmatrix},$$

$$R_\theta = d\begin{pmatrix} 0 & -\frac{\cos\theta}{\sqrt{2}} & \frac{\cos\theta}{\sqrt{2}} \\ -\frac{\cos\theta}{\sqrt{2}} & 0 & -\sin\theta \\ \frac{\cos\theta}{\sqrt{2}} & -\sin\theta & 0 \end{pmatrix}, R_z = d\begin{pmatrix} 0 & \frac{1}{\sqrt{2}} & \frac{1}{\sqrt{2}} \\ \frac{1}{\sqrt{2}} & 0 & 0 \\ \frac{1}{\sqrt{2}} & 0 & 0 \end{pmatrix} \quad (4.21)$$

And the Raman tensors in cylindrical co-ordinates for nanowires in <011> can be written as

$$R_r = d\begin{pmatrix} 0 & -\frac{2\sin\theta}{\sqrt{6}} & -\frac{\cos\theta}{\sqrt{2}}+\frac{\sin\theta}{\sqrt{6}} \\ -\frac{2\sin\theta}{\sqrt{6}} & 0 & \frac{\cos\theta}{\sqrt{2}}+\frac{\sin\theta}{\sqrt{2}} \\ -\frac{\cos\theta}{\sqrt{2}}+\frac{\sin\theta}{\sqrt{6}} & \frac{\cos\theta}{\sqrt{2}}+\frac{\sin\theta}{\sqrt{2}} & 0 \end{pmatrix},$$

$$R_\theta = d\begin{pmatrix} 0 & -\frac{2\cos\theta}{\sqrt{6}} & -\frac{\sin\theta}{\sqrt{2}}+\frac{\cos\theta}{\sqrt{6}} \\ -\frac{2\cos\theta}{\sqrt{6}} & 0 & \frac{\cos\theta}{\sqrt{2}}-\frac{\sin\theta}{\sqrt{2}} \\ -\frac{\sin\theta}{\sqrt{2}}+\frac{\cos\theta}{\sqrt{6}} & \frac{\cos\theta}{\sqrt{2}}-\frac{\sin\theta}{\sqrt{2}} & 0 \end{pmatrix},$$

$$R_Z = d\begin{pmatrix} 0 & \frac{1}{\sqrt{3}} & \frac{1}{\sqrt{3}} \\ \frac{1}{\sqrt{3}} & 0 & \frac{1}{\sqrt{3}} \\ \frac{1}{\sqrt{3}} & \frac{1}{\sqrt{3}} & 0 \end{pmatrix} \tag{4.22}$$

The zeroth–order approximation to the Raman tensors is considered, as it ignores the terms proportional to the strain approximation such that the Raman tensors computed in Eq.(4.21) and Eq. (4.22) represents the Raman tensors for the three different modes in the presence of the strain perturbation. In addition since in the small diameter semiconductor nanowires[79,80,81], Raman scattering is enhanced for scattering configurations in which the light's electric field is along the structure's axis, the Raman modes are then classified according to the orientation of the electric field vectors relative to the nanowire axis. The Raman intensity is given by

$$I^i \propto \left|\mathbf{E}_{\text{inc}}^T \cdot \mathbf{R}(i) \cdot \mathbf{E}_{\text{scatt}}\right|^2, \tag{4.23}$$

where E_{inc}^T and E_{scatt} are the incident and scattered electric field orientations.

4.4 Numerical Simulations of the core

We have computed the optical phonon frequencies and Raman tensors for core-shell nanowires with axes along $\langle 011 \rangle$ and $\langle 111 \rangle$ in section 4.3.

We now consider structures with Ge cores and Si shells and also structures with Si cores and Ge shells. We use the structural and elastic parameters given in Table (1). The phonon parameters are given below in Table (2.1) as

Table 4.2: Phonon parameters for Si and Ge used for the computation of strain shifts in core-shell nanowires. ω_0 is the bulk, unperturbed Raman phonon frequency, and p,q,r are the phonon deformation potentials.

	ω_0 (cm^{-1})	p/ω_0^2	q/ω_0^2	r/ω_0^2
Si	521[76]	-1.83[72]	-2.33[72]	-0.71[72]
Ge	301[76]	-1.47[72]	-1.93[72]	-1.11[72]

The value of parameter γ (refer Eq. (2.76) is slightly different for the <011> and <111> directions. For accuracy we use <011> values for <011> nanowires and <111> values for <111> nanowires, although we obtain essentially the same frequencies with either set. Similarly, we use the Voigt average of the Si Poisson ratio for Si-core nanowires, and we use the corresponding Ge average for Ge–cores. Figs. (4.2) – (4.5) show the results of the numerical simulations. Critical discussions on Poisson's ratio are given in chapter 5. We begin by computing the core strain tensor components as a function of the *c/a* ratio using Eqs. (4.1) – (4.3), and then we calculate the phonon frequencies using Eqs. (4.14) or (4.18). We compute the Raman intensities using the Raman tensors obtained in Eqs. (4.21) or (4.22). Raman modes are computed for both light polarizations parallel to the nanowire axis, with one polarization

parallel to the nanowire axis, and another with no polarization parallel to the nanowire axis. The polarizations are indicated in Figs. 4.2 – 4.5, where the thicker line corresponds to the frequency shift observed for both polarizations parallel to the nanowire axis, which presumably corresponds to the dominant Raman mode in small diameter nanowires. The figures are given below:

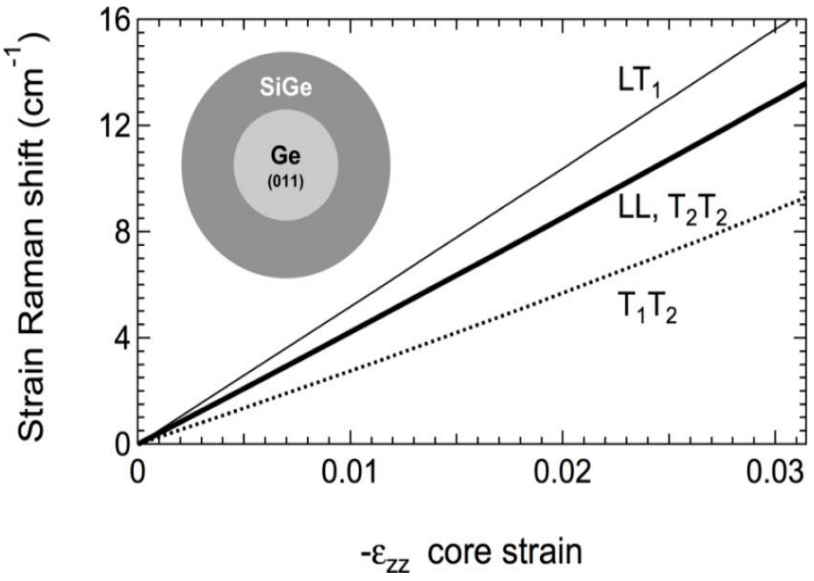

Fig. 4.2 Computed core Raman phonon frequency shifts in a fully-strained Ge-Si core-shell nanowire with axis along the <011> crystallographic direction. The figure can also be used to obtain the shifts in a Ge-$Si_{1-x}Ge_x$ core-shell structure by simply computing from Eq.(4.3). The labels in the lines correspond to the incident and scattered light polarization directions for which the corresponding modes are observed. L = <011>, T1 = <100>, T2 == $< 01\bar{1} >$.

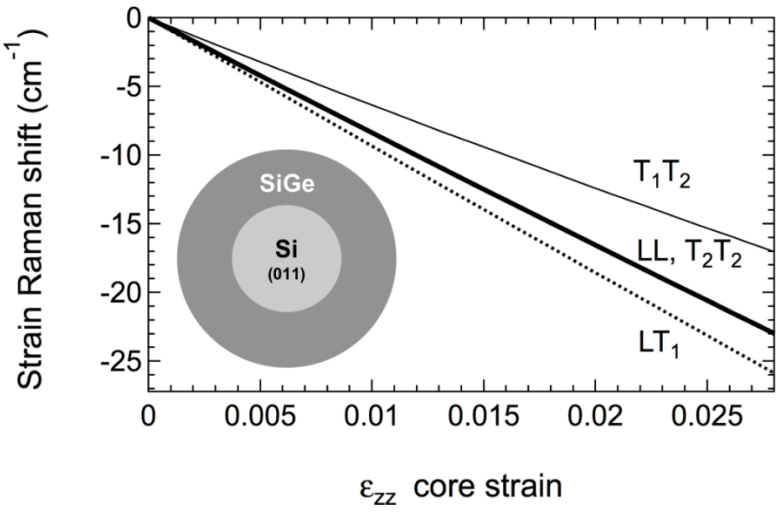

Fig. 4.3 Computed core Raman phonon frequency shifts in a fully-strained Si-Ge core-shell nanowire with axis along the <011> crystallographic direction. The figure can also be used to obtain the shifts in a Si-$Si_{1-x}Ge_x$ core-shell structure by computing $\varepsilon_{zz}^{\text{core}}$ from Eq.(4.3). The labels in the lines correspond to the incident and scattered light polarization directions for which the corresponding modes are observed. L = <011>, T_1 = <100>, $T_2 = < 01\bar{1} >$.

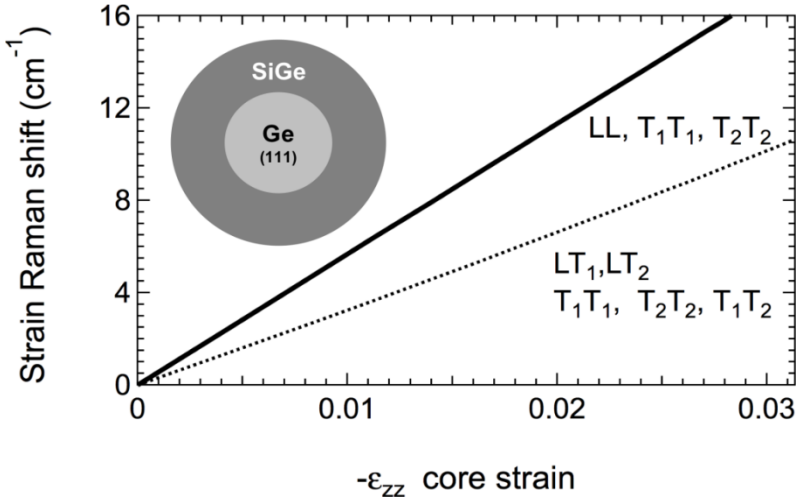

Fig. 4.4 Computed core Raman phonon frequency shifts in a fully-strained Ge-Si core-shell nanowire with axis along the <111> crystallographic direction. The figure can also be used to obtain the shifts in a Ge-$Si_{1-x}Ge_x$ core-shell structure by simply re-computing $\varepsilon_{zz}^{\text{core}}$ from Eq.(4.3). The labels in the lines correspond to the incident and scattered light polarization directions for which the corresponding modes are observed. L = <111>, $T_1 = < 1\bar{1}0 >$, $T_2 = < 11\bar{2} >$.

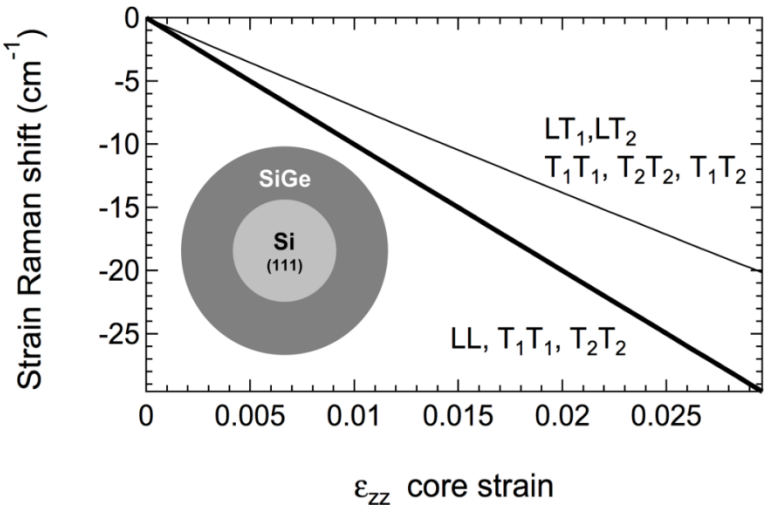

Fig. 4.5 Computed core Raman phonon frequency shifts in a fully-strained Si-Ge core-shell nanowire with axis along the <111> crystallographic direction. The figure can also be used to obtain the shifts in a Si-$Si_{1-x}Ge_x$ core-shell structure by simply computing $\varepsilon_{zz}^{\text{core}}$ from Eq.(4.3). The labels in the lines correspond to the incident and scattered light polarization directions for which the corresponding modes are observed. L = <111>, T_1 = $<1\bar{1}0>$, T_2 = $<11\bar{2}>$.

The results in Figs. 4.2 – 4.5 are presented as a function of $\varepsilon_{zz}^{\text{core}}$. This approach makes it simple to use the calculations for Si–Ge or Ge–Si core–shell nanowires to obtain the phonon frequencies in systems in which the shell consists of a $Si_{1-x}Ge_x$ alloy. Now we only need to compute the appropriate value of $\varepsilon_{zz}^{\text{core}}$ using Eq.(4.3), and find the core frequencies from Figs 4.2–4.5. Also, since the strain tensor is exactly proportional to $\varepsilon_{zz}^{\text{core}}$ in Eqs. (2.52)– (2.57), it justifies the approach, but this does not apply to the more accurate expressions in Eqs. (4.1)–(4.3), in which the difference between core and shell Young moduli is taken into account. However, numerical simulations show that the core frequencies obtained for the case of alloy shells using the full procedure

from Eqs. (4.1)–(4.3), through Eqs. (4.14) or (4.18), differ from the simple approach just described by less than 0.1 cm^{-1}. This difference can be neglected as this error is considerably smaller than other sources of error. The data in Figs 4.2–4.5 can be implemented to fit the strain dependence of the mode which is Raman–active for both polarizations parallel to nanowire axis with a linear function. The results are (in cm^{-1}):

$$\begin{aligned}
&\Delta\omega_{\mathrm{LL}} = -431\varepsilon_{zz}^{\mathrm{core}} \quad \langle 011 \rangle \text{ nanowire, Ge core} \\
&\Delta\omega_{\mathrm{LL}} = -824\varepsilon_{zz}^{\mathrm{core}} \quad \langle 011 \rangle \text{ nanowire, Si core} \\
&\Delta\omega_{\mathrm{LL}} = -565\varepsilon_{zz}^{\mathrm{core}} \quad \langle 111 \rangle \text{ nanowire, Ge core} \\
&\Delta\omega_{LL} = -999\varepsilon_{zz}^{\mathrm{core}} \quad \langle 111 \rangle \text{ nanowire, Si core}
\end{aligned} \qquad (4.24)$$

Hence we have computed the strain–induced Raman frequency shifts in core–shell nanowires based on the Si/Ge system. Errors in the predicted shifts arise mainly from the use of isotropic averages for the Poisson ratios of Si and Ge. These errors are not likely to exceed 20% of the total shifts. A more detailed and complete numerical analysis is shown in the Chapter 5.

CHAPTER 5

VALIDATION OF THE ANALYTICAL STRAIN MODEL FOR CORE-SHELL NANOWIRE

5.1 Introduction

The approximations required to obtain analytical solutions for the strain in core-shell nanowires raise doubts about the accuracy of the Raman shift predictions based on this model. Even though we have incorporated an important improvement relative to the original work of Liang in chapter 4 (and corrected an error in their calculation in chapter 2) by accounting for the different Young moduli of Si and Ge, the fact remains that the cylindrical geometry is a very crude representation of the experimental nanowire geometries, and that we are neglecting the very large anisotropy of the Poisson ratio in Si and Ge by using Voigt averages. However, these simplifications will not affect all strain components equally. Let us start with the axial components of the strain. According to Eq. (2.48) the misfit strain $\varepsilon_{\text{misfit}}$ is distributed between the core and the shell in such a way that the magnitudes of the ε_{zz} components are inversely proportional to the corresponding cross-sectional areas. This originates from the boundary condition that the net force on any core cross-section must be equal and opposite to the net force on the corresponding shell cross section, so that the overall net force on any nanowire cross section vanishes

under equilibrium conditions, as discussed in Chapter 2. The forces on the core and shell cross sections are proportional to the corresponding strain, cross-sectional area, and Young modulus. Since Young moduli are taken to be the same for the core and shell in Eqs.(2.52)- (2.57), the final result is that the core and shell strains are simply inversely proportional to their corresponding cross-sectional areas. When the difference between Young moduli is accounted for, as in Eq. (4.3) and (4.6), the final values for the strain are inversely proportional to the areas multiplied by their respective Young moduli. This zero-force boundary condition would still be valid in the case of anisotropic materials, and the core and shell strains would still be proportional to the corresponding areas. Therefore, we expect Eqs. (4.3) and (4.6) to be reasonably accurate even for anisotropic core-shell nanowires of arbitrary shapes, as long as the radii a and c are chosen in such a way that core/shell area ratio in the cylindrical model is the same as the core/shell area ratio in the real nanowire. Moreover, since Eqs.(4.3) and (4.6) depend on the *ratio* γ of Young moduli, the result should be largely independent of the nanowire growth direction. We thus expect the ε_{zz} components of the strain computed with our analytical model to be a faithful representation of the ε_{zz} strain components in real core-shell nanowires. On the other hand, the in-plane strain components ε_{rr} and $\varepsilon_{\theta\theta}$ depend explicitly on the Poisson ratio, and therefore they are

less reliable because of the anisotropy of this parameter. However, we notice from Eqs.(2.52) and (2.53) that $\varepsilon_{rr}^{\text{core}}$ and $\varepsilon_{\theta\theta}^{\text{core}}$ are proportional to $\frac{1}{2}(1-3\nu)/(1-\nu)$, which vanishes for ν = 1/3.[47] Since the actual value of the Poisson ratio is not too far from this value, this means that $\varepsilon_{rr}^{\text{core}}$ and $\varepsilon_{\theta\theta}^{\text{core}}$ will be considerably smaller than $\varepsilon_{zz}^{\text{core}}$. For example, using the above Voigt averages for ν, the in-plane strain components are about four times smaller than $\varepsilon_{zz}^{\text{core}}$. This means that the larger expected error in the in-plane strain components, arising from Poisson ratio averaging, will be mitigated by their smaller magnitude relative to the more accurate axial component. However, in view of these approximations we can question not only the accuracy of the predicted Raman peak shifts, but also the main qualitative features of the calculated strain distributions, including the prediction of uniform strain in the core section of the nanowire, which plays an important role for strain characterization. To address these critical issues we present in this chapter a comparative numerical-analytical analysis of the Raman frequencies in Ge-Si core-shell nanowires with axis parallel to the <011> directions, as obtained for growth on (001) surfaces. First, the strain distribution in the nanowires is obtained using a finite-element code that uses realistic nanowire geometry and a cubic, anisotropic elasticity model for Si and Ge. This is done using the

commercial package ABAQUS. Then the Raman spectrum is calculated at each point using the local strain tensor, and the final spectrum is obtained by integrating over the volume of the nanowire. We compare the strain predicted by this numerical method with the strain obtained from our analytical model, and we compute the Raman spectrum corresponding to the numerical strain model by averaging over the nanowire cross section.

5.2 Numerical Simulations of Strain

The numerical calculations of strain were conducted using the commercial package ABAQUS. Using this program it is possible to reproduce the exact nanowire geometry corresponding to the experimental situation. The samples that we studied experimentally are nanowires with their axis along the, <011> direction, with a cross section as shown in Fig 5.1. We considered the case of a Ge core and Si Shell, as studied experimentally.

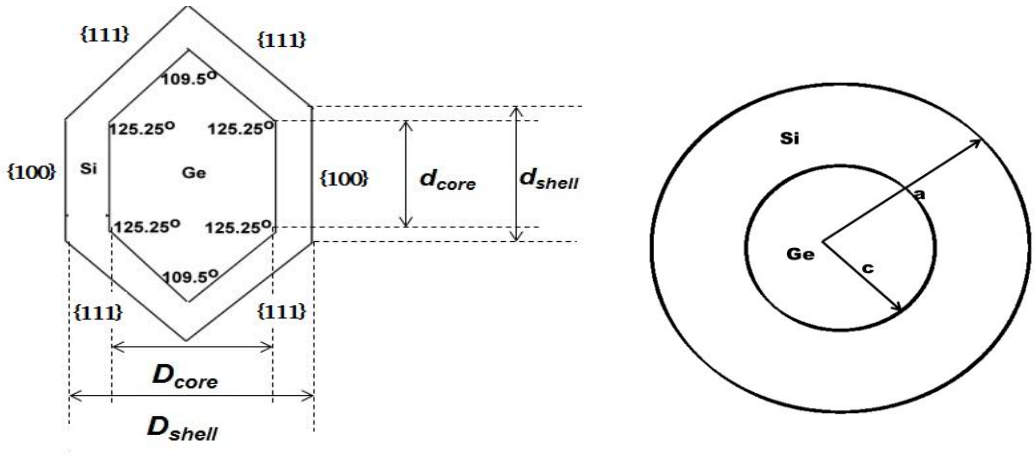

(a) (b)

Fig(5.1): Schematic representation of the Ge-Si core-shell nanowires cross-section used for the (a) numerical and (b) analytical calculations of strain and Raman spectra.

We define D_{core} (D_{shell}) as the distance between opposite (100) faces in Fig. 5.1(a), and d_{core} (d_{shell}) the length of these (011) faces measured along the <01-1> direction. The geometry of the nanowires is chosen so that $d_{core}/D_{core} = d_{shell}/D_{shell} = 0.612$. This gives a fairly good approximation of the observed nanowire geometries.

5.2.1 Analysis of anisotropic analytical model

For a comparison of the analytical and numerical results we need to find the best choice for the *c* and *a* radii in Fig. (5.1b). As suggested by the introductory discussion, the core radius should be selected in such a way that the core cross-sectional area in the cylindrical nanowire is equal to the core area in the realistic nanowire. Similarly, the shell

outer radius in the cylindrical geometry is chosen so that the ratio of shell/core areas is the same as in the realistic nanowire. From Fig. (5.1), it is trivial to show that the core area is given by

$$A_{\text{core}} = D_{\text{core}} d_{\text{core}} + \tfrac{1}{2} D_{\text{core}}^2 \tan\left(\alpha - \pi/2\right),$$

where α = 125.25°, so that a circle with the same area would have a ratio of

$$c = \sqrt{\frac{D_{\text{core}} d_{\text{core}} + \tfrac{1}{2} D_{\text{core}}^2 \tan\left(\alpha - \pi/2\right)}{\pi}} = D_{\text{core}} \sqrt{\frac{d_{\text{core}}/D_{\text{core}} + \tfrac{1}{2}\tan\left(\alpha - \pi/2\right)}{\pi}}. \tag{5.1}$$

Similarly, for the shell area we obtain

$$A_{\text{shell}} = D_{\text{shell}} d_{\text{shell}} + \tfrac{1}{2} D_{\text{shell}}^2 \tan\left(\alpha - \pi/2\right).$$

so that the equivalent circular shell should have a ratio given by

$$a = \sqrt{\frac{D_{\text{shell}} d_{\text{shell}} + \tfrac{1}{2} D_{\text{shell}}^2 \tan\left(\alpha - \pi/2\right)}{\pi}} = D_{\text{shell}} \sqrt{\frac{d_{\text{shell}}/D_{\text{shell}} + \tfrac{1}{2}\tan\left(\alpha - \pi/2\right)}{\pi}}. \tag{5.2}$$

Since the ratio $d_{\text{core}}/D_{\text{core}}$ was taken to be the same as $d_{\text{shell}}/D_{\text{shell}}$ in the ABAQUS simulations, the geometry is fully determined by giving the two diameters D_{core} and D_{shell} or D_{core} and the shell thickness $t_{\text{shell}} = D_{\text{shell}} - D_{\text{core}}$.

The analytical solutions for the strain were obtained in chapter 4[47] in Eqs. (4.1) – (4.6) by assuming a cylindrical core-shell structure and isotropic elastic constants characterized by Young moduli E^{core},

E^{shell}, and a common Poisson ratio $v_{core} = v_{shell} = v$. Also all off-diagonal components of the core and shell strain tensors are zero from Eq.(2.27). For the Poisson ratio we use the Voigt average[77,82]

$$\nu = \frac{c_{11} + 4c_{12} - 2c_{44}}{4c_{11} + 6c_{12} + 2c_{44}}, \tag{5.3}$$

where the c_{ij}'s are the elastic constants in the standard contracted index notation. Since this expression is a *ratio* of such constants, its value is almost identical in Si and Ge, justifying the use of a common Poisson ratio for both materials, which greatly simplifies the math. Instead of averaging the two very similar values we simply use Eq. (5.3) with elastic constants from Ge for core calculations, and with Si elastic constants for shell calculations. For the Young moduli we don't use Voigt averages but the value of the modulus for the crystalline direction corresponding to the nanowire main axis. For the case of nanowires with a <011> axes, as discussed here, the Young modulus is easily obtained from the stress-strain relations as[77,82]

$$E_{110} = \frac{4\left(c_{11}^2 + c_{11}c_{12} - 2c_{12}^2\right)c_{44}}{2c_{11}c_{44} + c_{11}^2 + c_{11}c_{12} - 2c_{12}^2} \tag{5.4}$$

In the same spirit, it is possible to compute a better effective Poisson ratio for specific nanowires by averaging over rotations around the nanowire axis rather than over all possible rotations in three-dimensions, as done for the Voigt average. However, the improvement

is expected to be minor because the core-shell nanowire strain does not depend strongly on the Poisson ratio.[47] Table 5.1 shows the values of the elastic constants used for the strain calculations in this paper as well as all other parameters used to compute the Raman spectra.

Table 5.1: Structural, elastic, and phonon anharmonic parameters used for the computation of the strain in Ge-Si core-shell nanowires.

	Lattice constant(Å)	c_{11} (GPa)	c_{12} (GPa)	c_{44} (GPa)	ω_0 (cm^{-1})	p/ω_0^2	q/ω_0^2	r/ω_0^2
Si	5.43086[83]	166[84]	63.9[84]	79.5[84]	521[76]	1.716[85]	-2.136[85]	-0.66[85]
Ge	5.6568[83]	124[84]	41.3[84]	68.3[84]	301[76]	1.618[85]	2.075[85]	-0.91[85]

The strain graphs were plotted and analyzed using IGOR Pro 6.1 software.

5.2.2 Numerical Simulations of ABAQUS model

The numerical calculations of strain were conducted using the commercial package ABAQUS, which applies a finite-element method to the continuum elasticity problem. The geometry of the simulated core-shell nanowires was chosen to be similar to the experimentally observed geometries for <011> oriented nanowires grown on Si (111) surfaces.[87,88,86] The nanowires have a hexagonal cross-section consisting of {100} and {111} facets (Fig. 1). These are lower-energy surfaces than the (112} facets present in <111>-oriented nanowires, minimizing surface roughening effects.[86] Thus <011>-oriented

nanowires are ideal for strain studies. We take $d_{core}/D_{core} = d_{shell}/D_{shell} =$ 0.612, which gives a fairly good approximation of the observed nanowire geometries.To simulate the lattice mismatch strain, the Si shell material is assigned an artificially large thermal expansion coefficient, so that a temperature change of -1°C leads to the experimental mismatch between Si and Ge at room temperature. The relevant information is taken from the central cross-section of the wire, for which end effects can be neglected. Since cylindrical coordinates are the obvious choice for cylindrical nanowires, and our analytical solutions in Eqs.(4.1)–(4.6) are expressed in cylindrical coordinates, we also expressed the numerical results obtained with the ABAQUS code in cylindrical coordinates, using the transformation matrix given in Eq.(4.16). This should facilitate the comparison between numerical and analytical strain calculations. The calculated strains are graphed using IGOR Pro 6.1 software.

5.2.3 Comparison of numerical and analytical Strains

We have performed calculations for 9 core-shell nanowires with dimensions similar to those observed experimentally.[87,88] The samples studied for numerical and analytical simulations are given in Table(5.2) below:

Table 5.2 Samples used for numerical and analytical simulations to study the strain distributions and Raman frequencies.

Sample	Dcore (nm)	t_{shell} (nm)
hscs28_090319	11	3.4
hscs27_090318	11	5
hscs26_090217	11	9
hscs29_090319	9	6.5
hscs45_090618	32	4.9
hscs40_090615	41	6.1
hscs47_090622	44	3.7
hscs46_090619	45	9.1
hscs43_090617	53	7.2

In fig. (5.2) we show a comparison of the diagonal components of the strain obtained from the analytical and numerical approaches for a nanowire with a Ge core with diameter D_{core} = 11 nm and a Si shell with thickness t_{shell} = 5 nm. We only show strain and Raman results for this nanowire, but all quoted numerical deviations between the analytical and numerical models of the strain correspond to averages for all nanowires. The numerical deviations and the diagonal and off-diagonal components of strain components of nine nanowires are shown in APPENDIX I and APPENDIX II respectively.

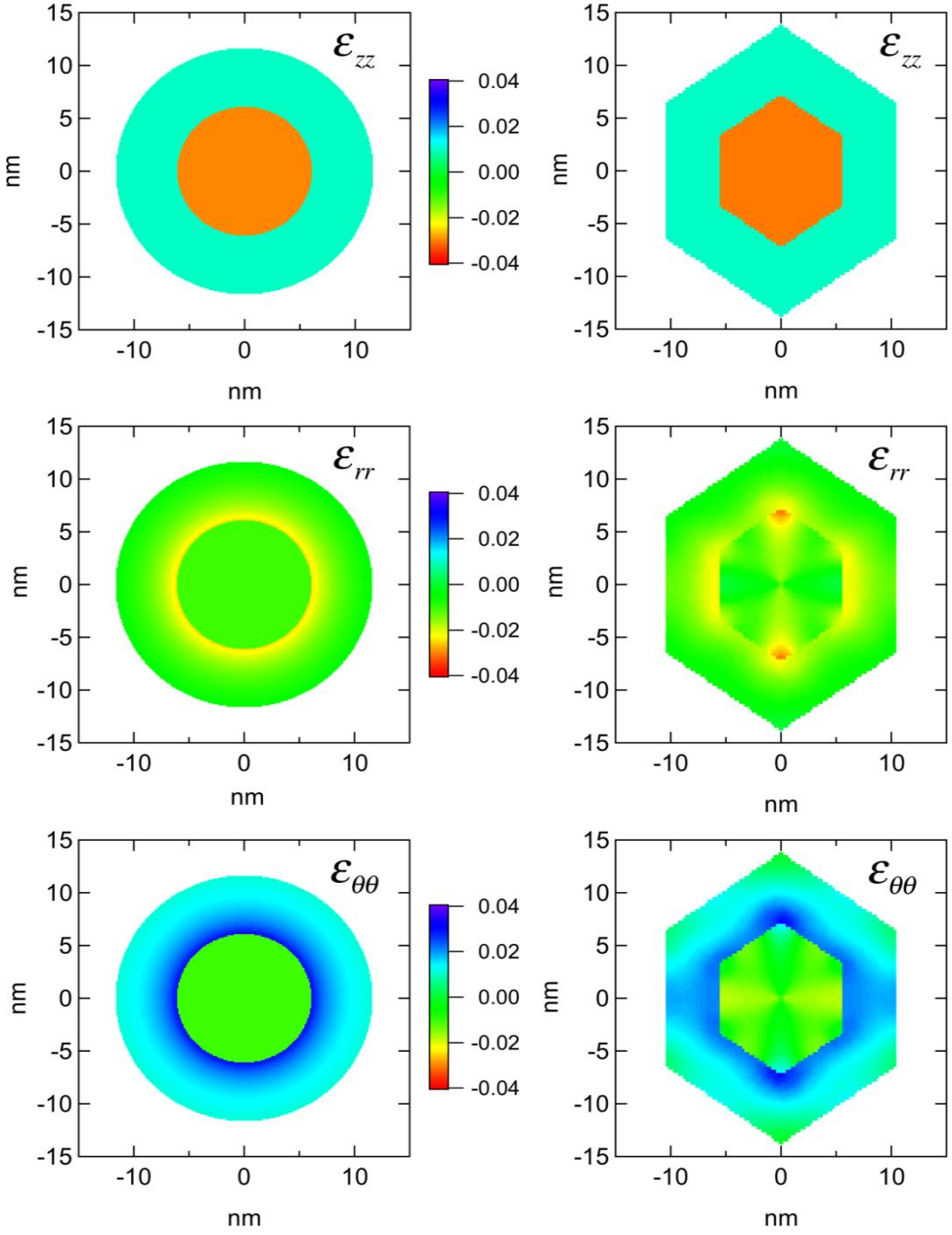

Figure 5.2 Comparison of the diagonal components of the strain tensor for a <011> Ge-Si core-shell nanowire with D_{core} = 11 nm and t_{shell} = 5 nm obtained with the analytical expressions in Eq. (4.1)-(4.6) (left) and the numerical finite-element package ABAQUS (right).

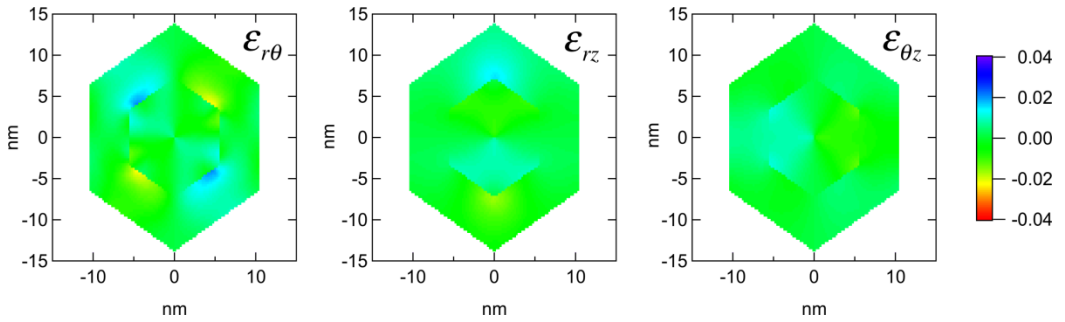

Figure 5.3 Off-diagonal components of the strain tensor for a <011> Ge-Si core-shell nanowire with D_{core} = 11 nm and t_{shell} = 5 nm obtained with the numerical finite-element package ABAQUS (right). The corresponding components in the analytical model of Eqs. (4.1)-(4.6) are exactly zero.

We observe a nearly perfect agreement between the ε_{zz} components calculated with the two methods. The uniformity (independence of r and θ) predicted by the analytical model in Eq. (4.3) is corroborated by the numerical study, and the strain values are very similar: for the analytical model we find $\varepsilon_{zz}^{\text{core}}$ = -0.0306 and $\varepsilon_{zz}^{\text{shell}}$=0.0094, whereas the numerical results are $\varepsilon_{zz}^{\text{core}}$ = -0.0314 and $\varepsilon_{zz}^{\text{shell}}$ = 0.0091. This confirms the argument in chapter 4[47] that the analytical model should yield very accurate values of the ε_{zz} component provided that the cylindrical cross-sectional areas are selected to match the cross-sectional areas of the real nanowire. The analytical model also implies uniform values of $\varepsilon_{rr}^{\text{core}}$ and $\varepsilon_{\theta\theta}^{\text{core}}$, and this result is clearly not perfectly reproduced in the numerical calculation. However, the largest discrepancies are limited to the corners of the hexagonal cross-section. At the center of the nanowire the agreement is very reasonable: whereas the numerical model gives $\varepsilon_{rr}^{\text{core}}$ = -0.011 and $\varepsilon_{\theta\theta}^{\text{core}}$ = -0.008, the analytical calculations

yields $\varepsilon_{rr}^{\text{core}} = \varepsilon_{\theta\theta}^{\text{core}} = -0.010$. These values are clearly smaller than those for $\varepsilon_{zz}^{\text{core}}$ component, and therefore they are expected to have a smaller impact on the Raman frequencies. Finally, the off-diagonal core strain components, shown in Fig. (5.3), are close to zero, as in the analytical model, when averaged over the entire nanowire cross section.

One might expect the shell to show the largest deviations between the numerical and analytical calculations, because realistic shells are quite thin and therefore the cylindrical geometry of the analytical model may be a crude approximation. Nevertheless, all qualitative features of the analytical results are reproduced in the numerical calculation, including the ring of negative values of $\varepsilon_{rr}^{\text{shell}}$ near the core interface and the corresponding ring of positive $\varepsilon_{\theta\theta}^{\text{shell}}$ values. The quantitative agreement, as expected, is not excellent. For example, right at the interface $\varepsilon_{\theta\theta}^{\text{shell}} = 0.03$ in the analytical calculation, but the numerical results are closer to $\varepsilon_{\theta\theta}^{\text{shell}} = 0.02$.

5.3 Raman Calculations and Discussions

Raman spectrum of the core and shell part of a core-shell nanowire was computed for core-shell nanowires with axes along $\langle 011 \rangle$ direction using the strain computed with the finite element code, ABAQUS and analytical model. Ge cores and Si shells systems were considered.

5.3.1 Numerical Simulations of Raman Spectra

The Raman spectrum corresponding to the strained nanowires is obtained as discussed in chapter 4[47]. We start with the triply-degenerate zone-center optical phonons in bulk diamond-structure semiconductors, with frequency ω_0 and eigenvectors that can be chosen as $\mathbf{u}_1 = (1,0,0)$, $\mathbf{u}_2 = (0,1,0)$, and $\mathbf{u}_3 = (0,0,1)$ in Cartesian coordinates. The effect of strain on these modes is computed using degenerate perturbation theory by solving the secular problem[72,47]

$$\begin{vmatrix} p\varepsilon_{11} + q(\varepsilon_{22} + \varepsilon_{33}) - \lambda & 2r\varepsilon_{12} & 2r\varepsilon_{13} \\ 2r\varepsilon_{12} & p\varepsilon_{22} + q(\varepsilon_{11} + \varepsilon_{33}) - \lambda & 2r\varepsilon_{23} \\ 2r\varepsilon_{13} & 2r\varepsilon_{23} & p\varepsilon_{33} + q(\varepsilon_{11} + \varepsilon_{22}) - \lambda \end{vmatrix} = 0, \tag{5.5}$$

where the strain is in cartesian coordinates and we have defined $\lambda = \omega^2 - \omega_0^2$. Here $p = K_{1111}$, $q = K_{1122}$, and $r = K_{2323}$ are the non-zero components of the phonon deformation potential tensor.[72] This $K_{\alpha\beta\gamma\delta}$ tensor has the exactly the same symmetry as the elastic constants tensor $c_{\alpha\beta\gamma\delta}$ but is even more anisotropic, creating a serious dilemma. If one combines in the same calculation the full cubic $K_{\alpha\beta\gamma\delta}$ deformation potential tensor with the strains from Eqs.(4.1)-(4.6), based on isotropic elastic constants, there is a risk of obtaining unphysical results due to the inconsistent treatment of the elastic and phonon

tensors. On the other hand, if one averages the $K_{\alpha\beta\gamma\delta}$ tensor to obtain an effective isotropic phonon deformation potential tensor, there is a risk of losing accuracy. In chapter 4[47] we choose the first option more or less arbitrarily, but here we can explore its validity by comparing Raman calculations with and without averaging of the deformation potential and elastic constants. For this we define average phonon deformation potentials $\bar{p}, \bar{q}$ and $\bar{r}$ using exactly the same approach that gives average elastic constants. Starting from the Voigt averaging procedure,[77,82] it is straightforward to show that the average and cubic deformation potential tensor components are related by

$$\begin{aligned} \bar{p} &= \tfrac{1}{5}\left(3p + 2q + 4r\right) \\ \bar{q} &= \tfrac{1}{5}\left(p + 4q - 2r\right) \\ \bar{r} &= \tfrac{1}{5}\left(p - q + 3r\right), \end{aligned} \tag{5.6}$$

which satisfies the isotropic condition $2\bar{r}/\left(\bar{p}-\bar{q}\right)=1$. Since, as mentioned above, the phonon deformation potential tensor is very anisotropic, the average $\bar{p}$, $\bar{q}$, and $\bar{r}$ are very different from the cubic *p*, *q*, and *r*. However, the Voigt average preserves the Grüneisen parameter $\gamma_h = -\tfrac{1}{6}\left(p+2q\right)/\omega_0^2 = -\tfrac{1}{6}\left(\bar{p}+2\bar{q}\right)/\omega_0^2$ that gives the phonon frequency shifts under hydrostatic strain.

The phonon problem in Eq. (5.5) is solved at each point of the nanowire, using the local values of the strain. The Raman tensors[47] $\mathbf{R}'$

(i) corresponding to each of the i =1,2,3 modes obtained from Eq. (5.6) are written as

$$\mathbf{R}'(i) = \sum_j L_{ji}\mathbf{R}(j), \tag{5.7}$$

where the unprimed Raman tensors correspond to the unperturbed Raman tensors in bulk diamond-structure materials, and $L_{ji} = \mathbf{u}_j \cdot \mathbf{u}'_i$, where the $\{\mathbf{u}'_i\}$ are the eigenvectors from Eq. (5.5). For the modes with the $\mathbf{u}_i$ unperturbed eigenvectors given above, the symmetry of the diamond structure dictates $R_{\alpha\beta}(i) = d(1-\delta_{\alpha\beta})(1-\delta_{i\alpha})(1-\delta_{i\beta})$, where α,β = 1,2,3 correspond to the x,y,z cartesian coordinates and d is a constant. Using the Raman tensors in Eq. (5.7), the Raman intensities are given by

$$I^i_{\text{inc,scatt}} \propto \left|\mathbf{E}^T_{\text{inc}} \cdot \mathbf{R}'(i) \cdot \mathbf{E}_{\text{scatt}}\right|^2, \tag{5.8}$$

where the $\mathbf{E}$'s are the electric field vectors of the incident and scattered light. These intensities are computed at each nanowire point and then integrated (added) over the entire nanowire and over the three modes. We will consider light polarized parallel or perpendicular to the nanowire axis, using the notation L = [011], T_1 = [100], and T_2 = [01$\bar{1}$]. It is important to emphasize that the electric fields appearing in Eq. (5.8) are local fields at the nanowire, which are not necessarily related to the external electric field of the incident electromagnetic field by a

single multiplicative constant, as is the case with macroscopic samples.[89] There is in fact substantial experimental evidence that electromagnetic waves polarized parallel to the nanowire axis set up much larger local fields than waves with transverse polarization relative to the nanowire.[79,90,91] This implies that the Raman spectrum should be dominated by the *LL* scattering configuration, regardless of nanowire orientation. Therefore, we pay particular attention to Raman scattering in this configuration.

5.3.2 Core Raman Spectra

The Raman spectra of the core of nanowire with Dcore = 11 nm and t_{shell} = 5.0 nm obtained from ABAQUS and analytical in parallel configuration is shown in Fig. (5.4). Raman spectra of core in LL configuration for all the nine samples studied are shown in APPENDIX III.

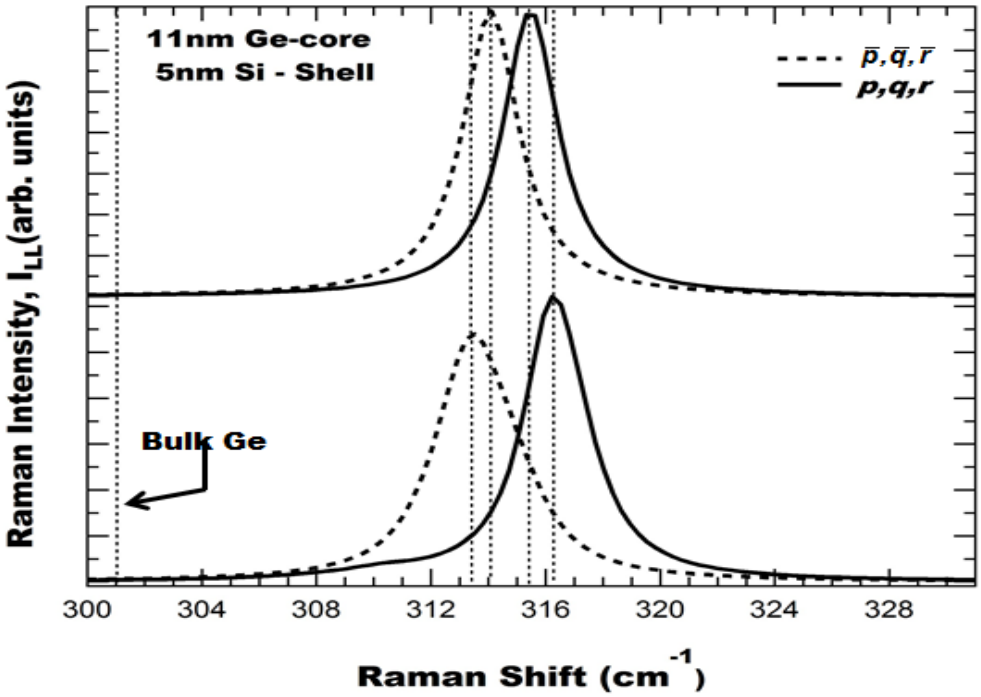

Figure 5.4 Calculated Raman spectra of the core region for a <011> Ge-Si core-shell nanowire with D_{core} = 11 nm and t_{shell} = 5.0 nm. Incident and scattered light polarizations are parallel to the nanowire axis. The top curves correspond to the analytical strain model with cylindrical geometry. The bottom curves correspond to the numerical strain calculation with realistic geometry. Solid lines were calculated using cubic symmetry *p,q, r* phonon deformation potential tensor components from Table 5.1. Dotted lines were calculated using the Voigt averaged tensor components from Eq.(5.6). All spectra are normalized to the same area. The vertical scale is the same in both panels. Darker regions give stronger contributions.

Fig.(5.4) shows the calculated Raman intensity I_{LL} for LL polarization. The peaks have been broadened using the experimentally determined Lorentzian width in bulk Ge.[92] In the case of the analytical strain model, corresponding to the top panel in Fig.(5.4), the strain tensor is perfectly uniform within the core and only one of the three optical modes is Raman-allowed for this polarization configuration, so that the peak lineshape is identical to that of bulk Ge. The only difference with the Raman spectrum of bulk Ge is that the compressive strain in the

Ge core upshifts the mode frequency. The Raman peak in the lower panel, corresponding to the numerical calculation, also has a very similar lineshape, indicating that a single phonon mode is dominant, even though the strain is no longer exactly uniform over the core. The most significant qualitative difference between the analytical and numerical modes is the appearance of a weak shoulder at the bottom of the peaks in Figs.(5.4).The Fig. (5.5) shows the origin of the shoulder near 310 cm^{-1} for the core region for a <011> Ge-Si core-shell nanowire with D_{core} = 11 nm and t_{shell} = 5.0 nm below.

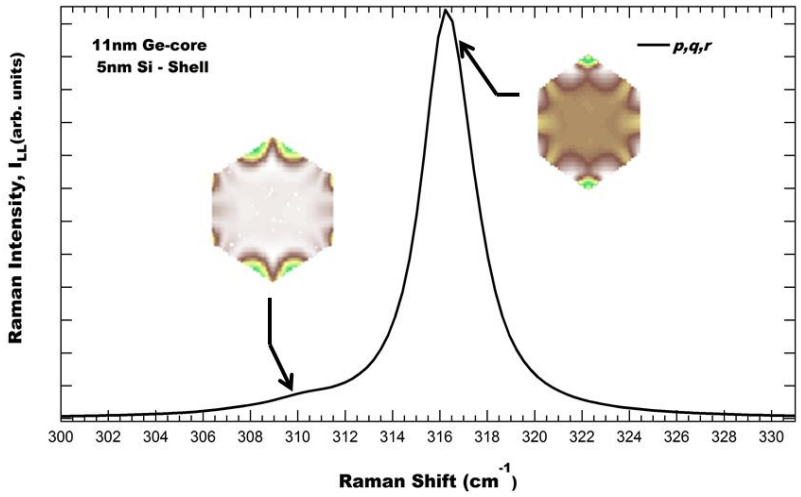

Figure 5.5 Calculated Raman spectra of the core region for a <011> Ge-Si core-shell nanowire with D_{core} = 11 nm and t_{shell} = 5.0 nm. Incident and scattered light polarizations are parallel to the nanowire axis. The curve correspond to the numerical strain calculation with realistic geometry. Solid lines were calculated using cubic symmetry *p,q, r* phonon deformation potential tensor components from Table 5.1. The vertical scale is the same in both panels. The inset diagrams in the bottom panel indicate the core regions from which the different spectral components originate.

In Fig.(5.5) the insets show the spatial localization of the modes. As might be expected, the shoulder originates from regions near the core-

shell interface where the details of the geometry are obviously not captured by the cylindrical approximation. To see more clearly the effect of strain on the Raman-active modes, we recalculate Fig.(5.5) with an unrealistically small Lorentzian width, as shown in Fig(5.6). We see a small high energy contribution in the numerical model, which was not apparent in Fig. 5.5. We speculate that this contribution arises from the small pockets of higher compressive strain seen in Fig. 5.2.

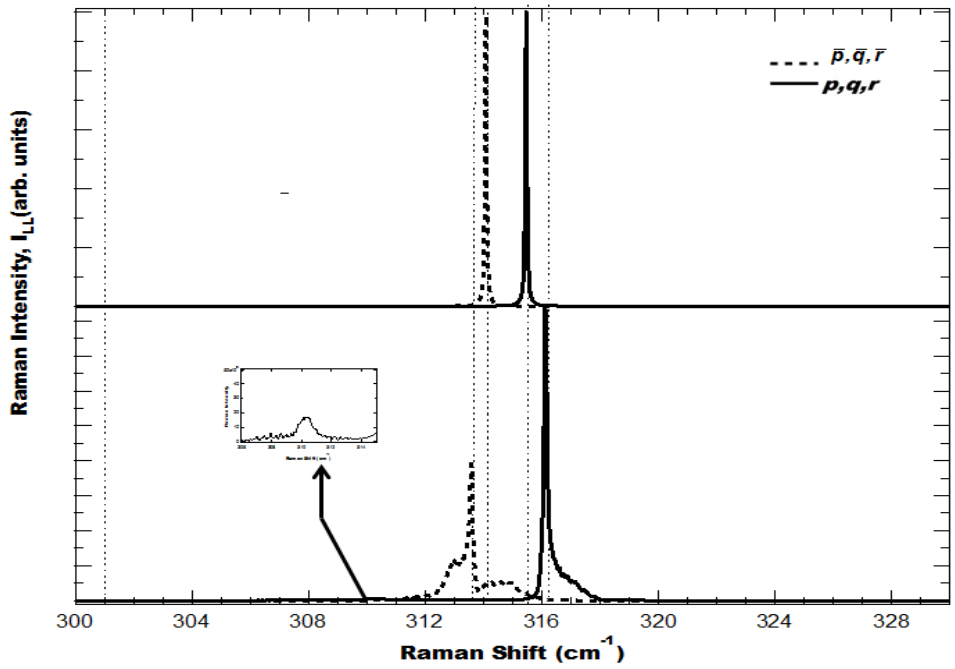

Figure 5.6 Calculated Raman spectra of the core region for a <011> Ge-Si core-shell nanowire with D_{core} = 11 nm and t_{shell} = 5.0 nm with minimal Lorentzian broadening. Incident and scattered light polarizations are parallel to the nanowire axis. The top curves correspond to the analytical strain model with cylindrical geometry. The bottom curves correspond to the numerical strain calculation with realistic geometry. Solid lines were calculated using cubic symmetry *p,q, r* phonon deformation potential tensor components from Table 5.1. Dotted lines were calculated using the Voigt averaged tensor components from Eq.(5.6). All spectra are normalized to the same area. The vertical scale is the same in both panels.

Fig.(5.7) shows the predicted Raman spectrum for the other three polarizations that give non-zero scattering intensities. The Raman spectra of all the samples with LT_1, T_1T_2 and T_2T_2 polarizations are shown in APPENDIX IV.

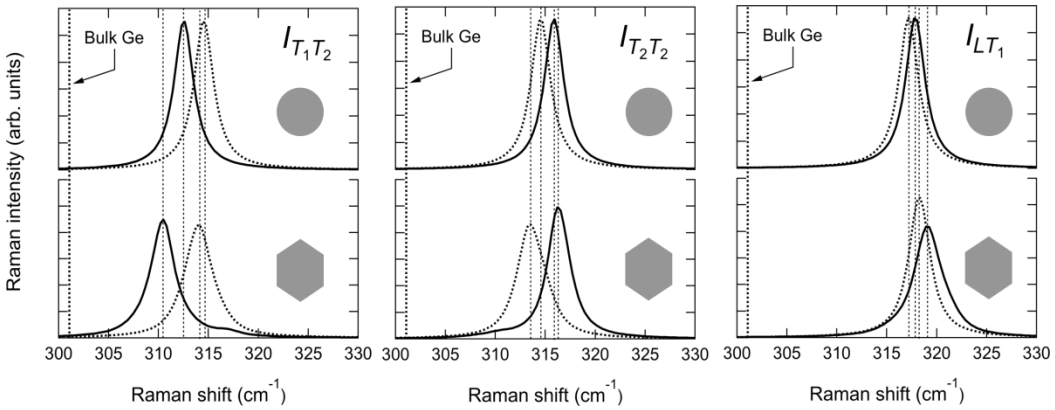

Figure 5.7 Calculated Raman spectra of the core region of a <011> Ge-Si core-shell nanowire with D_{core} = 11 nm and t_{shell} = 5 nm. Incident and scattered light polarizations are indicated in the three different panels. The convention is L = <011>, T_1 = <100>, and $T_2 = <01\bar{1}>$. The top curves correspond to the analytical strain model with cylindrical geometry. The bottom curves correspond to the numerical strain calculation with realistic geometry. Solid lines were calculated using cubic symmetry *p,q, r* phonon deformation potential tensor components from Table 5.1. Dotted lines were calculated using the Voigt averaged tensor components from Eq. (5.6). All spectra are normalized to the same area. The vertical scale is the same in all panels.

The calculation of Raman spectra with two different sets of phonon deformation potentials makes it possible to separately evaluate the impact of the anisotropy of the elastic constants and phonon deformation potential tensors. Using the isotropic averages $\bar{p}$, $\bar{q}$, and $\bar{r}$, the average discrepancy between the shifts calculated from the numerical strain and the shifts calculated from the analytical strain is 7% for a combination of nine nanowires with different dimensions. If

the comparison is limited to the Raman spectrum predicted for the *LL* scattering configuration, the discrepancy is 10%. These discrepancies must be ascribed to differences in the underlying strain calculations, since the average phonon deformation potentials are isotropic, and therefore no additional error is introduced in the Raman calculation. On the other hand, if we use the full cubic p,q,r set with the numerical strain tensors, which yields the most realistic Raman calculation, and the average $\bar{p}$, $\bar{q}$, and $\bar{r}$ with the analytical strain model, for maximum internal consistency, the error increases to 24% (16% for the *LL* configuration). The error is reduced to 9% (7% for the *LL* configuration) if the cubic p,q,r set is used in conjunction with the analytical strain model. These results demonstrate that the use of average phonon deformation potentials, while logically consistent with the use of average elastic constants, will significantly worsen the predictive capability of the analytical strain models. For maximum accuracy with an analytical strain model, the full cubic p,q,r set should be used, even though the resulting hybrid approach is not entirely consistent.

5.3.3 Shell Raman Spectra

Fig. (5.8) shows calculated Raman spectra from the shell region of the nanowire with D_{core} = 53 nm and t_{shell} = 7.2 nm, using average,

isotropic $\bar{p}$, $\bar{q}$, and $\bar{r}$ phonon deformation potentials for Si. The Raman spectra are downshifted relative to the bulk Si Raman spectrum, as expected given the overall tensile nature of the shell strain. However, they are more complex than those from the core, reflecting the non-uniformity of the strain over the shell. For incident and scattered light polarizations parallel to the nanowire axis, two broad peaks dominate the spectra. Each of these peaks corresponds mainly to a single vibrational mode whose frequency varies radially due to the radial dependence of the strain in the shell. The insets show this radial dependence. The large strain components at the interface with the core induce a sizable mode frequency splitting, which is apparent if one notes that the highest and lowest frequencies are located near the interface.

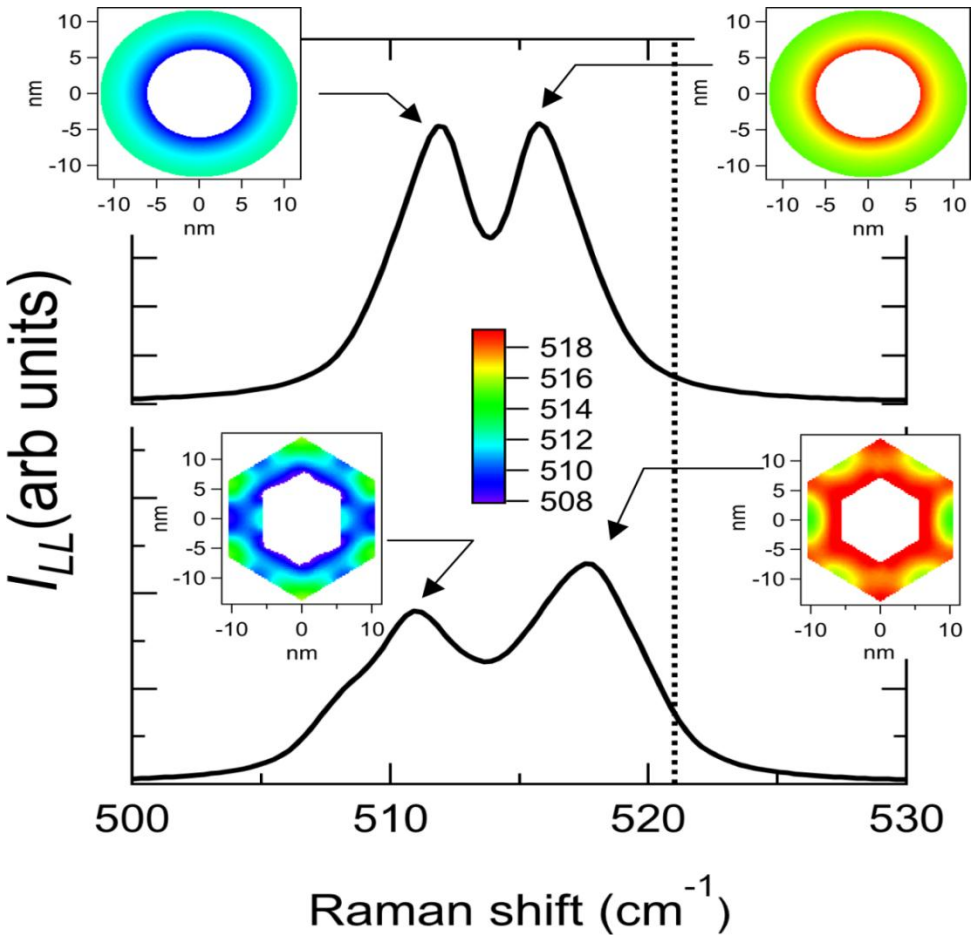

Figure 5.8 Calculated Raman spectra of the shell region of a <011> Ge-Si core-shell nanowire with D_{core} = 11 nm and t_{shell} = 5 nm, for incident and scattered light polarizations parallel to the nanowire axis. The top curve corresponds to the analytical strain model with cylindrical geometry. The bottom curve corresponds to the numerical strain calculation with realistic geometry. The spectra were calculated using the Si Voigt-averaged tensor components from Eq. (5.6). All spectra are normalized to the same area. The vertical scale is the same in all panels. The vertical dotted line is the position of the Raman peak from bulk Si. The insets show frequency maps for the Raman-active modes.

Calculations using the same phonon deformation potentials combined with the numerical strains, shown in the bottom panel of Fig. 5.8, are remarkably similar to those carried out with the analytical strain model, indicating that the analytical shell strains are a good approximation of the realistic numerical strains.

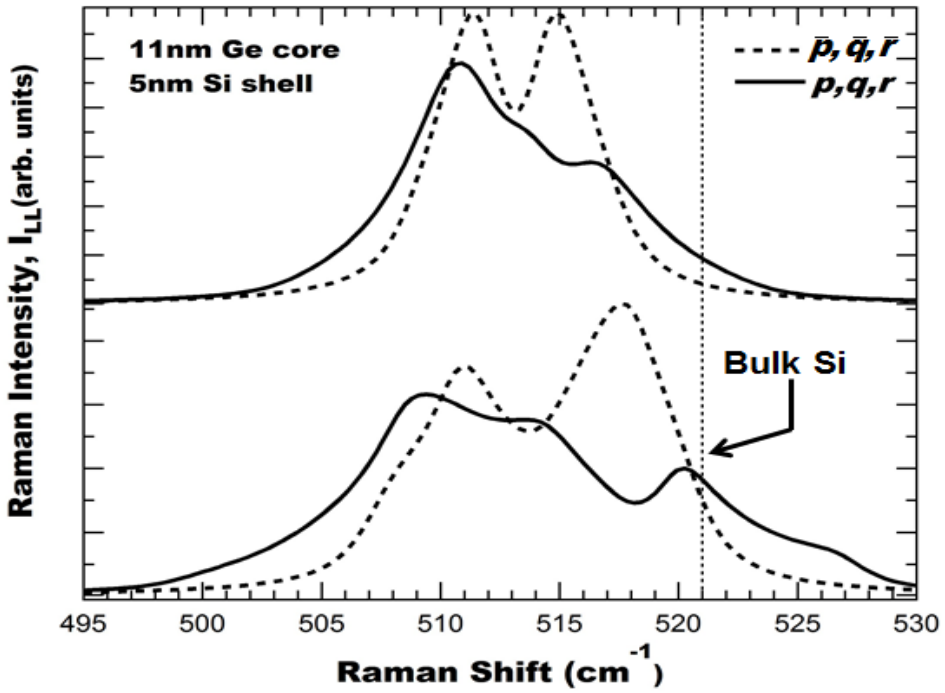

Figure 5.9 Calculated Raman spectra of the shell region of a <011> Ge-Si core-shell nanowire with D_{core} = 11 nm and t_{shell} = 5 nm, for incident and scattered light polarizations parallel to the nanowire axis. The top curves correspond to the analytical strain model with cylindrical geometry. The bottom curves correspond to the numerical strain calculation with realistic geometry. The spectra were calculated using either the full cubic p,q,r for Si from Table 5.1 (solid lines) or the Si Voigt-averaged tensor components from Eq. (5.6) (dotted lines). The latter are the same as in Fig. (5.4) and are shown here for easier comparison. All spectra are normalized to the same area. The vertical scale is the same in all panels. The vertical dotted line is the position of the Raman peak from bulk Si.

In Fig. (5.9) we repeat the calculation using the full cubic p,q,r set for Si, and we notice that, unlike the core case, the spectra are significantly distorted with respect to those calculated with isotropic phonon deformation potentials. Further splittings are observed, and there is an intensity loss of the high-frequency components. Interestingly, these features are reproduced in the calculation combining the analytical strains with the cubic p,q,r which, as in the

core calculations, is in principle inconsistent. For completeness Raman spectra with artificially low broadening were calculated for the shell region and the spectra obtained are shown in Fig.(5.9).

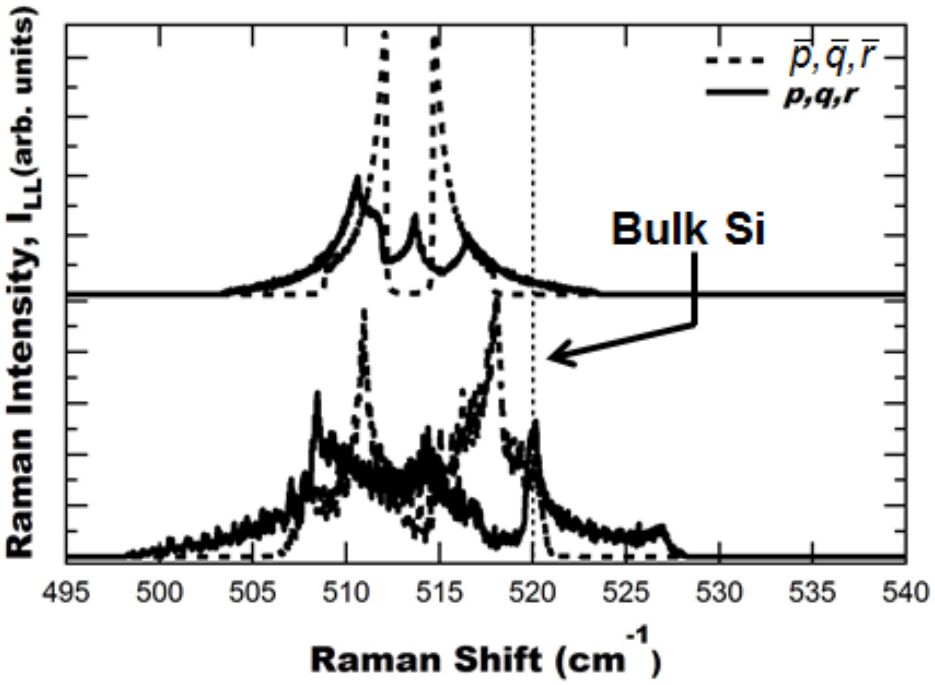

Figure 5.10 Calculated Raman spectra of the shell region of a <011> Ge-Si core-shell nanowire with D_{core} = 11 nm and t_{shell} = 5 nm, for incident and scattered light polarizations parallel to the nanowire axis with minimal Lorentzian broadening. The top curves correspond to the analytical strain model with cylindrical geometry. The bottom curves correspond to the numerical strain calculation with realistic geometry. The spectra were calculated using either the full cubic p,q,r for Si from Table 5.1 (solid lines) or the Si Voigt-averaged tensor components from Eq. (5.6) (dotted lines). The latter are the same as in Fig. (5.4) and are shown here for easier comparison. All spectra are normalized to the same area. The vertical scale is the same in all panels. The vertical dotted line is the position of the Raman peak from bulk Si.

Calculations for the other polarization configurations are shown in Fig. 5.10.

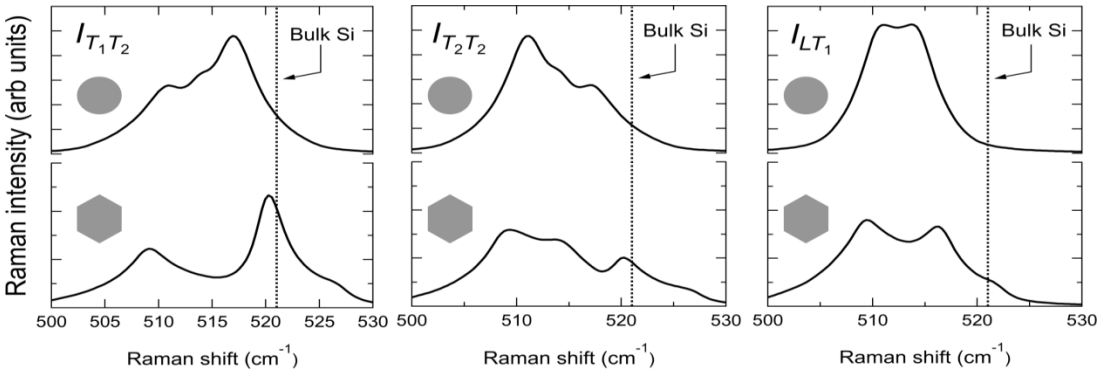

Figure 5.11 Calculated Raman spectra of the shell region of a <011> Ge-Si core-shell nanowire with D_{core} = 11 nm and t_{shell} = 5 nm. Incident and scattered light polarizations are indicated in the three different panels. The convention is L = <011>, T_1 = <100>, and $T_2 = < 01\bar{1} >$. The top curves correspond to the analytical strain model with cylindrical geometry. The bottom curves correspond to the numerical strain calculation with realistic geometry. All spectra were calculated using cubic symmetry Si *p,q, r* phonon deformation potential tensor components from Table 5.I. All spectra are normalized to the same area. The vertical scale is the same in all panels. The vertical dotted line is the position of the Raman peak in bulk Si.

APPENDIX V shows the Raman spectra of shell in LL, LT_1, T_1T_2, and T_2T_2 polarizations.

5.4 Conclusions

In this chapter we have used the numerical strain model combined with the cubic-symmetry *p,q,r* set as the benchmark reference to test the accuracy of the analytical strain model. Atomistic models [42,93,94,95] offer in principle even higher accuracy. These models incorporate phonon confinement effects, make it possible to treat the core-shell interface in a much more realistic way, including intermixing, and do not rely on the implicit continuum approximation made here, according to which each point in the sample has a different set of phonons with its own contribution to the Raman spectrum. By contrast, atomistic

calculations naturally incorporate the spatial extent of each of the vibrational modes. Unfortunately, accurate atomistic calculations normally require the use of *ab initio* methods that are computationally prohibitive for all but the smallest nanowires. Simpler models that use empirical interatomic potentials, such as the Valence Force Field approach,[42] are usually unable to reproduce the elastic and phonon properties of bulk materials with sufficient accuracy. For example, VFF models have been used to compute strain in III-V nanowires, but these models predict the material's elastic constants with errors of at least 10%, casting doubts that VFF strain predictions will be superior to predictions from numerical continuum models that use the experimental elastic constants. We believe this consideration is particularly valid for the core of our nanowires, where the uniform strain lends itself to continuum modeling, and the interface details play a minor role, as seen by the good agreement between our analytical and numerical calculations. Rücker and Methfessel have discussed the necessary generalizations of VFF-like models to be able to obtain quantitative agreement with the elastic and anharmonic properties needed to predict strain-induced Raman shifts in nanowires.[96] Their "anharmonic Keating model" is probably the best empirical potential to study the Raman spectra of core-shell nanowires,

but even with this model it is not clear that the phonon deformation potential r can be reproduced.

CHAPTER 6

RAMAN SCATTERING CHARACTERIZATION OF STRAIN IN Ge-Si NANOWIRES

6.1 Introduction

We studied the strain relaxation in Ge-Si core-shell nanowires by Raman spectroscopy. Raman spectroscopy studies were conducted on four Ge-Si core-shell nanowires and pure Ge nanowire. The experimental results were finally compared with analytical results with the introduction of the strain relaxation term which was introduced in the section (2.5).

This chapter starts with the experimental details of the core-shell nanowire. Section 6.3 discusses broadening of the Raman peak of a pure Ge nanowire and the Raman frequency shifts in the Ge-Si core-shell nanowires. Section 6.4 consists of an analysis of the strain relaxation in the Ge-Si nanowire. In section 6.5 we present the conclusions of our experiments on Ge-Si core-shell nanowires.

6.2 Experimental analysis of the core of the core-shell nanowire

6.2.1 Experimental details

Raman experiments were performed at room temperature in the back-scattering geometry using a micro-Raman system equipped with a 100× objective. Several laser lines, including 632 nm, 532 nm, and 480

nm were used to excite the spectra. The scattered light was analyzed with a single-stage 0.5 m spectrometer with 1800 lines/mm gratings and detected with a LN_2-cooled charge-coupled device detector. The incident laser power was kept below 1 mW.

The Ge-Si core-shell nanowires[97] were grown using "seedless" VLS mechanism. The Ge-core and consequently Si-shell were formed by growing Ge nanowires from planar 1/2ML of Au at temperature, T= 300^0C and pressure, P = 10mtorr of germane in the <011> crystallographic direction. Si shells were formed by adding disilane at pressure, P=3mtorr at temperature, T=540^0C. Different Si thicknesses were obtained by varying the shell deposition time from 100s to 400s. Fig.(6.1) shows 11nm Ge-core with a 9 nm Si-shell nanowire.

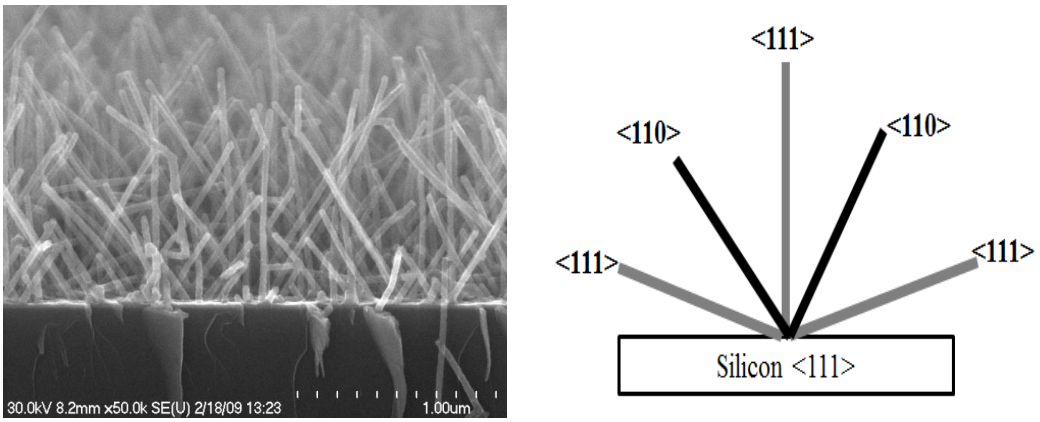

(a) (b)

Figure 6.1 (a) 11nm Ge-core with a 9.0 nm Si-shell nanowire. Courtesy of Prof. Jeff Drucker and Dr. Eric Dailey. (b) Possible <011> nanowires orientations on the Si Substrate in <111> along $<11\bar{2}>$ projection.

For our studies we mainly focused on four Ge-Si samples with Ge core diameters well above and well below the calculated value of 20 nm for a transition from core-limited to shell-limited coherency.[98] These calculations were performed for Si cores and Ge shells. We assume that transition diameters will not be very different if the core and shell materials are exchanged because the elastic energies are quadratic in the strains and the elastic properties of Ge and Si are not too different.

6.2.2 Experimental results

Fig.(6.2) shows the Raman spectrum of a pure Ge nanowire with a diameter D = 10 nm compared with the Raman spectrum from a bulk Ge sample. We notice that the peak corresponding to the nanowire sample is broader and downshifted by ~ 1.1 cm^{-1} with respect to the bulk. We find similar shifts and lineshapes for other pure Ge nanowires. The peaks are fit with Voigt profiles in which the Gaussian component has a fixed width that matches the width of the elastically scattered laser line, whereas the Lorentzian component has an adjustable width. We obtain for pure Ge a Lorentzian full width at half maximum (FWHM) of 2.35 cm^{-1}, in excellent agreement with published data.[18] On the other hand, the nanowire samples have much larger Lorentzian widths of about 4.5 cm^{-1}. Laser heating can be discarded as the source of the difference between nanowires and bulk Ge, not only

because the laser powers used are very modest, but also because the broadening and the peak shift are inconsistent if we try to explain them in terms of a different effective temperature. A Lorentzian width of 4.5 cm^{-1} implies a sample temperature of about 600 K, but the corresponding shift relative to room temperature would be about 3 cm^{-1}, much larger than the observed shift of ~1 cm^{-1}.

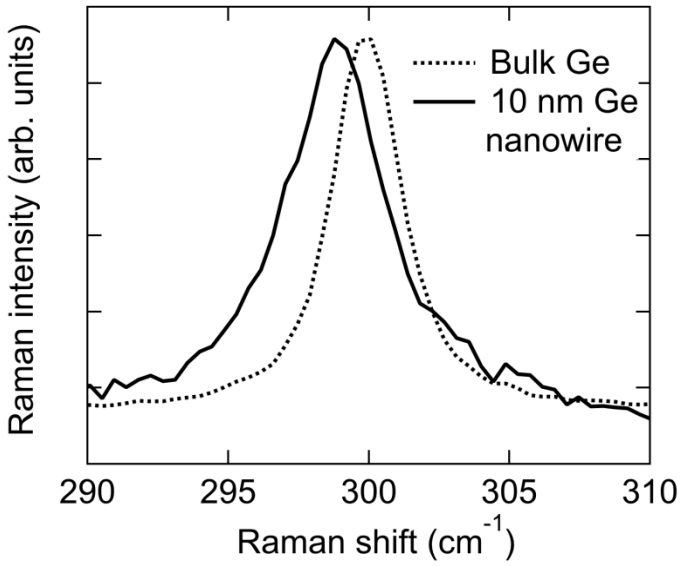

Figure 6.2: Solid line: Raman spectrum from a <011> Ge nanowire with a diameter D = 10 nm. Dotted line: Raman spectrum from a bulk Ge sample.

Possible alternative reasons for the downshift will be discussed below, but since we are interested in strain-induced Raman shifts in core-shell nanowires, it seems natural to use pure Ge nanowires as a reference, assuming that only the *differences* between pure-element and core-shell nanowires are attributable to strain. Accordingly, we

show in Fig. (6.3) the Raman spectra for core-shell nanowires as a function of the relative shift with respect to the pure Ge nanowires.

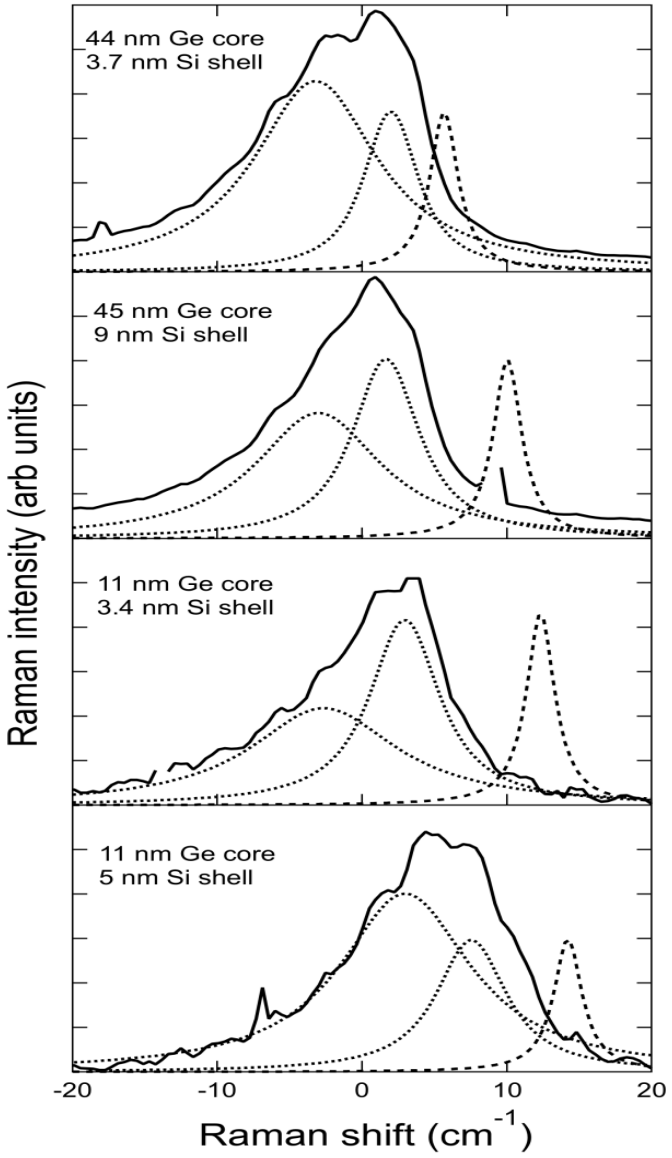

Figure 6.3 Room temperature Raman spectra of different Ge/Si core/shell nanowires in the spectral region around the Ge Raman peak frequency. The core diameter D_{core} and shell thickness t_{shell} are indicated on each panel. The solid lines are the experimental spectra. The dotted lines show the results of a fit with two spectral components. The dashed line is the theoretical prediction for fully strained core-shell nanowires, shown here with the same peak height as the high-frequency component of the two-peak fit. The Raman shifts are shown relative to the Raman frequency of bulk Ge, in the theoretical case, and relative to the Raman frequency of the pure Ge nanowire in Fig. 6.2 , in the case of the experimental data.

It is apparent from Fig. (6.3) that the Raman spectra from core-shell nanowires in the region corresponding to Ge-like vibrations are much broader that their pure Ge nanowire counterparts, and also quite asymmetric. A first possible interpretation of these spectra is that they correspond to the three strain-split phonons in the Ge core. These phonons are Raman active under different polarization selection rules,[47] and these selection rules could be used to verify the validity of this interpretation. Unfortunately, we see no difference in Raman spectra obtained under different polarization conditions, presumably due to the fact that the polarization is completely scrambled in the nanowire sample. On the other hand, the Raman spectra are expected to be dominated by the scattering corresponding to incident and scattered polarizations parallel to the nanowire axis (*LL* polarization), since the local electric field is enhanced under this polarization,[79,99,100] for which only one phonon is Raman-active. We also note that the spectra in Fig. (6.3) show substantial Raman activity at frequencies *below* that of unstrained Ge. It is not possible to explain this observation in terms of the strain-split core phonons, since all of these phonons are upshifted with respect to bulk Ge due to the overall compressive nature of the strain in the Ge core.[47] Therefore, we propose an alternative interpretation for the spectra in Fig. (6.3). We assume that the peaks have two components. The high-frequency

component is assigned to Raman scattering from the core in the *LL* polarization, and the low-frequency component is interpreted as Raman scattering from the Ge-Ge mode in a SiGe alloy located at the core-shell interface. We have fit the Raman spectra with Voigt profiles, and the two-components are shown as dotted lines in Fig. (6.3). The high-frequency component is narrower, with FWHM values between 4 cm^{-1} and 5 cm^{-1}, in good agreement with the widths observed in pure Ge nanowires (Fig.(6.2)), whereas the FWHM of the low-frequency component is much larger (~ 10-12 cm^{-1}) as expected for an alloy mode. These fit values support our interpretation of the spectra.

Also shown in Fig.(6.3) are the predicted Raman spectra for fully strained core-shell nanowires, calculated following the method described in Ref. 49 using the parameters listed in Table 4.1. It is apparent that the observed experimental upshifts in the core spectra are significantly below the theoretical predictions, strongly suggesting that our nanowires are not fully strained.

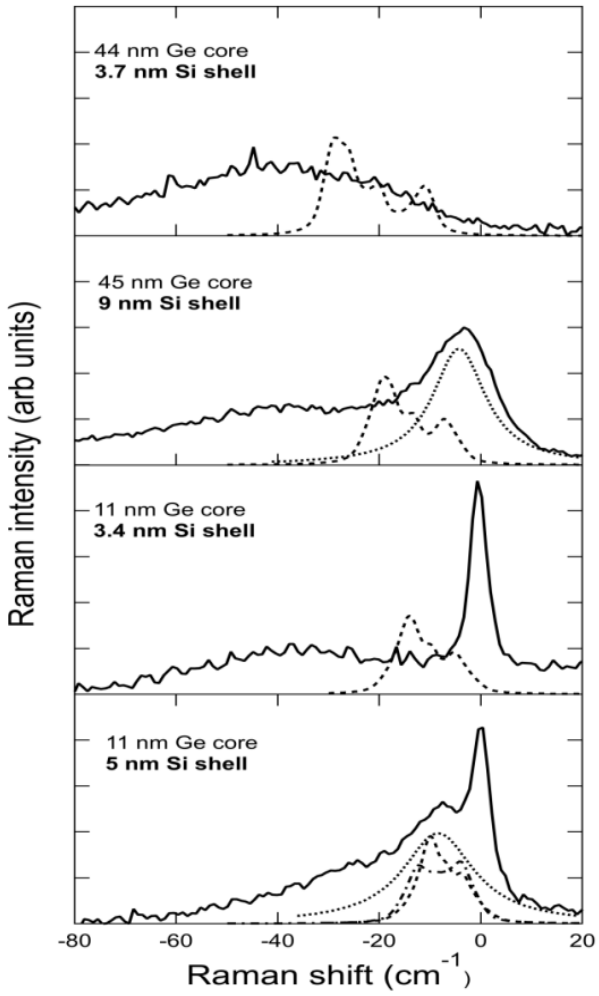

Figure 6.4 Room temperature Raman spectra of different Ge/Si core/shell nanowires in the spectral region around the Si Raman peak frequency. The core diameter D_{core} and shell thickness t_{shell} are indicated on each panel. The solid lines are the experimental spectra. The sharp peaks at zero shift correspond to the Raman signal from the Si substrates, which is not observable in the top two panels. The dotted lines show the results of fits to spectral features assigned to shell Raman peaks. The broad feature at ~-40 cm^{-1} is assigned to the Si-Si peak in the SiGe interfacial alloy. The dashed lines are the theoretical predicted shell spectra for fully strained core-shell nanowires. The dash-dotted line in the bottom panel is the predicted shell spectrum for a partially relaxed nanowire. The Raman shifts are shown relative to the Raman frequency of bulk Si, in the theoretical case, and relative to the Raman frequency of the Si substrate, in the case of the experimental data.

Fig (6.4) shows the Raman spectra from the shell region in the nanowires. Since isolated Si shells are not experimentally available,

the shifts are simply taken relative to the Si substrate. This may introduce errors on the order of ~1 cm^{-1}, but since the shell spectra are much broader, such errors are not significant. The sharp peaks observed in the two lower panels correspond to the Si substrate. Raman scattering from the substrate is not observed in the top two panels due to increased absorption by the thicker Ge cores. In all cases there is a broad feature centered at around -40 cm^{-1} that is assigned to Si-Si vibrations from the interfacial alloy invoked to explain the Ge core spectra. Evidence for shell Raman spectra are only seen for the 45/9 and 11/5 nanowires. The Raman spectra from the other two nanowires, with thinner shells, do not show any obvious evidence of a shell Raman spectrum. The dashed lines in Fig (6.4) show the predicted shell spectra for fully-strained core-shell nanowires. As explained in Refs. 49 and 102(chapter 5)[101] these spectra are broad and complex due to the radial dependence of the strain in the nanowire shell. We see that only in the case of the 11/5 nanowire there is good agreement between theory and experiment.

6.3 Analysis of Raman frequency shifts in pure Ge nanowires

For a quantitative analysis of Raman shifts in core-shell nanowires we have used as a reference the Raman spectra from pure Ge nanowires, rather than the Raman spectrum from bulk Ge. From Fig.(6.1) we

noticed that the Ge nanowire Raman spectrum is downshifted by about 1.1 cm^{-1} relative to bulk Ge, which represents a substantial fraction of the observed strain shifts. Thus this correction is important for a full characterization of the strain and deserves careful scrutiny. An explanation in terms of laser heating was discarded above. The second possibility is confinement effects. It is well known from studies on Ge/Si superlattices[102] that the Ge optical modes are well confined in Ge layers, even though they overlap in frequency with the Si longitudinal acoustic modes. This should also be the case in Ge/Si core-shell nanowires. This means that the confinement shifts should be very similar to those of pure Ge nanowires with a thickness equal to the core diameter of the core-shell structure. Confinement effects have been treated in the experimental literature using the Richter-Fauchet-Campbell (RFC) model.[103,104,105,106] The Raman spectrum is assumed to be given by

$$I(\omega) = I_0 \int_0^{q_{\max}} \frac{2\pi |C(q)|^2 \, q\,dq}{\left[\omega - \omega(q)\right]^2 + \Gamma^2}. \tag{6.1}$$

with

$$|C(q)|^2 = \exp\left[-\frac{1}{2}\left(\frac{qD}{\alpha}\right)^2\right], \tag{6.2}$$

where I_0 is a constant, D the nanowire diameter, and α a constant that is sometimes taken as adjustable parameter[104] or as $\alpha = \sqrt{8}\pi$ (Ref. 103).

It is customary to make the approximation that the phonon dispersion relation is isotropic. In that case it is appropriate to define a spherical Brillouin zone such that

$$\frac{4}{3}\pi q_{\max}^3 = \frac{(2\pi)^3}{a_0^3/4}, \tag{6.3}$$

where a_0 is the cubic lattice constant. We now define the dimensionless wave vector $x = qa$, the dimensionless frequency $y = \omega/\omega_0$, where ω_0 is the bulk Raman frequency, the dimensionless width $s = \Gamma/\omega_0$, and the dimensionless diameter $z = D/a_0$, In terms of these quantities, Eq. (6.1) becomes

$$I(y/\omega_0) = \frac{I_0}{a_0^2\omega_0^2}\int_0^{x_{\max}} \frac{(2\pi)\exp\left[-\frac{1}{2}\left(\frac{xz}{\alpha}\right)^2\right]x\,dx}{\left[y - y\left(x/a_0\right)\right]^2 + s^2}. \tag{6.4}$$

The parameter s is the same for Si and Ge at very low temperatures. This is not the case at room temperature, but s has a negligible effect on the maximum of $I(y)$, which is what we are interested in. Since the $y(x/a_0)$ curve is virtually identical for Si and Ge, we obtain a universal expression for the lineshape of both materials for a given value of z. Using the dispersion proposed in Ref.104, and α = 6.3 (Ref.104) we calculate Raman lineshapes from Eq. 6.4 and obtain the peak frequency $x_{\max}$ as a function of z. The results are very well fit with an expression of the form

$$1 - x_{\max} = \frac{A}{z^{\beta}}, \tag{6.5}$$

from which we obtain A = 0.023 and ß = 1.04. This expression provides a universal formula for confinement shifts in Si and Ge nanowires. The results are shown in Fig. (6.5), where we also compare with *ab initio* calculations of phonon frequencies in Si-Ge core-shell nanowires. The first-principles calculations were performed by Yang[93] for <011>-oriented Si nanowires with H-passivated surfaces, and fit with an expression formally identical to Eq.(6.5). However, the fit was limited to diameters less than 2.4 nm, so that extrapolation to larger diameters may involve large errors. Nevertheless, it is apparent that the RFC model significantly underestimates the confinement shifts, and that mode frequency splitting induced by confinement is not negligible. We have recomputed the shifts from the RFC model using more realistic phonon dispersion curves than those from Ref.104, but such improvements do not remove the discrepancy with the *ab initio* calculations. Unfortunately, there are no corresponding *ab initio* results for Ge nanowires, so that in Fig. 6.4(b) we have rescaled the Si nanowire results according to $\Delta\omega_{\mathrm{Ge}} = \Delta\omega_{\mathrm{Si}} \left(\omega_{0,\mathrm{Ge}}/\omega_{0,\mathrm{Si}}\right)\left(a_{0,\mathrm{Si}}/a_{0,\mathrm{Ge}}\right)^{\beta}$. For a diameter of 11 nm, as in our smallest cores, the predicted confinement shift is 1-2 cm^{-1}, in good agreement with the experimental observations, whereas the RFC model predicts much smaller shifts of

~0.3 cm^{-1} The confinement shifts become very large for nanowire diameters less than 10 nm, increasing the discrepancy between the RFC and *ab initio* models. Therefore, future Raman studies of such nanowires will have to incorporate a realistic model of phonon confinement in order to make quantitative strain determinations.

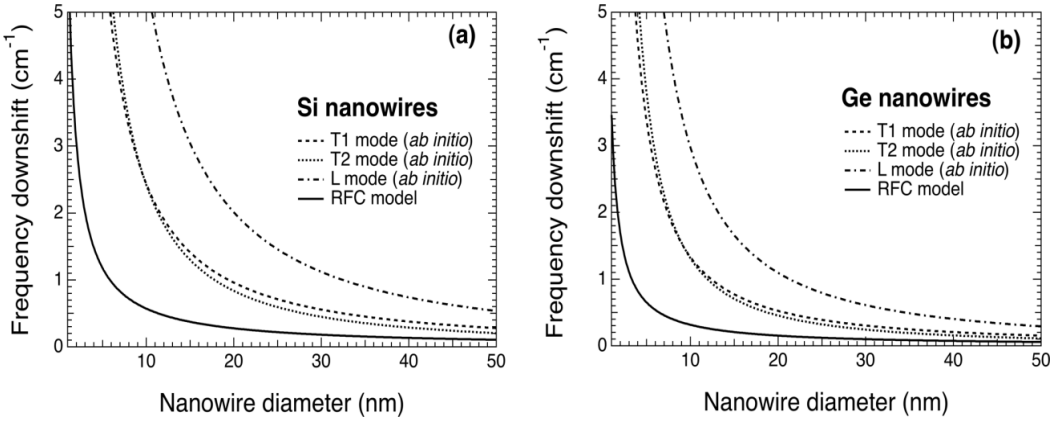

Figure 6.5 Predicted confinement frequency downshifts in pure Si and pure Ge nanowires. Solid lines are predictions from the RFC model. Dotted, dashed, and dash-dotted lines are extrapolations from *ab initio* calculations by [27] for <011> oriented Si nanowires. The triply-degenerate zone center Raman phonon in the cubic parent material is split by the lower symmetry of the nanowire. The three split modes are denoted as *T*1, *T*2, and *L*. For the case of Ge nanowires, shown in panel (b), the *ab initio* results for Si nanowires were scaled as discussed in the text.

6.4 Analysis of Strain Relaxation

A fundamental result from the strain simulations in Chapter 4 and Chapter 5 (see also Eqs. (2.78)-(2.79) in chapter 2) is that the strain tensor is uniform within the core, so that Raman scattering from the cores is ideal for strain characterization. By contrast, the non-uniform nature of the shell strain leads to broad Raman spectra that are much

more difficult to analyze. The core Raman data from all core-shell nanowires studied here show that the strain-induced shifts are much less than theoretically predicted. As indicated above, however, these deviations cannot be directly associated with strain relaxation via defects, since changes in the core and shell dimensions will also affect the strain balance. The strain partition between core and shell will also be affected by the presence of an alloy layer at the core-shell interface. Moreover, in the presence of strain relaxation associated with defects, the radial and axial components of the strain may relax differently, affecting the Raman shifts in unique ways depending on the precise relaxation mechanism.

The theoretical work by Trammel[98] and coworkers predicts that for small-diameter nanowires the core limits the strain coherency and the epitaxial failure occurs in the axial z-direction. Experimental work on <111> core-shell nanowires shows a preferential relaxation of the axial strain but little relaxation of the radial strain,[86] in agreement with the theoretical predictions. This is easy to understand, since the core axial strain is much larger than the components in the cross-sectional plane. Since these conditions also prevail in <011>-oriented nanowires, we have calculated the strain distribution and associated Raman spectra, introducing an axial strain relaxation parameter ρ discussed in Eqs. (2.78) and (2.79) for core and shell regions

respectively, such that ρ = 0 corresponds to fully strained core-shell nanowires and ρ = 1 corresponds to core-shell nanowires that are fully relaxed in the axial direction. The relaxation parameter, ρ was taken as an adjustable parameter, and we approximated the presence of an interface SiGe layer by subtracting an equal amount from the core radius and shell thickness. We find that we can simultaneously fit the core Raman spectra for the 11/5 and 11/3.4 nanowires by assuming a total SiGe thickness of 5.8 nm and a relaxation ρ = 0.7. Alternatively, one could argue that oxidation and surface roughness prevents the shell from exerting the theoretically predicted compressive stress on the core, so that a better way to simulate the results would be to assume that only the shell thickness is reduced relative to its nominal value. Proceeding this way, we find that we can fit the core spectra from the 11/5 and 11/3.4 nanowires by assuming a shell thickness "loss" of 2.8 nm and a relaxation ρ = 0.5. It is interesting to point out that these shell "losses", either via oxidation or roughness or due to intermixing, are consistent with our failure to observe any shell Raman signal in Fig (6.3) for nanowires with nominal shell thicknesses below 4 nm. In the case of the 11/5 nanowire, a clear shell Raman signal is observed, and its frequency and width are in good agreement with a theoretical calculation assuming a fully strained nanowire. This result, however, is not in contradiction with the core Raman spectra,

which, as just indicated, suggest a significant degree of relaxation. In fact, a recalculation of the shell spectra for the partially relaxed nanowires with reduced shell thicknesses (dash-dotted line in the bottom panel of Fig (6.3)) shows that shell Raman spectrum does not shift very much. This is in part due to the fact that a strain relaxation reduces the strain in the shell, but a shell thickness reduction increases its value.

The core Raman spectra for the 44/3.7 and 45/9 nanowires indicate a very large degree of relaxation. Whereas the theoretical upshifts for fully strained nanowires are 5.6 cm^{-1} and 10.1 cm^{-1}, respectively, the experimental shifts are 2.2 and 1.8 cm^{-1}. For these core diameters the relaxation study of Trammell *et al.* [8] suggests that the strain is mainly relaxed in the θ-direction, and indeed we find that even assuming full relaxation of the axial strain ($\rho = 1$), the calculated shift is larger than the observed one, indicating a breakdown of the model in Eqs. (2.78)-(2.79). Similarly, the predicted shell spectrum appears at much lower energies than observed experimentally. These results suggest a different mechanism for strain relaxation in these nanowires with thicker cores, as predicted theoretically.

6.5 CONCLUSIONS

Our Raman results indicate that none of the nanowires studied here are fully strained. This appears to be consistent with theoretical calculations of Goldthorpe *et al.*[86] based on the model developed by Liang *et al.*[40], who predict that core diameters less than 5 nm are required to accommodate a mismatch strain of ε_{misfit} = 0.04, but quantitatively in disagreement with the calculations by Trammell *et al.*[98], according to which our nanowires with core diameters of 11 nm should be able to accommodate core strains as high as $\varepsilon_{zz}^{\text{core}}$ = 0.035, well above the maximum predicted core strains in those nanowires. As we have pointed out, however, the calculations by Trammell *et al.*[98] correspond to structures with Si cores and Ge shells, a mirror version of our experimental Ge core/ Si shell structures. Moreover, our results appear to be in qualitative agreement with the argument by Trammel *et al.*[98] that for core diameters less than 20 nm epitaxial failure occurs in the axial z-direction, whereas for core diameters exceeding this value the epitaxial failure is more likely in the θ-direction.

CHAPTER 7

CONCLUSIONS

7.1 Introduction

In this dissertation we have used Raman spectroscopy to study the vibrational properties of Ge-Si core-shell nanowires. Raman spectroscopy was used to study the strain distribution in these nanowires. An elastic continuum model of strain was developed which was later compared with realistic computer simulations via the ABAQUS code to analyze the strain effects in core-shell nanowire. A detailed analysis to determine the Raman spectra of the nanowires using the numerical and analytical models is presented. Both theoretical calculations predict that the strain is essentially uniform within the core section of the nanowire, suggesting that core Raman spectra are ideal for strain characterization. We estimated that the error in the Raman determination of the strain does not exceed 10%. We also introduced a strain relaxation term for the determination of strain relaxation in core-shell nanowire and found that all Ge-Si core-shell nanowires studied here, with core diameters of 11 nm or higher, have partially relaxed strains. This also agrees with some theoretical predictions of critical thicknesses in these structures. Our Raman data also show strong evidence for Ge-Si intermixing at the core-shell interface.

7.2 Analytical and Numerical Model Results

We have computed Raman scattering spectra from Ge-Si core-shell nanowires using two alternative strain models: a simple analytical approach that assumes cylindrical symmetry and isotropic elastic constants, and a more realistic method that incorporates the exact nanowire geometry and the cubic-symmetry elastic constants of Si and Ge. The second approach solves the elastic problem numerically using a realistic geometry and the full cubic, non-isotropic elastic constant tensors for both materials. From the point of view of strain characterization, the most significant prediction of the analytical model is the uniformity of the strain within the core region of the nanowires. This prediction is largely confirmed by the numerical calculation, and the strains computed via the two methods are in very good quantitative agreement. The predicted Raman strain shifts from the two models differ on average by no more than 10%, and therefore this is roughly the error incurred if the strain is extracted from the Raman data. The accuracies on the order of 10% are obtained by using a hybrid approach in which strain is computed by assuming isotropic elastic properties but the phonon strain shifts are calculated using the full cubic, anisotropic set of parameters p,q,r. A more consistent approach in which the phonon deformation potential tensor is Voigt-

averaged over all directions leads to larger errors, which we associate with the very strong anisotropy of the phonon deformation potentials.

The shell Raman spectra obtained from the analytical and numerical strain models are in good agreement. This is gratifying from the point of view of the validity of the analytical strain model, but of limited value for strain characterization given the broadening of the peaks caused by the non-uniform shell strains.

For the strain levels involved in core-shell nanowires, we predict substantial differences between Raman spectra obtained for different scattering configurations. Thus the characterization of strain in nanowires seems to require a precisely controlled geometry in which all nanowires in the scattering sample are oriented identically. On the other hand, if the local electric fields are preferentially enhanced for polarization parallel to the nanowire axis, the Raman spectrum should be dominated by the *LL* scattering configuration, regardless of nanowire orientation.

7.3 Core-shell nanowire Experiment Results

We have analyzed the strain relaxation in Ge-Si core-shell nanowires by means of Raman spectroscopy. We also introduced a strain relaxation term in our analytical model to analyze the strain relaxation in our Raman experiments of core-shell nanowires. Our

Raman results for Ge-Si core-shell nanowires with core diameters of 11 nm or higher indicates that none of the nanowires studied here are fully strained, which also agrees with some theoretical predictions of critical thicknesses in these structures. Our Raman data also shows strong evidence for Ge-Si intermixing at the core-shell interface. In summary, this study demonstrates that Raman scattering can be a powerful tool for characterizing core-shell nanowires.

REFERENCES

[1]Michael Faraday, *Phil. Trans. R. Soc. Lond.* **147**,145 (1857).

[2] J. Turkevich, *Gold Bull.* **18**, 86; 125 (1985).

[3] M.S. Dresselhaus, Y.M Lin, O. Rabin, M.R. Black , and G. Dresselhaus,"Nanowires" 1, (2003).

[4] M. Law, J. Goldberger and P. Yang, *Annu. Rev. Mater. Re.* **34** , 83 (2004).

[5] C.M Lieber *Sci. Am* **285**, 59 (2001).

[6] C. Thelander, P. Agarwal, S.Brongersma, J. Eymery, F.L Feiner, A. Forchel ,M. Scheffler,W. Riess, J.B. Ohisson, U. Gösele and I. Samuelson, *Materials Today* **9**, 28 (2008).

[7] J. Appenzeller, J. Knoch, T.M. Björk, H. Riel, H. Schmid and W. Riess, *IEEE* **55**, 2827 (2004).

[8] R.S. Wagner and W.C. Ellis, *Appl. Phys . Lett* .**4**, 89 (1964).

[9] E.I. Givargizov, *J. Cryst. Growth* **31**, 20 (1975).

[10]J. Westwater, D.P. Gosain and S. Usui, *Jpn. J. Appl. Phys* **36**, 6204 (1997).

[11] Y. Wu and P. Yang, *Chem. Mater* **12**, 605 (2000).

[12] J. W. Dailey, J. Taraci, T. Clement, David J. Smith, Jeff Drucker, and S. T. Picraux, *J. Appl. Phys.* **96**, 7556, (2004).

[13]M.S. Gudiksen and C.M. Lieber. *J . Am. Chem. Soc* **122** , 8801 (2000).

[14] X. Duan and C.M Leiber, *Adv. Mater* **12**, 298, (2000).

[15] Z. Zhong, F,Qian, D.Wang, and C.M. Lieber, *Nano Lett.* **3**, 343 (2003).

[16] D. A. Wharam, T. J. Thornton, R. Newbury, M. Pepper, H. Ahmed, J. E. F. Frost, D. G. Hasko, D. C. Peacock, D. A. Ritchie and G. A. C. Jones, *J. Phys. C : Solid State Phys.* **21**, L209 (1988).

[17] B. J. van Wees, H. van Houten, C. W. J. Beenakker, J. G. Williamson,L. P. Kouwenhoven, D. van der Marel and C. T. Foxon, *Phys. Rev. Lett.* **60**, 848 (1988).

[18] D.L. Hicks and M.S. Dresselhaus, *Phys .Rev. B.* **47**, 12727 (1993).

[19] D.L. Hicks and M.S. Dresselhaus, *Phys .Rev. B.* **47**, 16631 (1993).

[20] X. Lu, J. H. Chu, and W. H. Shen, *J. Appl. Phys.* **93**, 1219 (2003).

[21] D. Li , Y.Wu , P. Kim . L. Shi, N. Mingo , Y. Liu , P. Yang and A.Majumdar *Appl. Phys. Lett.* **83**, 2934 (2003).

[22] J. Heremans, C. M. Thrush,Z. Zhang, X. Sun,M. S. Dresselhaus ,J. Y. Ying and D. T. Morelli, *Phys. Rev. B* **58**, 91 (1998).

[23] Ch. Kaiser, G Weiss, T. W. Cornelius, M.E. Toimil-Molares and R. Neumann, *J. Phys.: Condens. Matter* **21**, 205301 (2009).

[24] P.L.Hernandez-Martinez, Ohio University, 2010

[25]X. Duan ,Y .Huang ,Y. Cui ,J. Wang and C.M Lieber, *Nature* **409** , 66 (2001).

[26] Y. Cui and C.M Lieber, *Science* **291**, 851 (2001).

[27] Y. Huang, X. Duan, Y. Cui, and C. M. Lieber, *Nano Lett.* **2**, 101 (2002).

[28] J. R. Kim, H. Oh, H.M.So, J.J. Kim, J. Kim, C.J. Lee and S.C.Lyu, *Nanotechnology* **13** , 701 (2002).

[29] V. Schmidt, H. Riel, S. Senz, S. Karg, W. Riess,and U. Gösele., *Small* **2**, 85 (2006).

[30]M.T. Björk, O. Hayden, H. Schmid, H. Riel and W. Riess, *Appl . Phys. Lett*. **90**, 142110 (2007).
[31] O. Hayden, M. T. Björk, H. Schmid, H. Riel, U. Drechsler, S.F. Karg, E. Lörtscher and W. Reiss, *Small* **3**, 230, (2007).

[32] J. Knoch, M. T. Björk, H. Riel, H. Schmid and W. Reiss, *IEEE* **978** , 173 (2008).

[33] Y. Li, K. Buddharaju, N. Singh, G.Q. Lo and S.J. Lee, 9th *International Power & Energy Conference (IPEC 2010)*, p. 1181 (2010).

[34] A.I. Hochbaum, R. Chen, R. D. Delgado, W. Liang, E. C. Garnett, M.Najarian, A. Majumdar and P. Yang, *Nature* **451**, 163 (2008).

[35] X. Duan ,Y .Huang ,Y. Cui ,J. Wang and C.M Lieber, *Nature* **409,** 66 (2001).

[36] Y. Li, F. Qian, J. Xiang and C.M. Lieber, *Materials Today* **9**, 18 (2006).

[37] E. Dailey and J. Drucker, *Journal of Applied Physics* **105**, 064317 (2009).

[38] H.W. Seo, S.Y. Bae, J. Park, H. Yang, K.S. Park, and S. Kim, *Journal of Chem Phys*. **116**, 9492 (2002).

[39] T. Sadowski and R. Ramprasad, *J. Phys. Chem*. **114**, 1173 (2010).

[40] Y. Liang, W. D. Nix, P. B. Griffin, and J. D. Plummer, *J. Appl. Phys.* **97**, 043519 (2005).

[41] N. Søndergaard, Y. He, C. Fan, T. Guhr and H.Q. Xu, *J. Vac. Sci. Technol. B* **27**, 827 (2009).

[42] J. Grönqvist, N. Søndergaard, F. Boxberg, T. Guhr, S. Aberg and H.Q. Xu, *J. Appl. Phys*. **106**, 053508 (2009).

[43] L. J. Lauhon, M. S. Gudiksen, D. Wang, and C. M. Lieber, *Nature* **420**, 57, (2002).

[44] O. Hayden, R. Agarwal, and W. Lu, *Nano Today* **3**, 12 (2008).

[45] S. A. Dayeh, A. V. Gin, and S. T. Picraux, *Appl. Phys. Lett.* **98**, 163112 (2011).

[46] Y. Liang, W. D. Nix, P. B. Griffin, and J. D. Plummer, *J. Appl. Phys.* **97**, 043519 (2005).

[47] J. Menéndez, R. Singh, and J. Drucker, *Annalen der Physik* **523**, 145 (2011).

[48] I. Zardo, G. Abstreiter, and A. Fontcuberta i Morral, in *Nanowires*, edited by Paola Prete (Intech, Rijeka, 2010), pp. 227.

[49] V. Laneuville , F. Demangeot, R. Pécho , P. Salles and A. Ponchet, *Phys. Rev. B* **83**, 115417 (2008).

[50] J.F. Nye, *"Physical properties of crystals*" Oxford University Press, Chapters: 4, 5, 8 (1964).

[51] M.T. Atanackovic and A. Guran "*Theory of elasticity for scientists and engineers"* (Birkhäuser Boston) Chapter 3 (2000).

[52] A. Boresi, O.M Sidebottom, F.B. Seely and J.O.Smith "*Advanced Mechanics of Materials"* (John Wiley and Sons) Chapter 1 (1978).

[53] A. Boresi, O.M Sidebottom, F.B. Seely and J.O.Smith "*Advanced Mechanics of Materials"* (John Wiley and Sons) p. 77 (1978).

[54] K. Charles "*Introduction of Solid State Physics*" (John Wiley & Sons, Inc.) Eighth edition , Chapters: 1,2 (2005).

[55] M. Born and K. Huang "*Dynamical theory of crystal lattices*" (Oxford University Press) Chapter 4 (1998).

[56] J. Page "*Lectures notes of PHY 598*", Group theory, p. 112(1-8), (2008).

[57] M.J.H. Smith, *Phil. Trans. R. Soc. Lond. A* **241**, 105 (1948).

[58] P.Giannozzi, S.D.Gironcoli, P.Pavone and S. Baroni, *Phys. Rev. B* **43**, 7231 (1991).
[59] J. Page "*Lectures notes of PHY 598"* Group theory, p.118-(1-6), (2008).

[60] J. Page "*Lectures notes of Prof John Page obtained from Prof Jose Menendez*" , p.218-229.

[61] M. Cardona and G. Güntherodt " *Light scattering in solids ll*" (Springer-verlag , Berlin , New york) p. 45 (1982).

[62] J. Page "*Lectures notes of Prof John Page obtained from Prof Jose Menendez*" , p:239-244.

[63] M. Cardona and G. Güntherodt " Light scattering in solids ll" (Springer-verlag , Berlin , New york) p: 99-101 (1982).

[64] R. Loudon, " *Quantum theory of light*" (Oxford University Press) Section 4.1, p.126-127 (2000).

[65] R. Loudon, " *Quantum theory of light*" (Oxford University Press) Section 2.4, p. 20 (2000)

[66]R. Loudon, "*Quantum theory of light*" (Oxford University Press) Section 8.7, p. 373 (2000).

[67] R. Loudon, " *Quantum theory of light*" (Oxford University Press) Section 8.7, p, 371-374 (2000).

[68] R. Loudon, *"Quantum theory of light*" (Oxford University Press) Section 8.8, p. 374-379 (2000).

[69] W.H. Weber and R. Merlin, "*Raman Scattering in materials science*" (Springer) Section 3.1.3, p. 66 (2000).

[70] W.H. Weber and R. Merlin "*Raman Scattering in materials science*" (Springer) , Section 3.1.3, p. 68 (2000).

[71] W.H. Weber and R. Merlin, "*Raman Scattering in materials science*" (Springer) Section 3.1.3, p. 368 (2000).

[72] E. Anastassakis, and M. Cardona, "*High Pressure in Semiconductor Physics* II" edited by T. Suski, and W. Paul (Academic Press, New York, 1998).

[73] E. Anastassakis, *Acta Physica Hungarica* **74**, 83 (1994)

[74] Princeton Instruments Software : "*http://www.princetoninstruments.com/products/software*"

[75] J.J Wortman and R.A Evans, J. Appl. Phys. 36, 153 (1965).

[76] O. Madelung, *Physics of Group IV Elements and III-V Compounds* (Springer-Verlag, Berlin, 1982), Vol. 17a

[77] J. P. Hirth, and J. Lothe, *Theory of Dislocations* (McGraw-Hill, New York, 1968), p. 780

[78] H. J. McSkimin, and P. Andreatch, Jr., *J. Appl. Phys.* **35**, 3312, (1964).

[79]G. Chen, J. Wu, Q. Lu, H. R. Gutierrez, Q. Xiong, M. E. Pellen, J. S. Petko, D. H. Werner, and P. C. Eklund, *Nano Lett.* **8**, 1341 (2008).

[80] I. Zardo, S. Conesa-Boj, F. Peiro, J. R. Morante, J. Arbiol, E. Uccelli, G. Abstreiter, and A. Fontcuberta i Morral, *Phys. Rev. B* **80**, 245324 (2009).

[81] E. O. Schafer-Nolte, T. Stoica, T. Gotschke, F. Limbach, E. Sutter, P. Sutter, and R. Calarco, *Appl. Phys. Lett.* **96**, 091907 (2010).

[82] J. M. J. den Toonder, J. A. W. van Dommelen, and F. P. T. Baaijens, Modelling and Simulation in Materials Science and Engineering **7** (6), 909 (1999).

[83]O. Madelung, in Landolt-Börstein: Numerical Data and Functional Relationships in Science and Technology, edited by O. Madelung (Springer-Verlag, Berlin, 1985), Vol. 22a.

[84] O. Madelung, in *Landolt Börstein* (Springer-Verlag,, Berlin, New York, 2001), Vol. 41-Aα.

[85] S. Bagchi and J. Menéndez, (unpublished) (2011).

[86] I. A. Goldthorpe, A. F. Marshall, and P. C. McIntyre, *Nano Lett.* **9**, 3715 (2009)

[87] D. D. D. Ma, C. S. Lee, F. C. K. Au, S. Y. Tong, and S. T. Lee, *Science* **299**, 1874 (2003).

[88] Y. Wu, Y. Cui, L. Huynh, C. J. Barrelet, D. C. Bell, and C. M. Lieber, *Nano Lett.* **4**, 433 (2004).

[89] L. Cao, B. Nabet, and J. E. Spanier, *Phys. Rev. Lett.* **96** , 157402 (2006).

[90] I. Zardo, S. Conesa-Boj, F. Peiro, J. R. Morante, J. Arbiol, E. Uccelli, G. Abstreiter, and A. Fontcuberta i Morral, *Phys. Rev. B* **80**, 245324 (2009).

[91] E. O. Schafer-Nolte, T. Stoica, T. Gotschke, F. Limbach, E. Sutter, P. Sutter, and R. Calarco, *Appl. Phys. Lett.* **96**, 091907 (2010).

[92] J. Menéndez and M. Cardona, *Phys. Rev. B* **29**, 2051 (1984).

[93] L. Yang, Georgia Institute of Technology, 2006.

[94] L. Yang, R. Musin, X.-Q. Wang, and M. Chou, *Phys. Rev. B* **77**, 195325 (2008).

[95] Y. Zhang and Y. Xiao, *Eur. Phys. J. B* **63**, 425 (2008).

[96] H. Rücker and M. Methfessel, *Phys. Rev. B* **52**, 11059 (1995).

[97] E. Dailey, Arizona State Univeristy, 2010.

[98] T. E. Trammell, X. Zhang, Y. Li, L.-Q. Chen, and E. C. Dickey, J. Cryst. Growth **310** (12), 3084 (2008)

[99] I. Zardo, S. Conesa-Boj, F. Peiro, J. R. Morante, J. Arbiol, E. Uccelli, G. Abstreiter, and A. Fontcuberta i Morral, Phys. Rev. B **80** (24), 245324 (2009).

[100] E. O. Schafer-Nolte, T. Stoica, T. Gotschke, F. Limbach, E. Sutter, P. Sutter, and R. Calarco, Appl. Phys. Lett. **96** (9), 091907 (2010).

[101] R. Singh, E. J. Dailey, J. Drucker, and J. Menéndez, (unpublished) (2011)

[102] R. Schorer, G. Abstreiter, S. d. Gironcoli, E. Molinari, H. Kibbel, and H. Presting, Phys. Rev. B **49** (8), 5406 (1994)

[103] S. Piscanec, M. Cantoro, A. C. Ferrari, J. A. Zapien, Y. Lifshitz, S. T. Lee, S. Hofmann, and J. Robertson, Phys. Rev. B **68** (24), 241312 (2003).

[104]K. W. Adu, H. R. Gutiérrez, U. J. Kim, G. U. Sumanasekera, and P. C. Eklund, Nano Lett. **5** (3), 409 (2005).

[105] A. K. Arora, M. Rajalakshmi, T. R. Ravindran, and V. Sivasubramanian, J. Raman Spectrosc. **38** (6), 604 (2007).

[106] I. Zardo, G. Abstreiter, and A. Fontcuberta i Morral, in *Nanowires*, edited by Paola Prete (Intech, Rijeka, 2010), pp. 227.

APPENDIX I

STRAIN GRAPHS OF THE CORE SHELL NANOWIRE

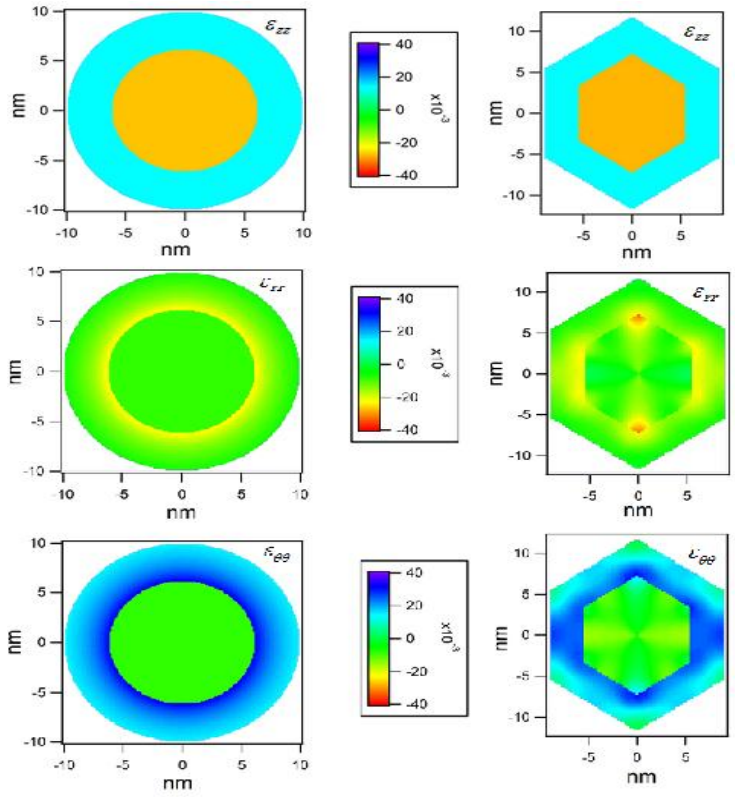

Figure A1a Comparison of the diagonal components of the strain tensor for a <011> Ge-Si core-shell nanowire with D_{core} = 11 nm and t_{shell} = 3.4 nm obtained with the analytical expressions in Eqs. (5.1)-(5.6) (left) and the numerical finite-element package ABAQUS (right).

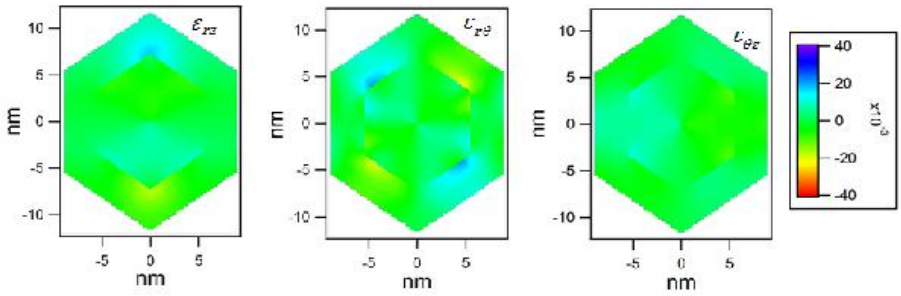

Figure A1b Off-diagonal components of the strain tensor for a <011> Ge-Si core-shell nanowire with D_{core} = 11 nm and t_{shell} = 3.4 nm obtained with the numerical finite-element package ABAQUS (right). The corresponding components in the analytical model of Eqs. (5.1)-(5.6) are exactly zero

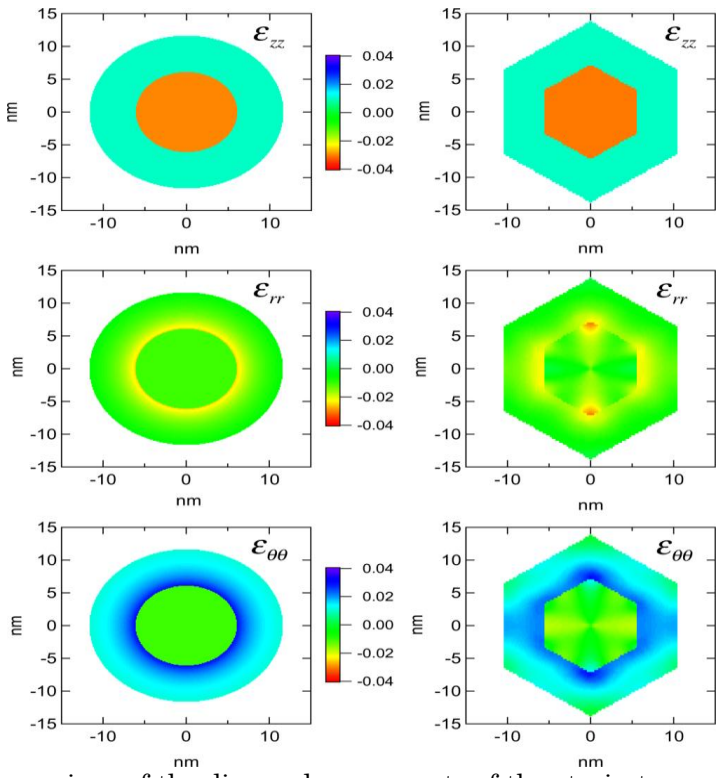

Figure A2a Comparison of the diagonal components of the strain tensor for a <011> Ge-Si core-shell nanowire with D_{core} = 11 nm and t_{shell} = 5 nm obtained with the analytical expressions in Eqs. (5.1)-(5.6) (left) and the numerical finite-element package ABAQUS (right).

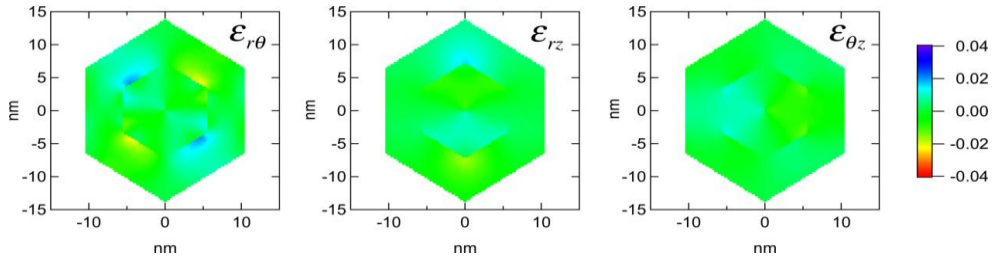

Figure A2b Off-diagonal components of the strain tensor for a <011> Ge-Si core-shell nanowire with D_{core} = 11 nm and t_{shell} = 5 nm obtained with the numerical finite-element package ABAQUS (right). The corresponding components in the analytical model of Eqs. (5.1)-(5.6) are exactly zero.

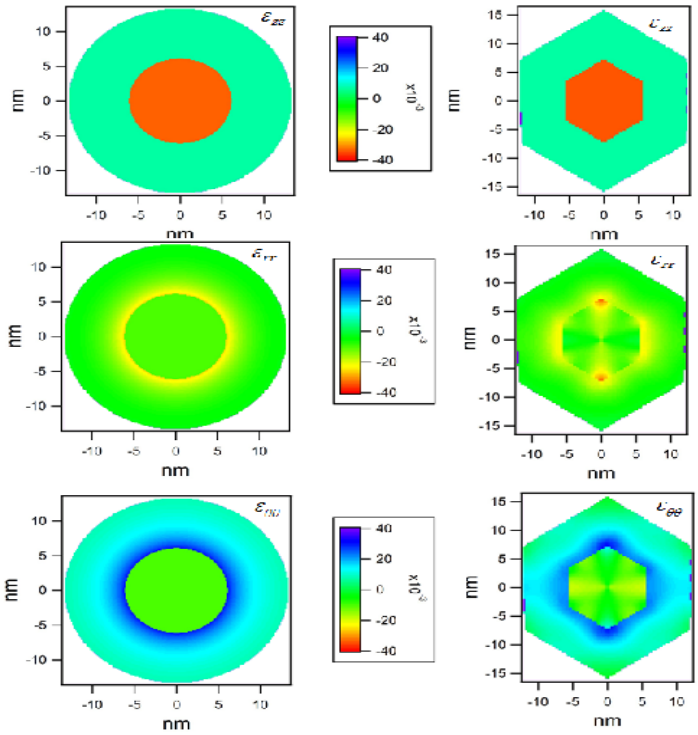

Figure A3a Comparison of the diagonal components of the strain tensor for a <011> Ge-Si core-shell nanowire with D_{core} = 11 nm and t_{shell} = 6.5 nm obtained with the analytical expressions in Eqs. (5.1)-(5.6) (left) and the numerical finite-element package ABAQUS (right).

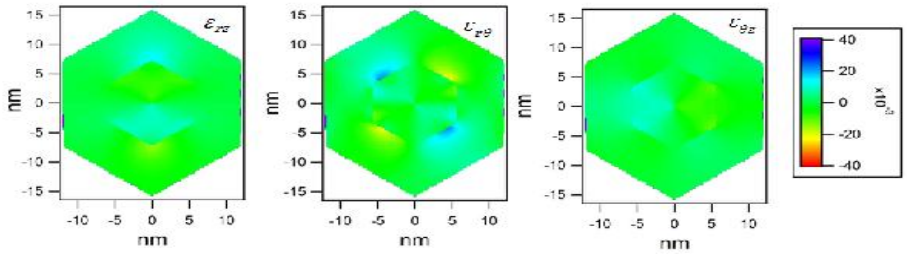

Figure A3b Off-diagonal components of the strain tensor for a <011> Ge-Si core-shell nanowire with D_{core} = 11 nm and t_{shell} = 6.5 nm obtained with the numerical finite-element package ABAQUS (right). The corresponding components in the analytical model of Eqs. (5.1)-(5.6) are exactly zero.

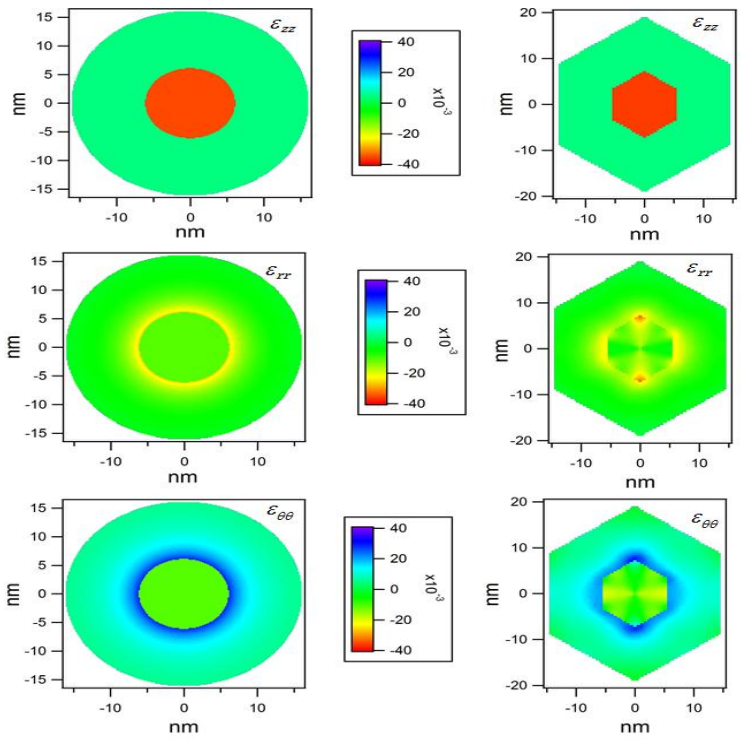

Figure A4a Comparison of the diagonal components of the strain tensor for a <011> Ge-Si core-shell nanowire with D_{core} = 11 nm and t_{shell} = 9 nm obtained with the analytical expressions in Eqs. (5.1)-(5.6) (left) and the numerical finite-element package ABAQUS (right).

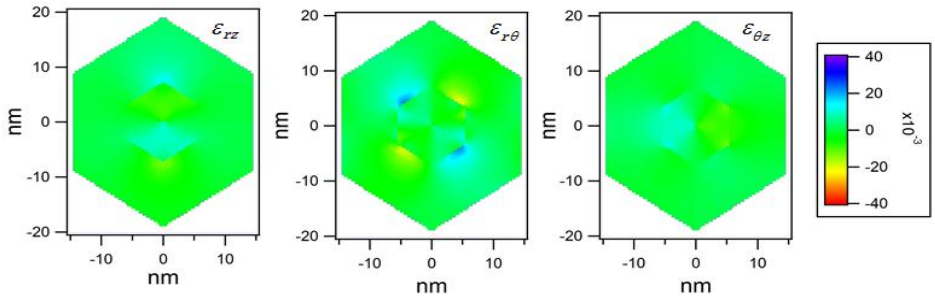

Figure A4b Off-diagonal components of the strain tensor for a <011> Ge-Si core-shell nanowire with D_{core} = 11 nm and t_{shell} = 9 nm obtained with the numerical finite-element package ABAQUS (right). The corresponding components in the analytical model of Eqs. (5.1)-(5.6) are exactly zero.

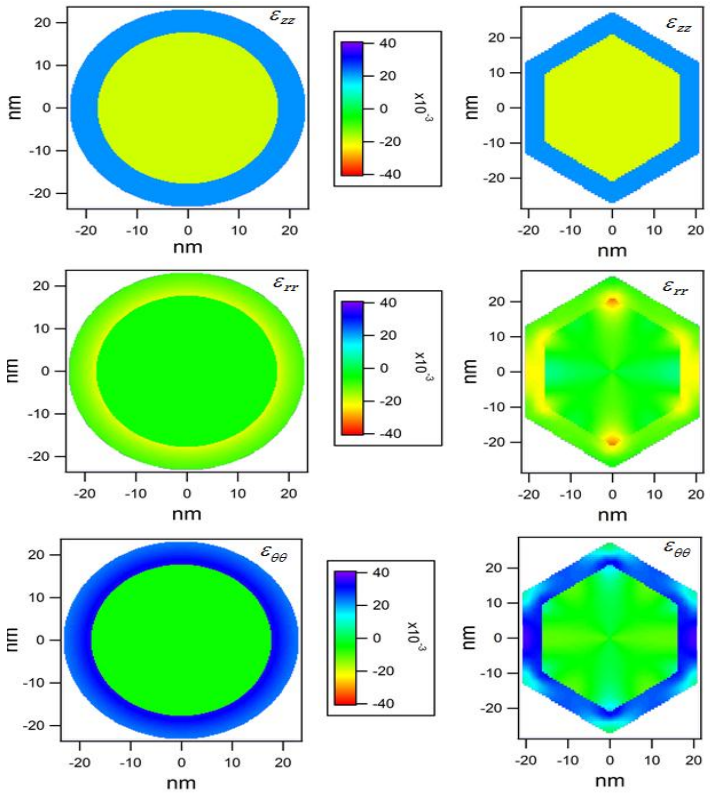

Figure A5a Comparison of the diagonal components of the strain tensor for a <011> Ge-Si core-shell nanowire with D_{core} = 32 nm and t_{shell} = 4.9 nm obtained with the analytical expressions in Eqs. (5.1)-(5.6) (left) and the numerical finite-element package ABAQUS (right).

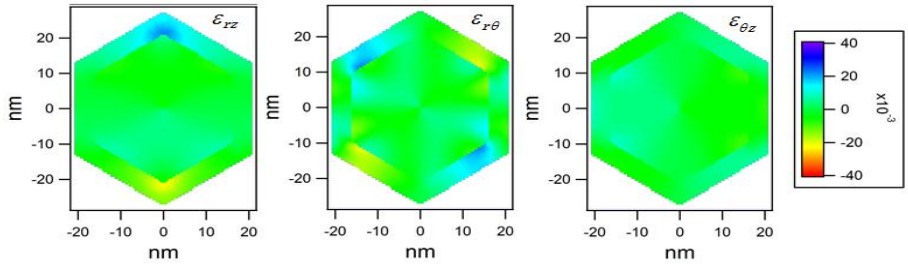

Figure A5b Off-diagonal components of the strain tensor for a <011> Ge-Si core-shell nanowire with D_{core} = 32 nm and t_{shell} = 4.9 nm obtained with the numerical finite-element package ABAQUS (right). The corresponding components in the analytical model of Eqs. (5.1)-(5.6) are exactly zero.

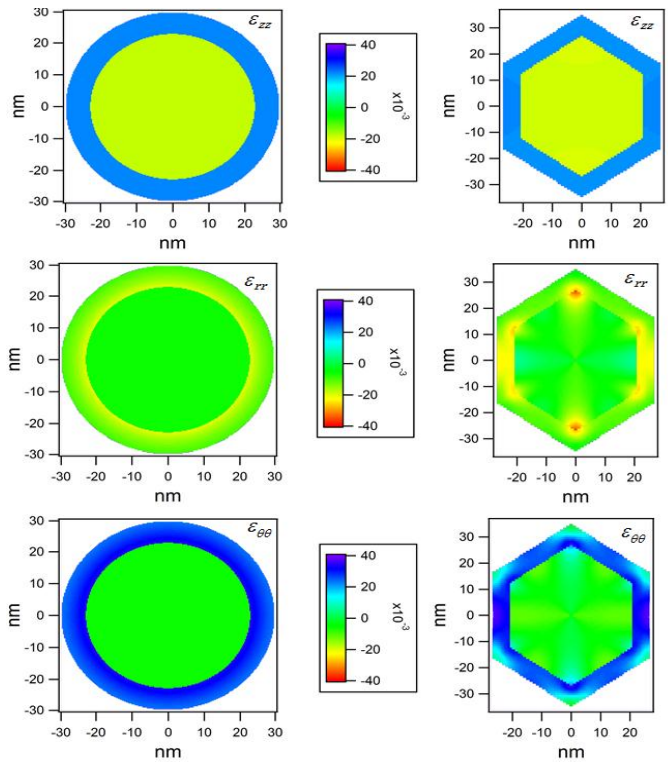

Figure A6a Comparison of the diagonal components of the strain tensor for a <011> Ge-Si core-shell nanowire with D_{core} = 41 nm and t_{shell} = 6.1 nm obtained with the analytical expressions in Eqs. (5.1)-(5.6) (left) and the numerical finite-element package ABAQUS (right).

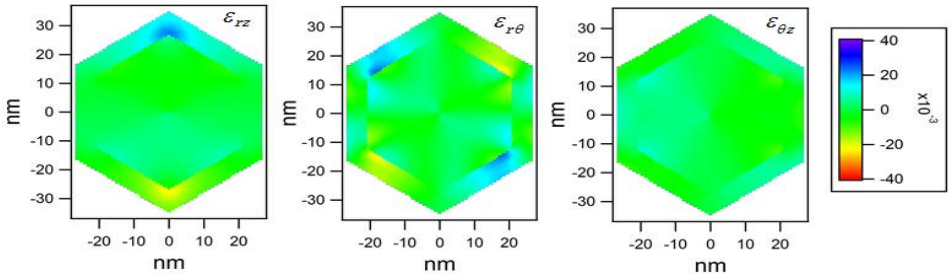

Figure A6b Off-diagonal components of the strain tensor for a <011> Ge-Si core-shell nanowire with D_{core} = 41 nm and t_{shell} = 6.1 nm obtained with the numerical finite-element package ABAQUS (right). The corresponding components in the analytical model of Eqs. (5.1)-(5.6) are exactly zero.

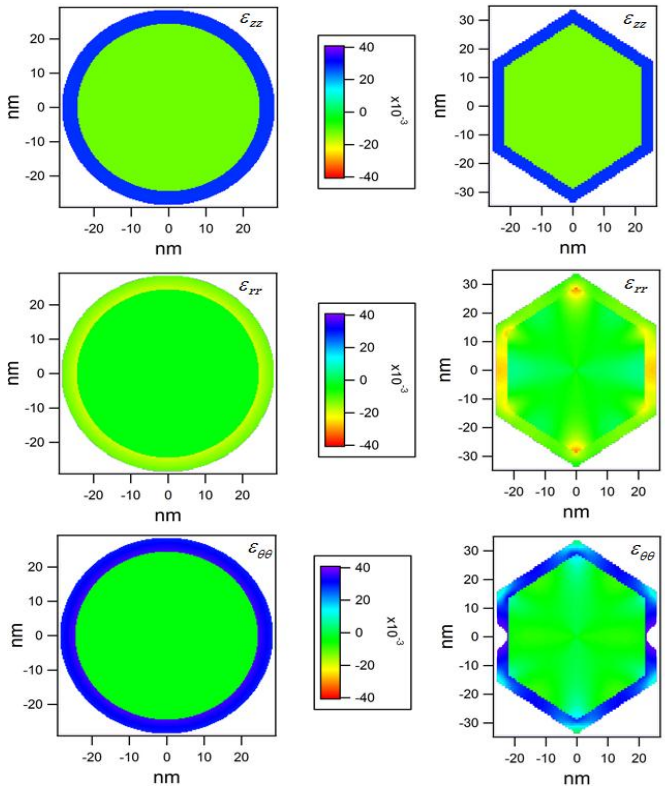

Figure A7a Comparison of the diagonal components of the strain tensor for a <011> Ge-Si core-shell nanowire with D_{core} = 44 nm and t_{shell} = 3.7 nm obtained with the analytical expressions in Eqs. (5.1)-(5.6) (left) and the numerical finite-element package ABAQUS (right).

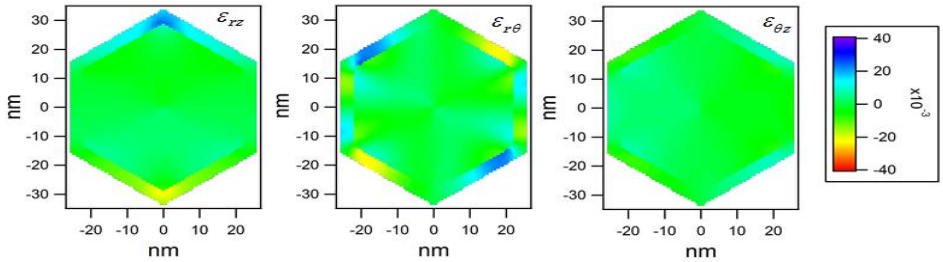

Figure A7b Off-diagonal components of the strain tensor for a <011> Ge-Si core-shell nanowire with D_{core} = 44 nm and t_{shell} = 3.7 nm obtained with the numerical finite-element package ABAQUS (right). The corresponding components in the analytical model of Eqs. (5.1)-(5.6) are exactly zero.

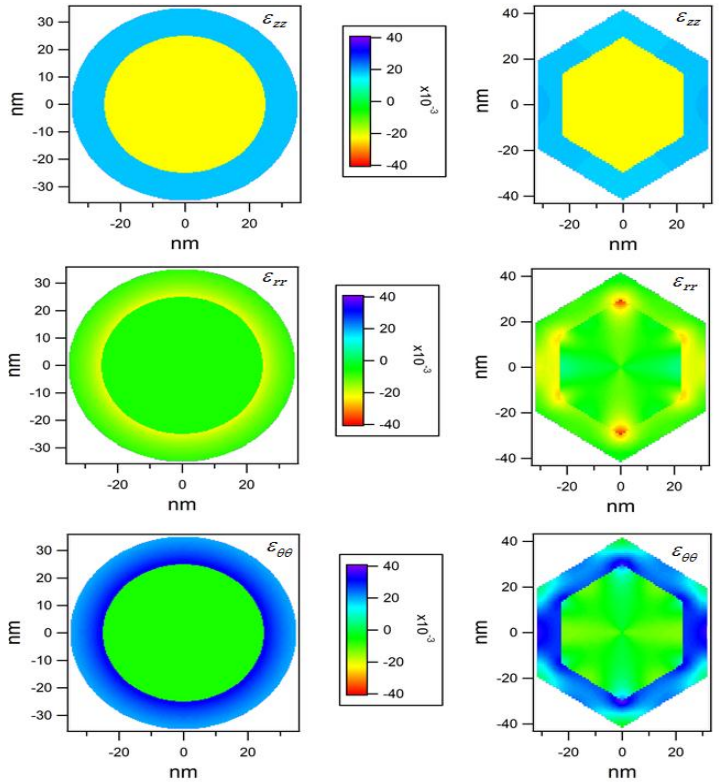

Figure A8a Comparison of the diagonal components of the strain tensor for a <011> Ge-Si core-shell nanowire with D_{core} = 45 nm and t_{shell} = 9.1 nm obtained with the analytical expressions in Eqs. (5.1)-(5.6) (left) and the numerical finite-element package ABAQUS (right).

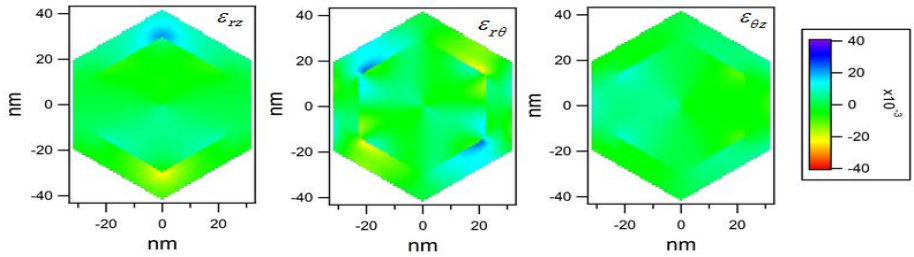

Figure A8b Off-diagonal components of the strain tensor for a <011> Ge-Si core-shell nanowire with D_{core} = 44 nm and t_{shell} = 3.7 nm obtained with the numerical finite-element package ABAQUS (right). The corresponding components in the analytical model of Eqs. (5.1)-(5.6) are exactly zero.

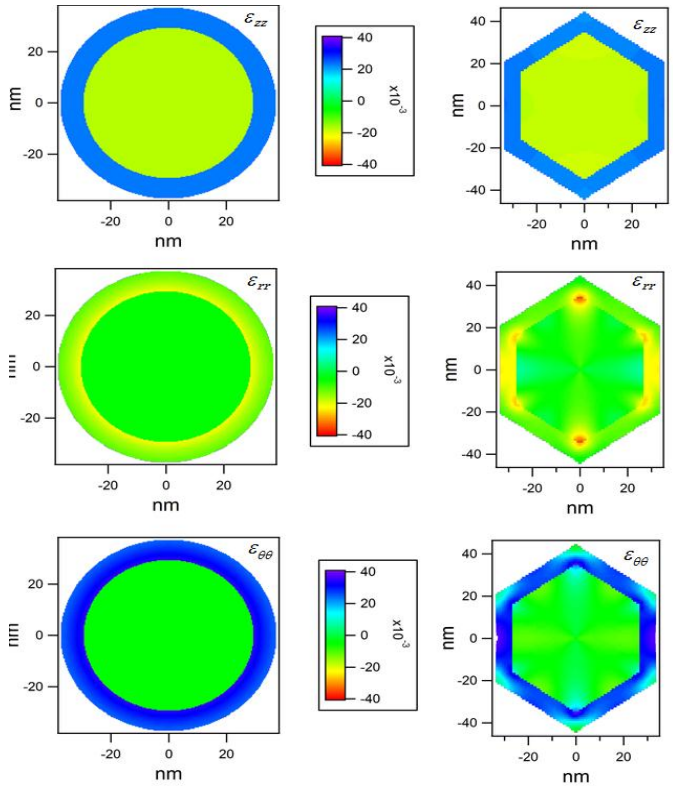

Figure A9a Comparison of the diagonal components of the strain tensor for a <011> Ge-Si core-shell nanowire with D_{core} = 53 nm and t_{shell} = 7.2 nm obtained with the analytical expressions in Eqs. (5.1)-(5.6) (left) and the numerical finite-element package ABAQUS (right).

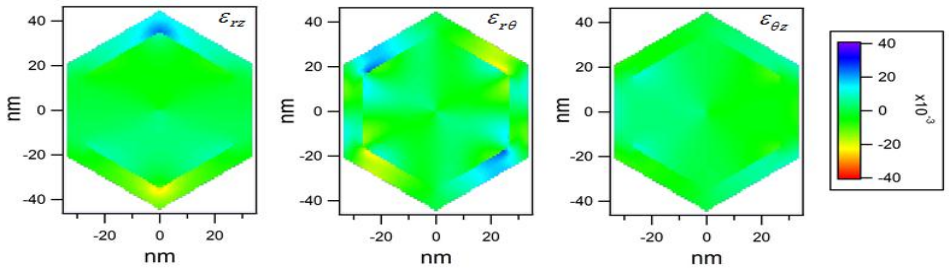

Figure A9b Off-diagonal components of the strain tensor for a <011> Ge-Si core-shell nanowire with D_{core} = 53 nm and t_{shell} = 7.2 nm obtained with the numerical finite-element package ABAQUS (right). The corresponding components in the analytical model of Eqs. (5.1)-(5.6) are exactly zero.

APPENDIX II

TABLE FOR COMPARISION OF STRAIN COMPONENTS OF ANALYTICAL AND NUMERICAL MODEL

Table AII.1 : Table to compare the diagonal strain components, $\varepsilon_{zz}^{\text{core}}$, $\varepsilon_{zz}^{\text{shell}}$, $\varepsilon_{rr}^{\text{core}}$ and $\varepsilon_{\theta\theta}^{\text{core}}$ computed from analytical and numerical model

Sample		$\varepsilon_{zz}^{\text{core}}$		$\varepsilon_{zz}^{\text{shell}}$		$\varepsilon_{rr}^{\text{core}}$		$\varepsilon_{\theta\theta}^{\text{core}}$	
D_{core} (nm)	t_{shell} (nm)	Analytical	Numerical	Analytical	Numerical	Analytical	Numerical	Analytical	Numerical
11	3.4	-0.027	-0.028	0.013	0.013	-0.008	-0.01	-0.008	-0.013
11	5	-0.031	-0.031	0.009	0.009	-0.01	-0.011	-0.01	-0.008
11	6.5	-0.033	-0.034	0.007	0.007	-0.010	-0.012	-0.010	-0.014
11	9	-0.035	-0.036	0.005	0.005	-0.011	-0.013	-0.011	-0.015
32	4.9	-0.019	-0.019	0.021	0.021	-0.005	-0.007	-0.005	-0.001
41	6.1	-0.018	-0.019	0.022	0.021	-0.006	-0.006	-0.006	-0.004
44	3.7	-0.012	-0.013	0.028	0.027	-0.004	-0.007	-0.004	-0.006
45	9.1	-0.022	-0.023	0.018	0.017	-0.007	-0.002	-0.007	-0.010
53	7.2	-0.017	-0.018	0.023	0.022	-0.005	-0.002	-0.005	-0.008

APPENDIX III

GRAPHS OF CORE RAMAN SPECTRA IN LL POLARIZATION

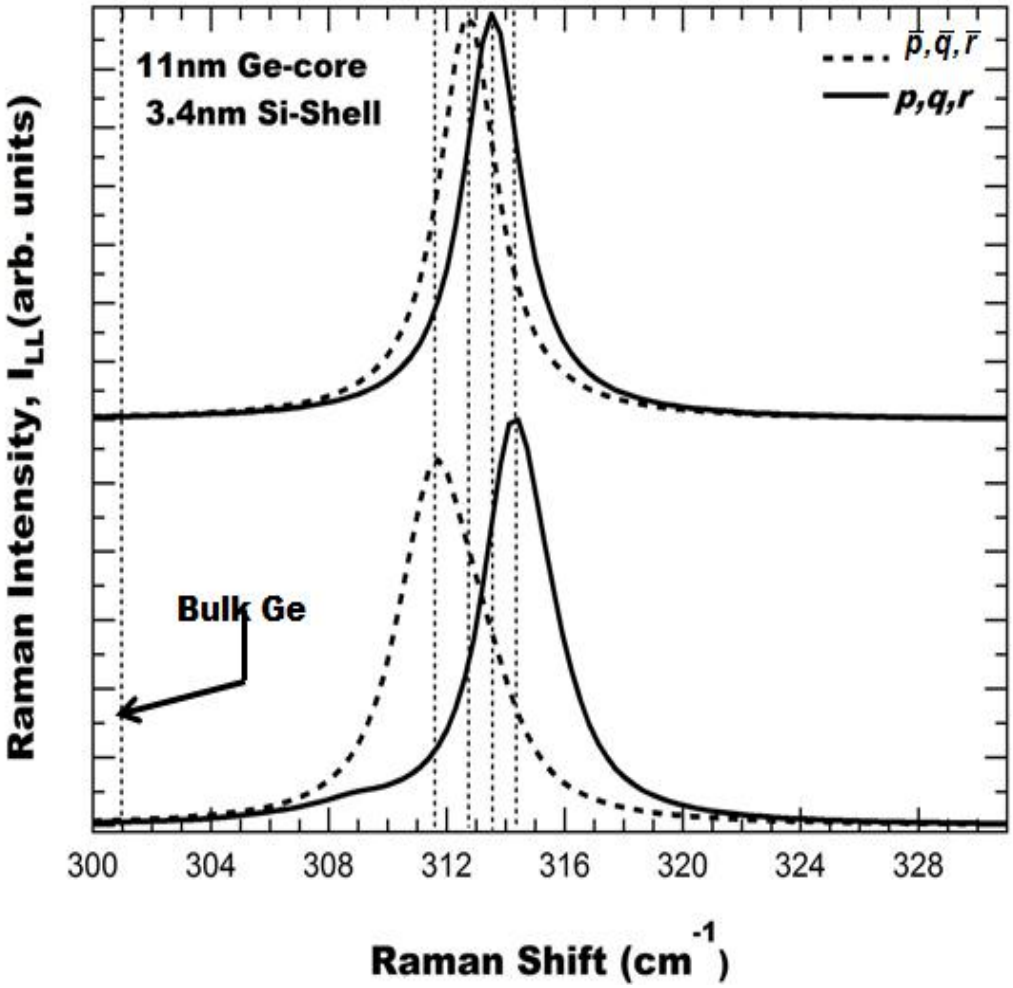

Figure A10 Calculated Raman spectra of the core region for a <011> Ge-Si core-shell nanowire with D_{core} = 11 nm and t_{shell} = 3.4 nm. Incident and scattered light polarizations are parallel to the nanowire axis. The top curves correspond to the analytical strain model with cylindrical geometry. The bottom curves correspond to the numerical strain calculation with realistic geometry. Solid lines were calculated using cubic symmetry *p,q, r* phonon deformation potential tensor components from Table 5.1. Dotted lines were calculated using the Voigt averaged tensor components from Eq.(5.6). All spectra are normalized to the same area. The vertical scale is the same in both panels. Darker regions give stronger contributions.

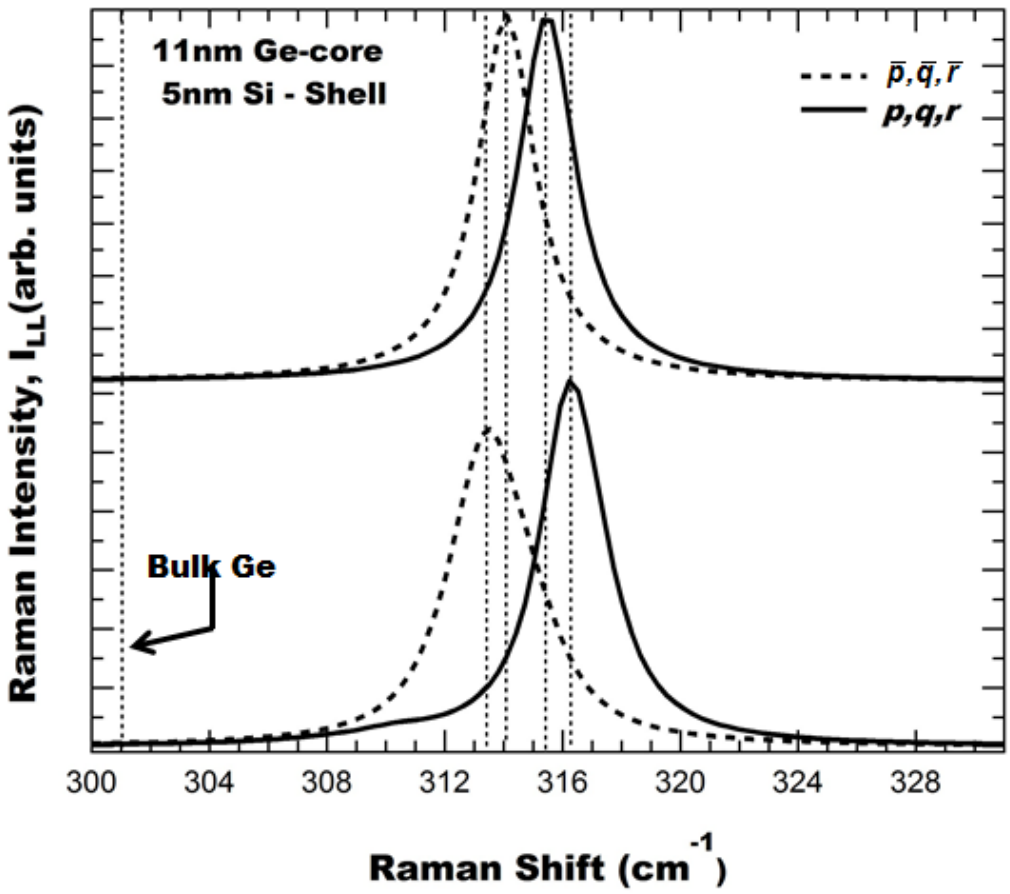

Figure A11 Calculated Raman spectra of the core region for a <011> Ge-Si core-shell nanowire with D_{core} = 11 nm and t_{shell} = 5.0 nm. Incident and scattered light polarizations are parallel to the nanowire axis. The top curves correspond to the analytical strain model with cylindrical geometry. The bottom curves correspond to the numerical strain calculation with realistic geometry. Solid lines were calculated using cubic symmetry *p,q, r* phonon deformation potential tensor components from Table 5.1. Dotted lines were calculated using the Voigt averaged tensor components from Eq.(5.6). All spectra are normalized to the same area. The vertical scale is the same in both panels. Darker regions give stronger contributions.

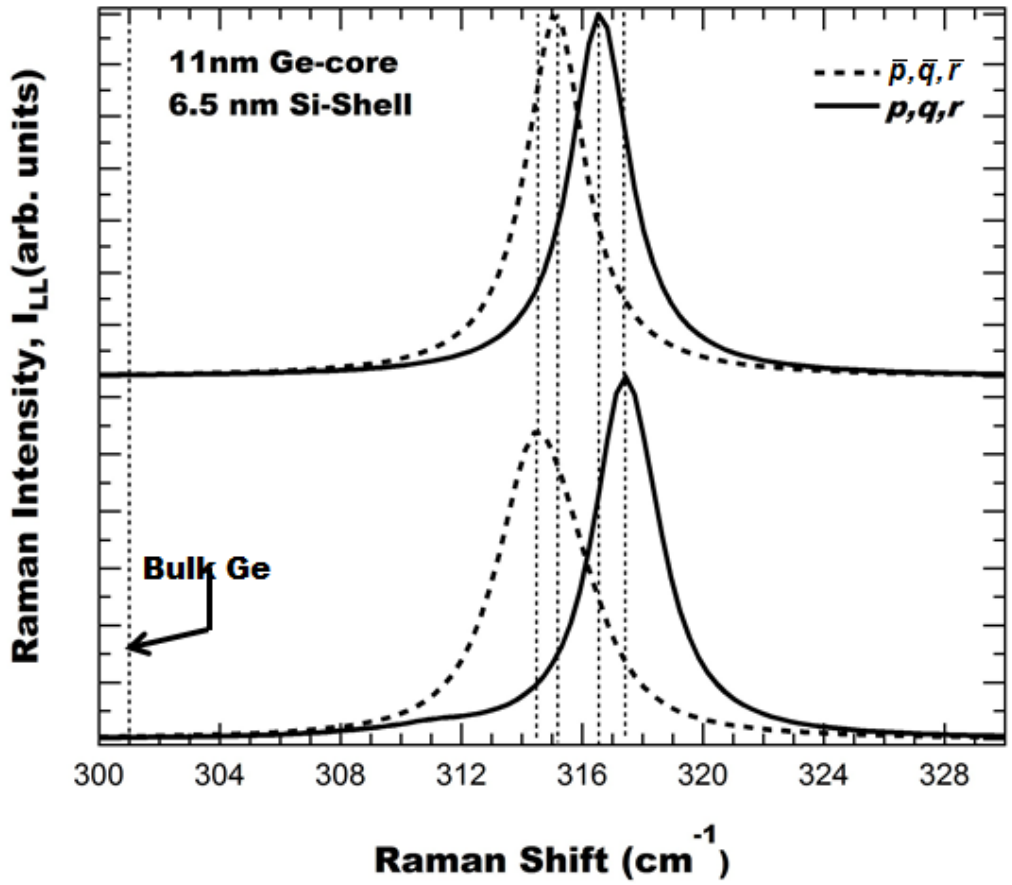

Figure A12 Calculated Raman spectra of the core region for a <011> Ge-Si core-shell nanowire with D_{core} = 11 nm and t_{shell} = 5.0 nm. Incident and scattered light polarizations are parallel to the nanowire axis. The top curves correspond to the analytical strain model with cylindrical geometry. The bottom curves correspond to the numerical strain calculation with realistic geometry. Solid lines were calculated using cubic symmetry *p,q, r* phonon deformation potential tensor components from Table 5.1. Dotted lines were calculated using the Voigt averaged tensor components from Eq.(5.6). All spectra are normalized to the same area. The vertical scale is the same in both panels. Darker regions give stronger contributions.

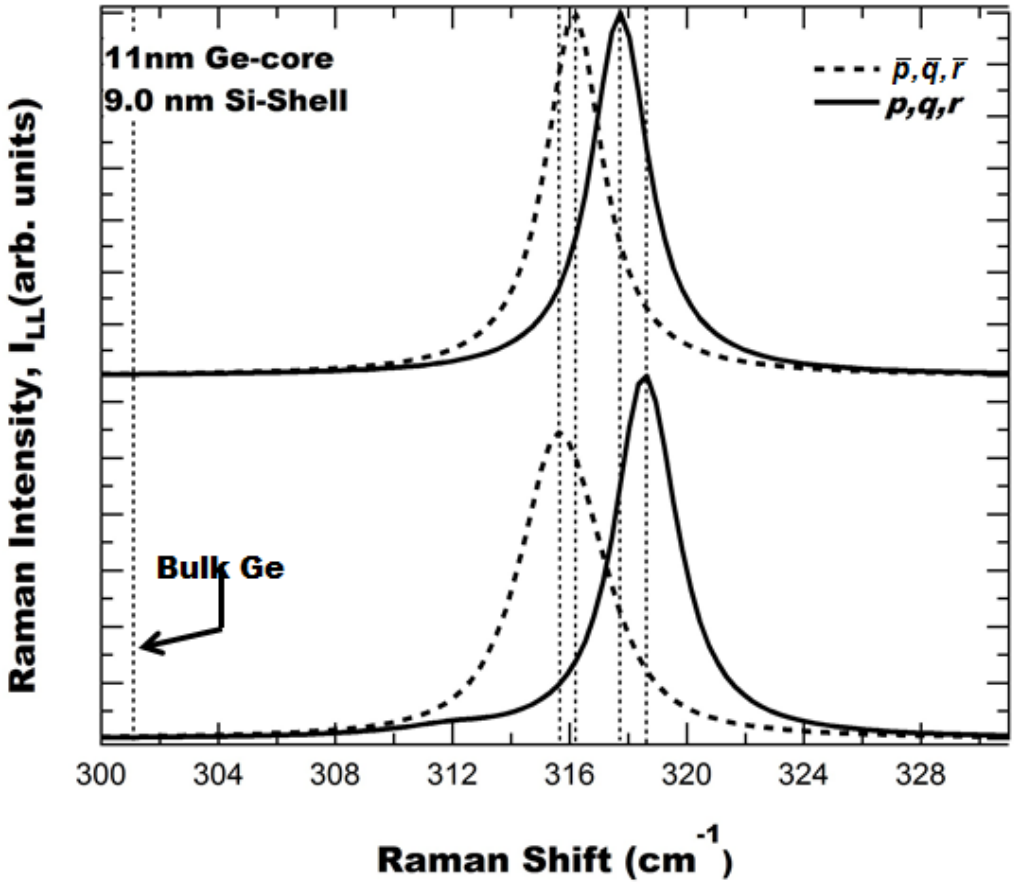

Figure A13 Calculated Raman spectra of the core region for a <011> Ge-Si core-shell nanowire with D_{core} = 11 nm and t_{shell} = 9.0 nm. Incident and scattered light polarizations are parallel to the nanowire axis. The top curves correspond to the analytical strain model with cylindrical geometry. The bottom curves correspond to the numerical strain calculation with realistic geometry. Solid lines were calculated using cubic symmetry *p,q, r* phonon deformation potential tensor components from Table 5.1. Dotted lines were calculated using the Voigt averaged tensor components from Eq. (5.6). All spectra are normalized to the same area. The vertical scale is the same in both panels. Darker regions give stronger contributions.

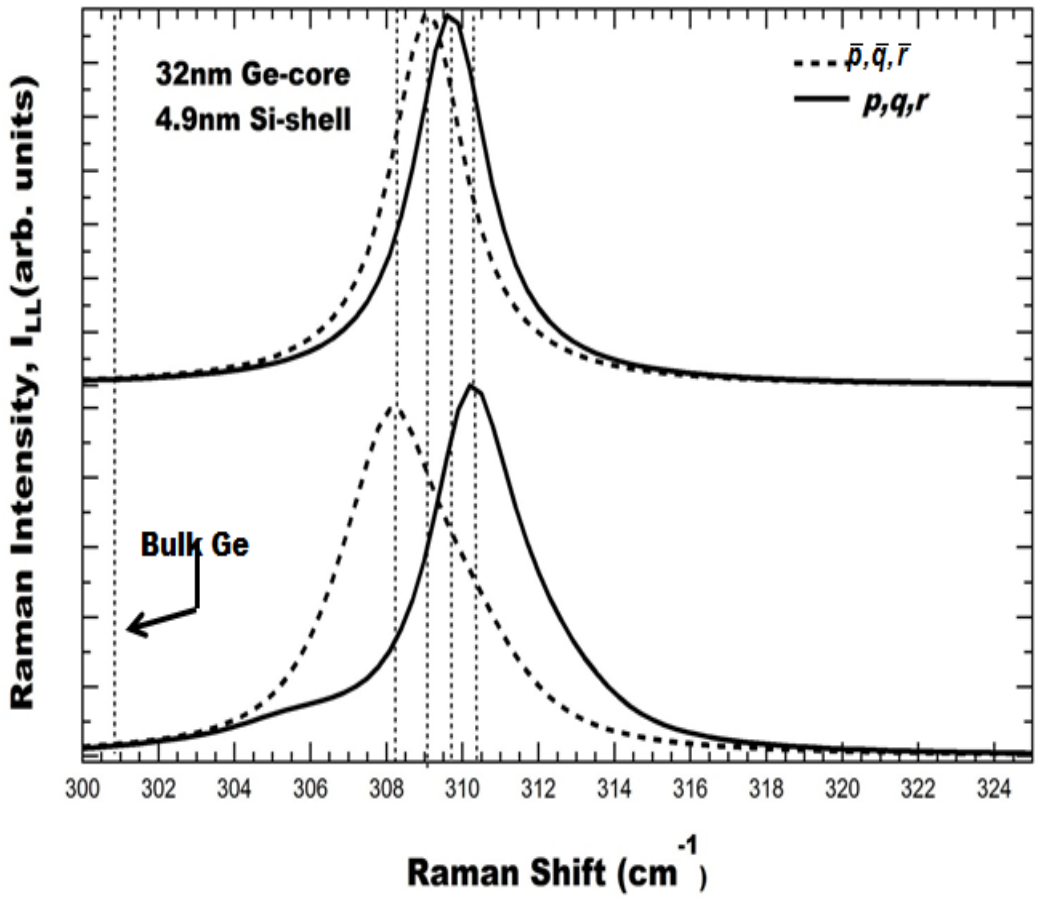

Figure A14 Calculated Raman spectra of the core region for a <011> Ge-Si core-shell nanowire with D_{core} = 32 nm and t_{shell} = 4.9 nm. Incident and scattered light polarizations are parallel to the nanowire axis. The top curves correspond to the analytical strain model with cylindrical geometry. The bottom curves correspond to the numerical strain calculation with realistic geometry. Solid lines were calculated using cubic symmetry *p,q, r* phonon deformation potential tensor components from Table 5.1. Dotted lines were calculated using the Voigt averaged tensor components from Eq. (5.6). All spectra are normalized to the same area. The vertical scale is the same in both panels. Darker regions give stronger contributions.

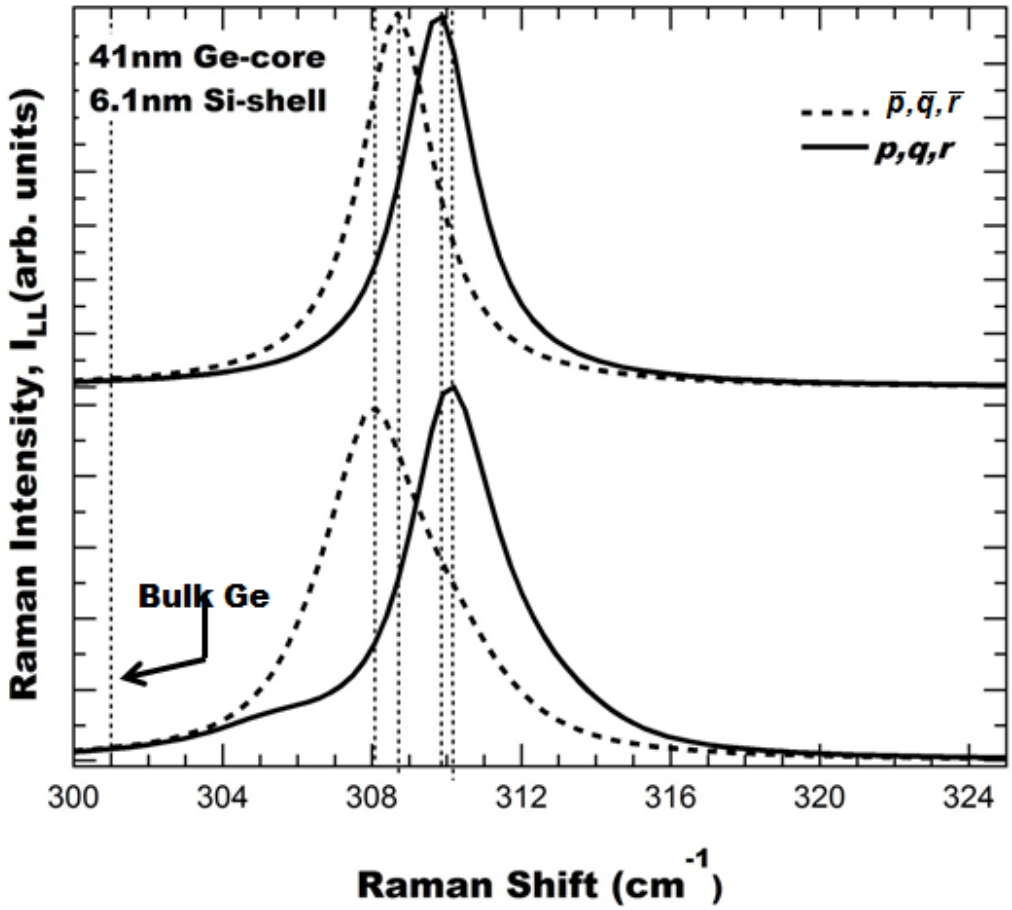

Figure A15 Calculated Raman spectra of the core region for a <011> Ge-Si core-shell nanowire with D_{core} = 41 nm and t_{shell} = 6.1 nm. Incident and scattered light polarizations are parallel to the nanowire axis. The top curves correspond to the analytical strain model with cylindrical geometry. The bottom curves correspond to the numerical strain calculation with realistic geometry. Solid lines were calculated using cubic symmetry *p,q, r* phonon deformation potential tensor components from Table 5.1. Dotted lines were calculated using the Voigt averaged tensor components from Eq. (5.6). All spectra are normalized to the same area. The vertical scale is the same in both panels. Darker regions give stronger contributions.

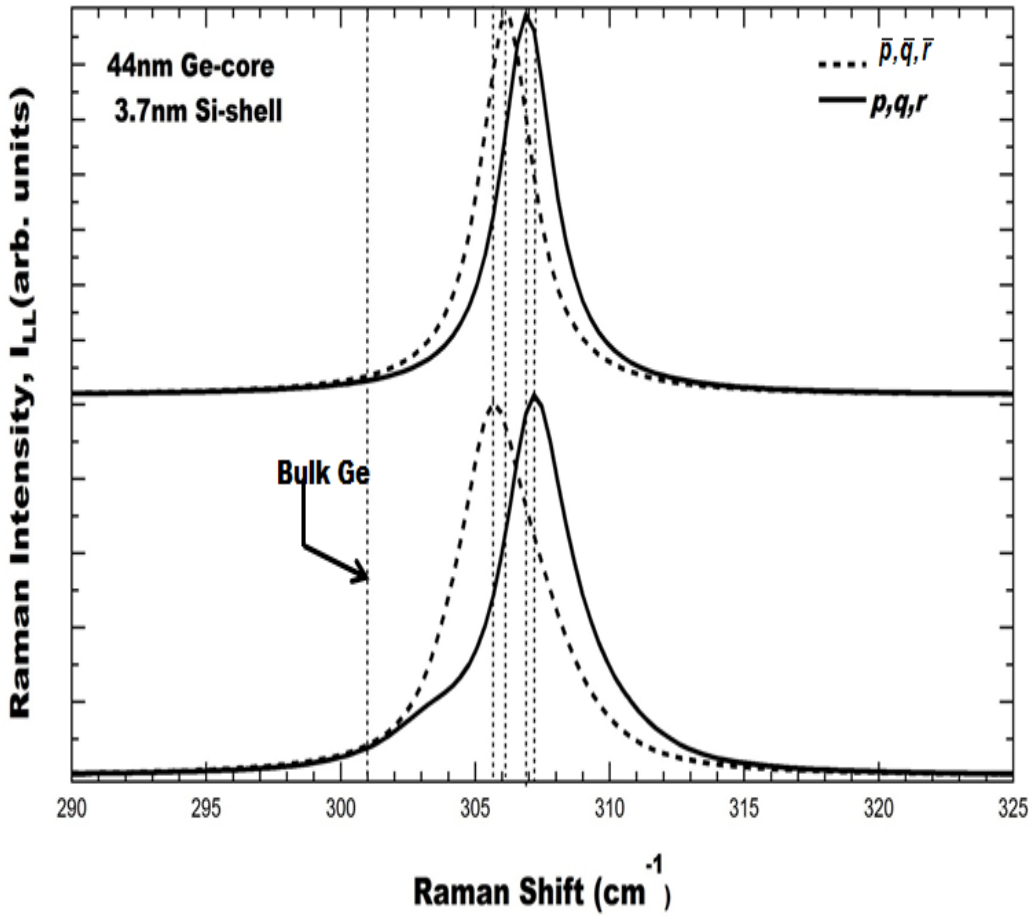

Figure A16 Calculated Raman spectra of the core region for a <011> Ge-Si core-shell nanowire with D_{core} = 44 nm and t_{shell} = 3.7 nm. Incident and scattered light polarizations are parallel to the nanowire axis. The top curves correspond to the analytical strain model with cylindrical geometry. The bottom curves correspond to the numerical strain calculation with realistic geometry. Solid lines were calculated using cubic symmetry *p,q, r* phonon deformation potential tensor components from Table 5.1. Dotted lines were calculated using the Voigt averaged tensor components from Eq. (5.6). All spectra are normalized to the same area. The vertical scale is the same in both panels. Darker regions give stronger contributions.

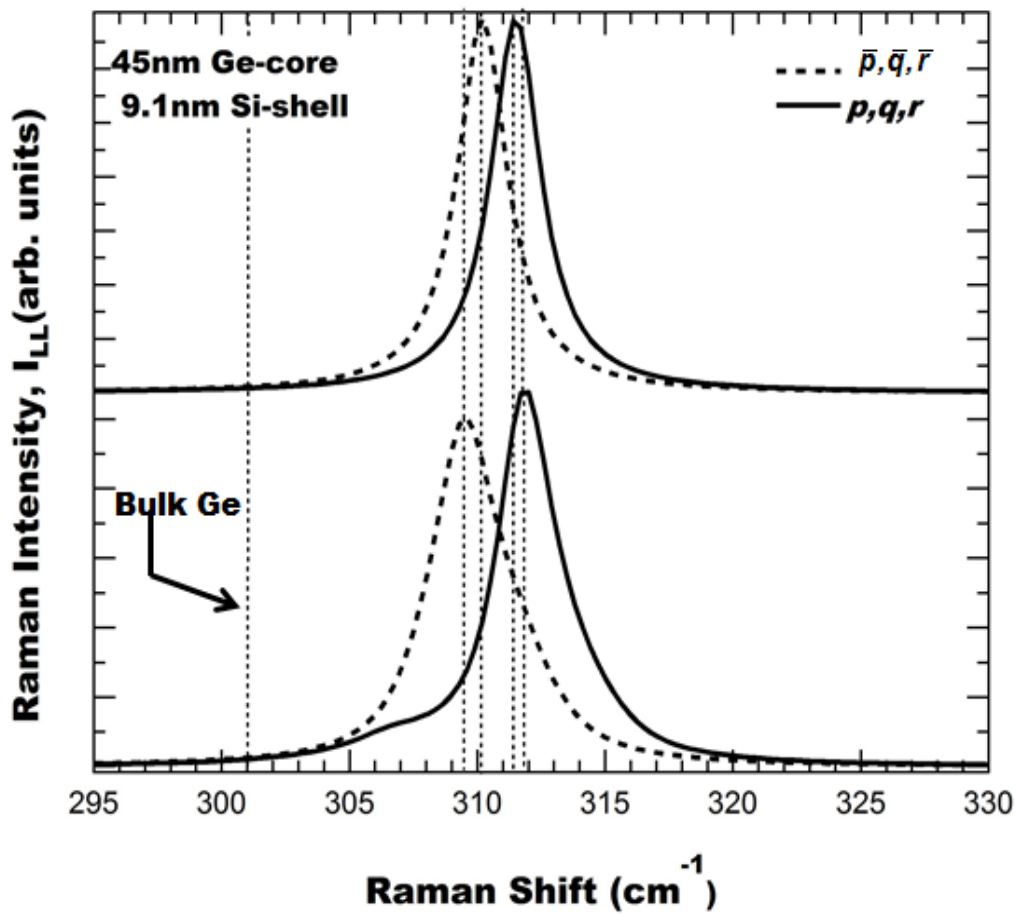

Figure A17 Calculated Raman spectra of the core region for a <011> Ge-Si core-shell nanowire with D_{core} = 45 nm and t_{shell} = 9.1 nm. Incident and scattered light polarizations are parallel to the nanowire axis. The top curves correspond to the analytical strain model with cylindrical geometry. The bottom curves correspond to the numerical strain calculation with realistic geometry. Solid lines were calculated using cubic symmetry *p,q, r* phonon deformation potential tensor components from Table 5.1. Dotted lines were calculated using the Voigt averaged tensor components from Eq. (5.6). All spectra are normalized to the same area. The vertical scale is the same in both panels. Darker regions give stronger contributions.

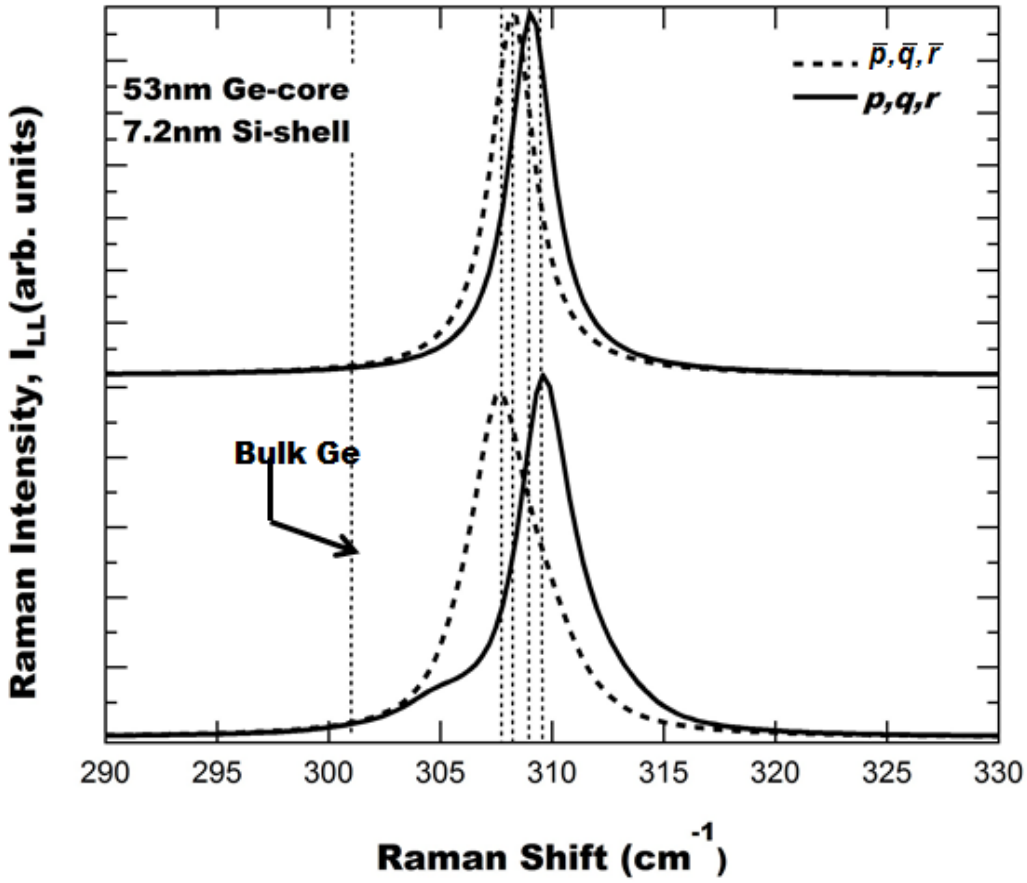

Figure A18 Calculated Raman spectra of the core region for a <011> Ge-Si core-shell nanowire with D_{core} = 53nm and t_{shell} = 7.2 nm. Incident and scattered light polarizations are parallel to the nanowire axis. The top curves correspond to the analytical strain model with cylindrical geometry. The bottom curves correspond to the numerical strain calculation with realistic geometry. Solid lines were calculated using cubic symmetry *p,q, r* phonon deformation potential tensor components from Table 5.1. Dotted lines were calculated using the Voigt averaged tensor components from Eq. (5.6). All spectra are normalized to the same area. The vertical scale is the same in both panels. Darker regions give stronger contributions.

APPENDIX IV

GRAPHS FOR CORE RAMAN SPECTRA IN LT_1,T_1T_2,ANDT_2T_2 POLARIZATIONS

Graphs of the Raman spectra of the core region of a <011> Ge-Si core-shell nanowires are shown in Appendix IV. Incident and scattered light polarizations are indicated in the three different panels. The convention is L = <011>, T_1 = <100>, and $T_2 = <01\bar{1}>$. The top curves correspond to the analytical strain model with cylindrical geometry. The bottom curves correspond to the numerical strain calculation with realistic geometry. Solid lines were calculated using cubic symmetry *p,q, r* phonon deformation potential tensor components from Table 5.1. Dotted lines were calculated using the Voigt averaged tensor components from Eq. (5.6). All spectra are normalized to the same area. The vertical scale is the same in all panels. The above instructions follow for all the graphs in Appendix IV.

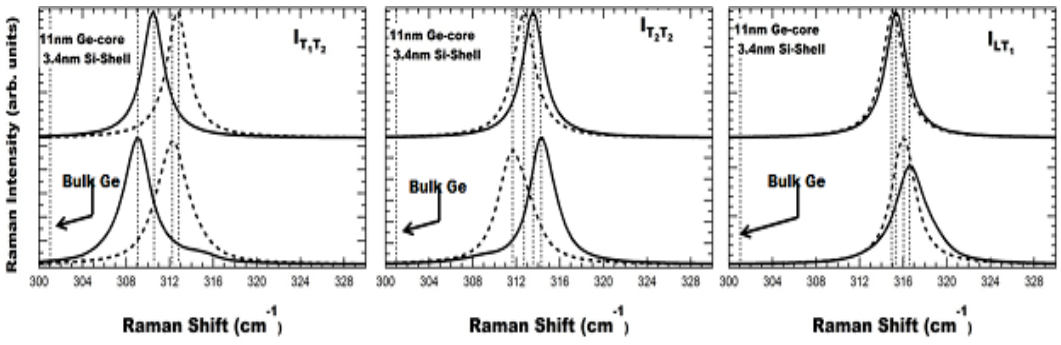

Figure A19 Calculated Raman spectra of the core region of a <011> Ge-Si core-shell nanowire with D_{core} = 11 nm and t_{shell} = 3.4 nm. Incident and scattered light polarizations are indicated in the three different panels. The convention is L = <011>, T_1 = <100>, and $T_2 = <01\bar{1}>$.

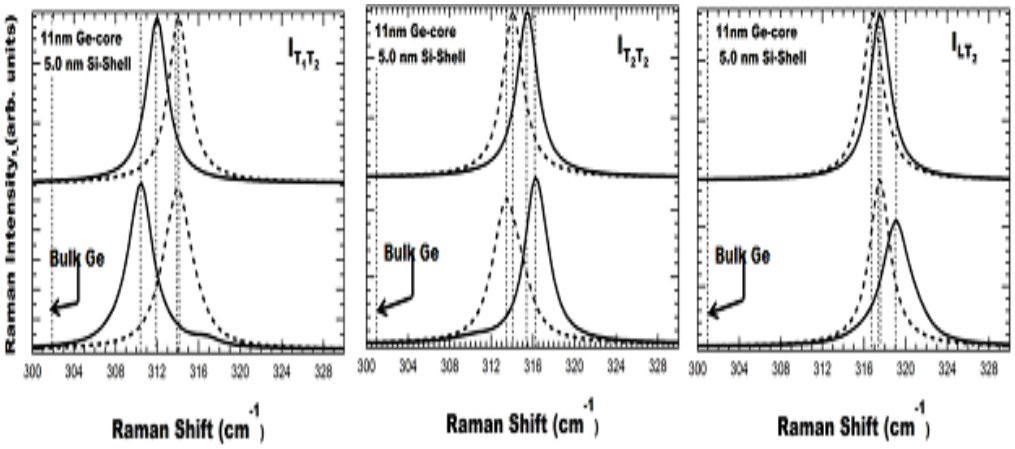

Figure A20 Calculated Raman spectra of the core region of a <011> Ge-Si core-shell nanowire with D_{core} = 11 nm and t_{shell} = 5 nm. Incident and scattered light polarizations are indicated in the three different panels. The convention is L = <011>, T_1 = <100>, and $T_2 = < 01\bar{1} >$.

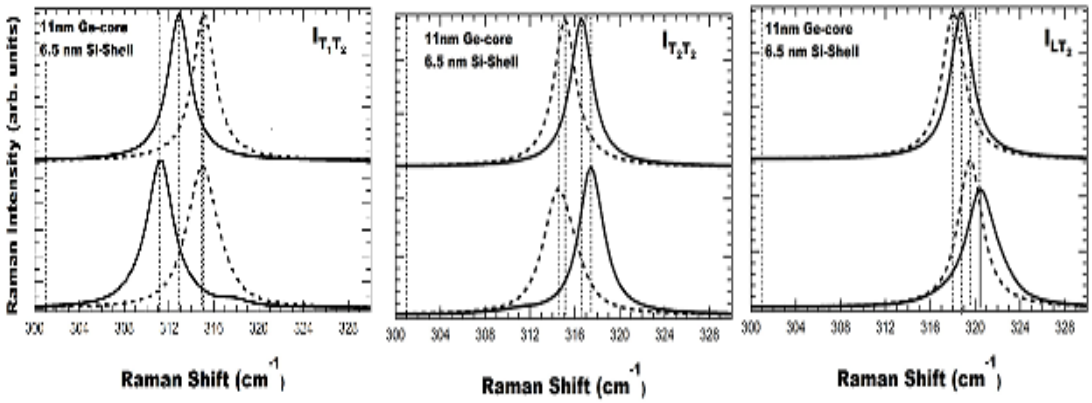

Figure A21 Calculated Raman spectra of the core region of a <011> Ge-Si core-shell nanowire with D_{core} = 11 nm and t_{shell} = 6.5 nm. Incident and scattered light polarizations are indicated in the three different panels. The convention is L = <011>, T_1 = <100>, and $T_2 = < 01\bar{1} >$.

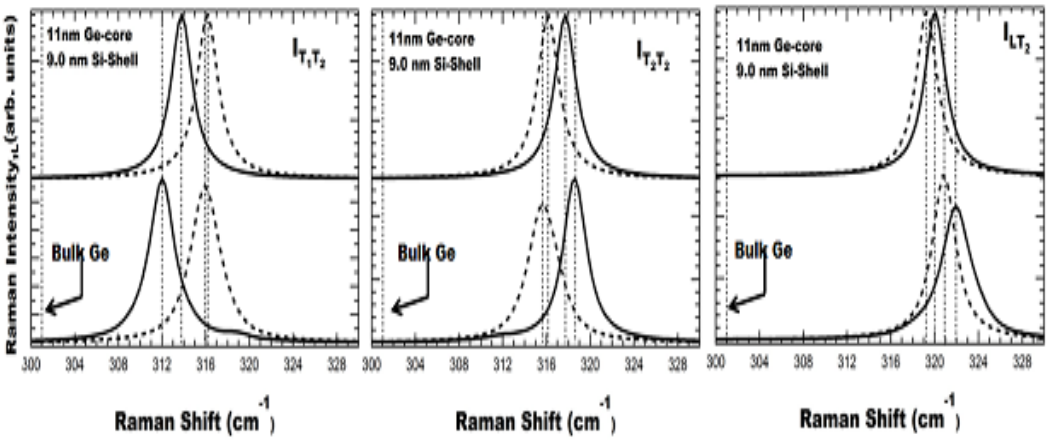

Figure A22 Calculated Raman spectra of the core region of a <011> Ge-Si core-shell nanowire with D_{core} = 11 nm and t_{shell} = 9 nm. Incident and scattered light polarizations are indicated in the three different panels. The convention is L = <011>, T_1 = <100>, and $T_2 = <01\bar{1}>$.

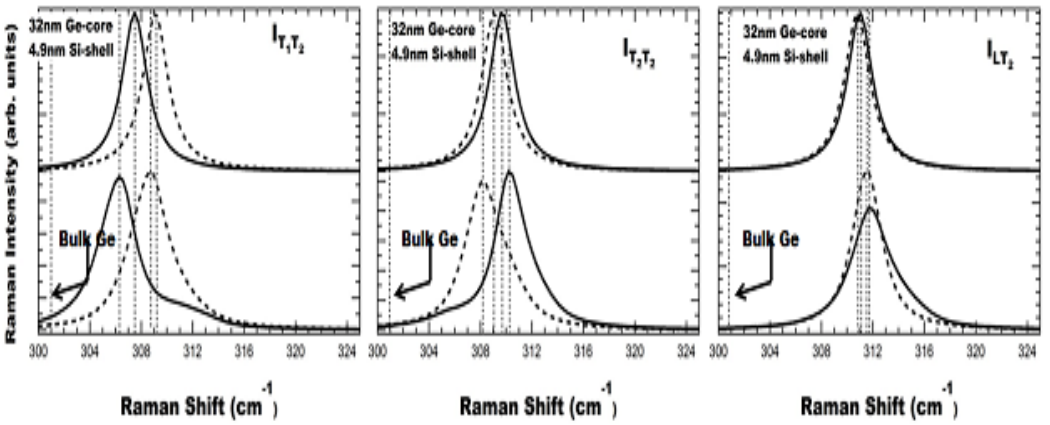

Figure A23 Calculated Raman spectra of the core region of a <011> Ge-Si core-shell nanowire with D_{core} = 32 nm and t_{shell} = 4.9 nm. Incident and scattered light polarizations are indicated in the three different panels. The convention is L = <011>, T_1 = <100>, and $T_2 = <01\bar{1}>$.

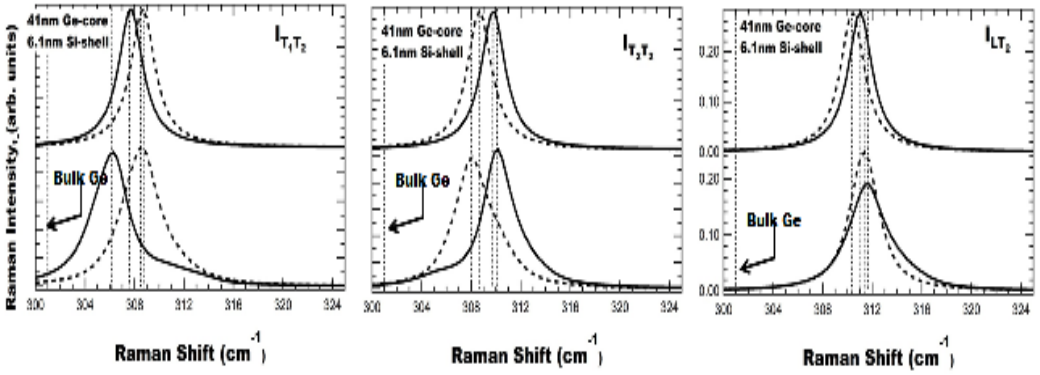

Figure A24 Calculated Raman spectra of the core region of a <011> Ge-Si core-shell nanowire with D_{core} = 41 nm and t_{shell} = 6.1 nm. Incident and scattered light polarizations are indicated in the three different panels. The convention is L = <011>, T_1 = <100>, and $T_2 = <01\bar{1}>$.

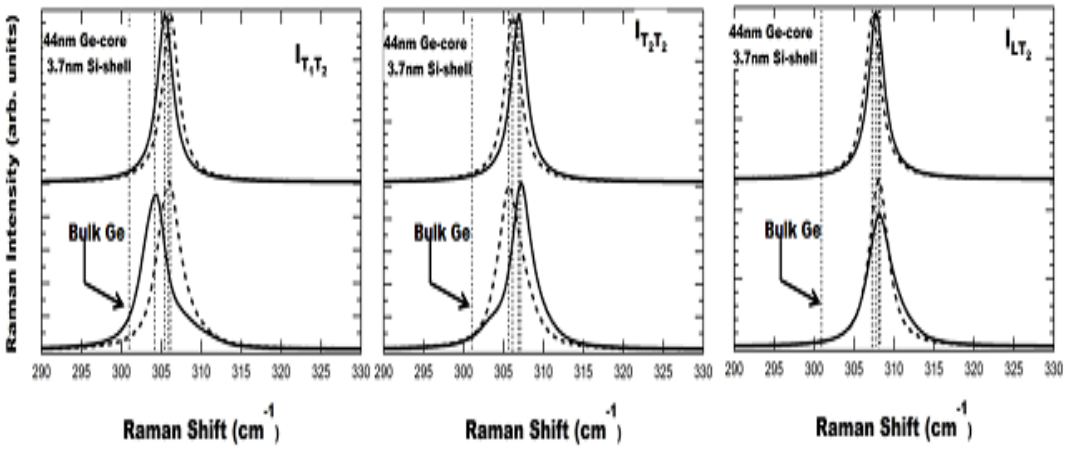

Figure A25 Calculated Raman spectra of the core region of a <011> Ge-Si core-shell nanowire with D_{core} = 44 nm and t_{shell} = 3.7 nm. Incident and scattered light polarizations are indicated in the three different panels. The convention is L = <011>, T_1 = <100>, and $T_2 = <01\bar{1}>$.

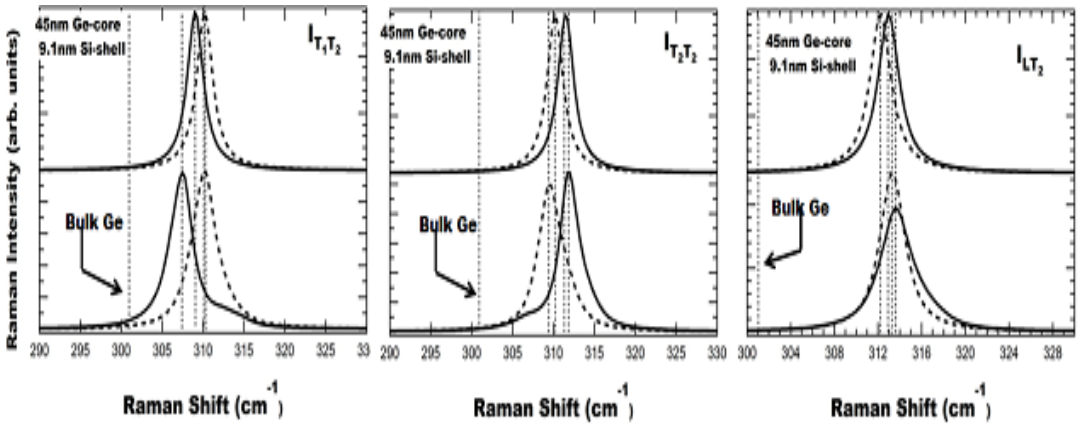

Figure A26 Calculated Raman spectra of the core region of a <011> Ge-Si core-shell nanowire with D_{core} = 45 nm and t_{shell} = 9.1 nm. Incident and scattered light polarizations are indicated in the three different panels. The convention is L = <011>, T_1 = <100>, and $T_2 = < 01\bar{1} >$.

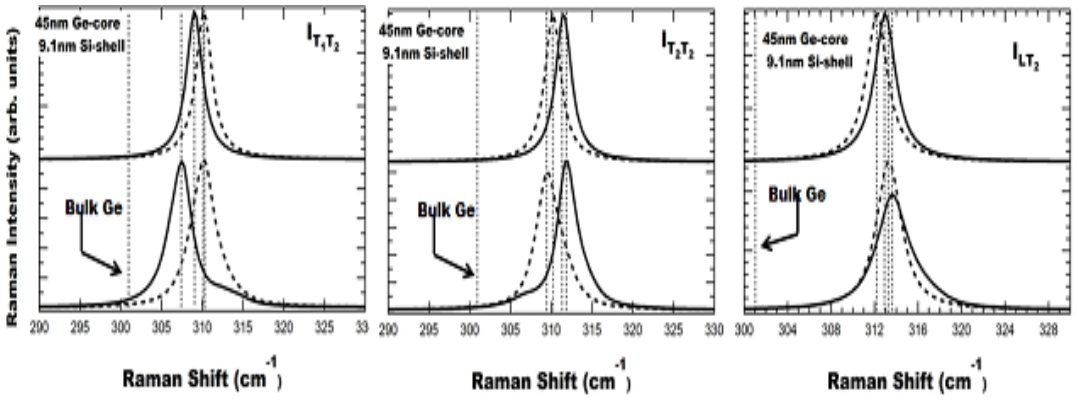

Figure A27 Calculated Raman spectra of the core region of a <011> Ge-Si core-shell nanowire with D_{core} = 53 nm and t_{shell} = 7.2 nm. Incident and scattered light polarizations are indicated in the three different panels. The convention is L = <011>, T_1 = <100>, and $T_2 = < 01\bar{1} >$.

APPENDIX V

GRAPHS FOR SHELL RAMAN SPECTRA IN 'LL' POLARIZATION

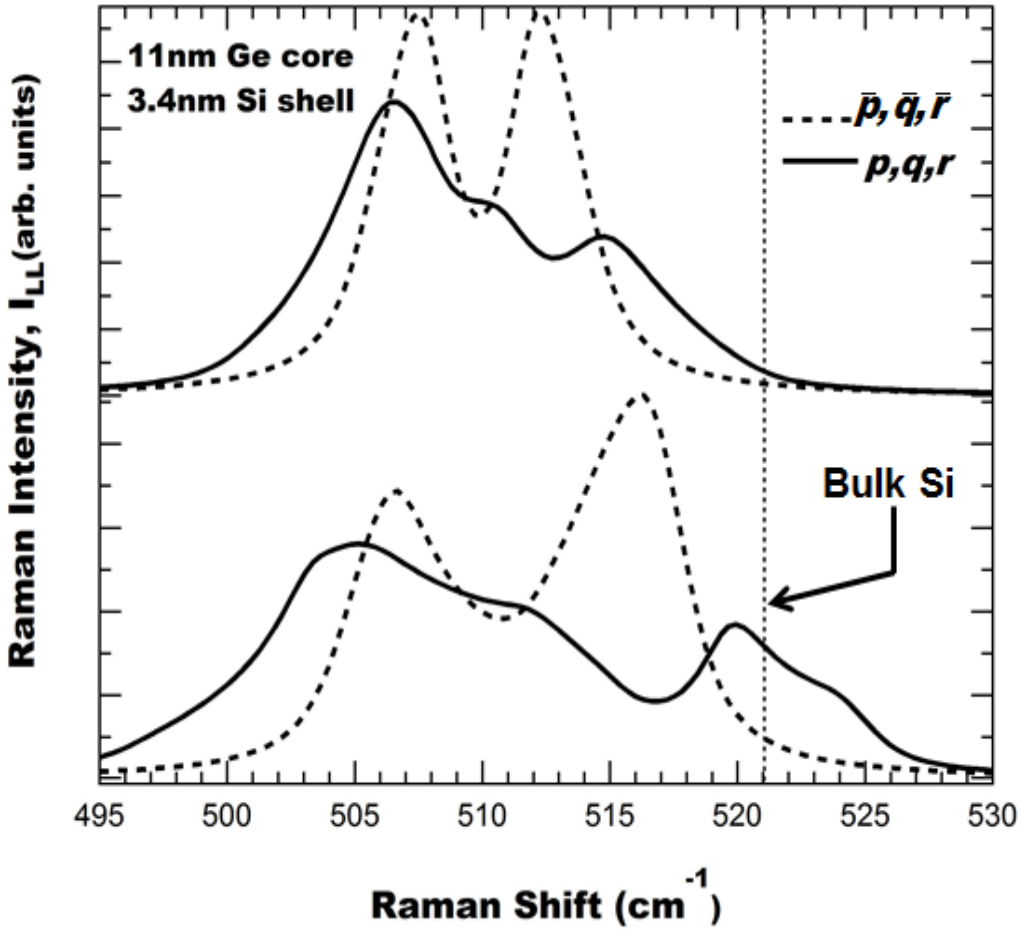

Figure A28 Calculated Raman spectra of the shell region of a <011> Ge-Si core-shell nanowire with D_{core} = 11 nm and t_{shell} = 3.4 nm, for incident and scattered light polarizations parallel to the nanowire axis. The top curves correspond to the analytical strain model with cylindrical geometry. The bottom curves correspond to the numerical strain calculation with realistic geometry. The spectra were calculated using either the full cubic p,q,r for Si from Table 5.1 (solid lines) or the Si Voigt-averaged tensor components from Eq. (5.6) (dotted lines). The latter are the same as in Fig. 5.4 and are shown here for easier comparison. All spectra are normalized to the same area. The vertical scale is the same in all panels. The vertical dotted line is the position of the Raman peak from bulk Si.

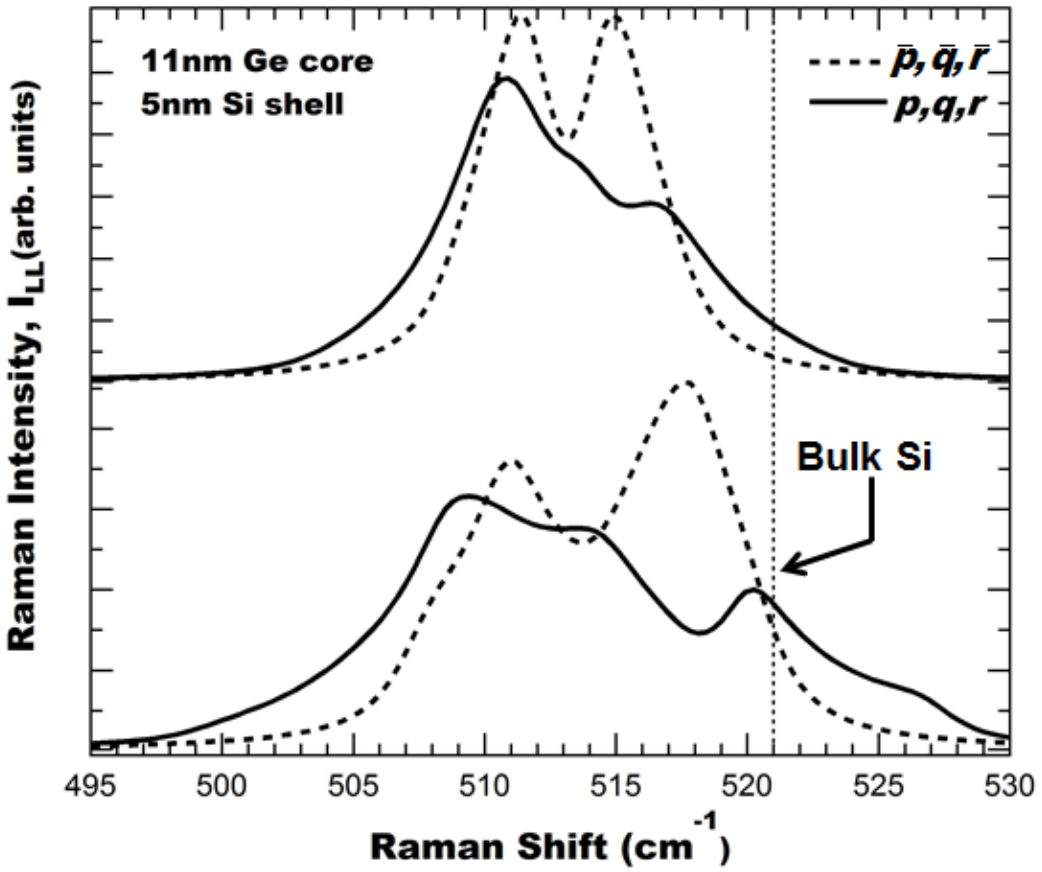

Figure A29 Calculated Raman spectra of the shell region of a <011> Ge-Si core-shell nanowire with D_{core} = 11 nm and t_{shell} = 5.0 nm, for incident and scattered light polarizations parallel to the nanowire axis. The top curves correspond to the analytical strain model with cylindrical geometry. The bottom curves correspond to the numerical strain calculation with realistic geometry. The spectra were calculated using either the full cubic p,q,r for Si from Table 5.1 (solid lines) or the Si Voigt-averaged tensor components from Eq. (5.6) (dotted lines). The latter are the same as in Fig. 5.4 and are shown here for easier comparison. All spectra are normalized to the same area. The vertical scale is the same in all panels. The vertical dotted line is the position of the Raman peak from bulk Si.

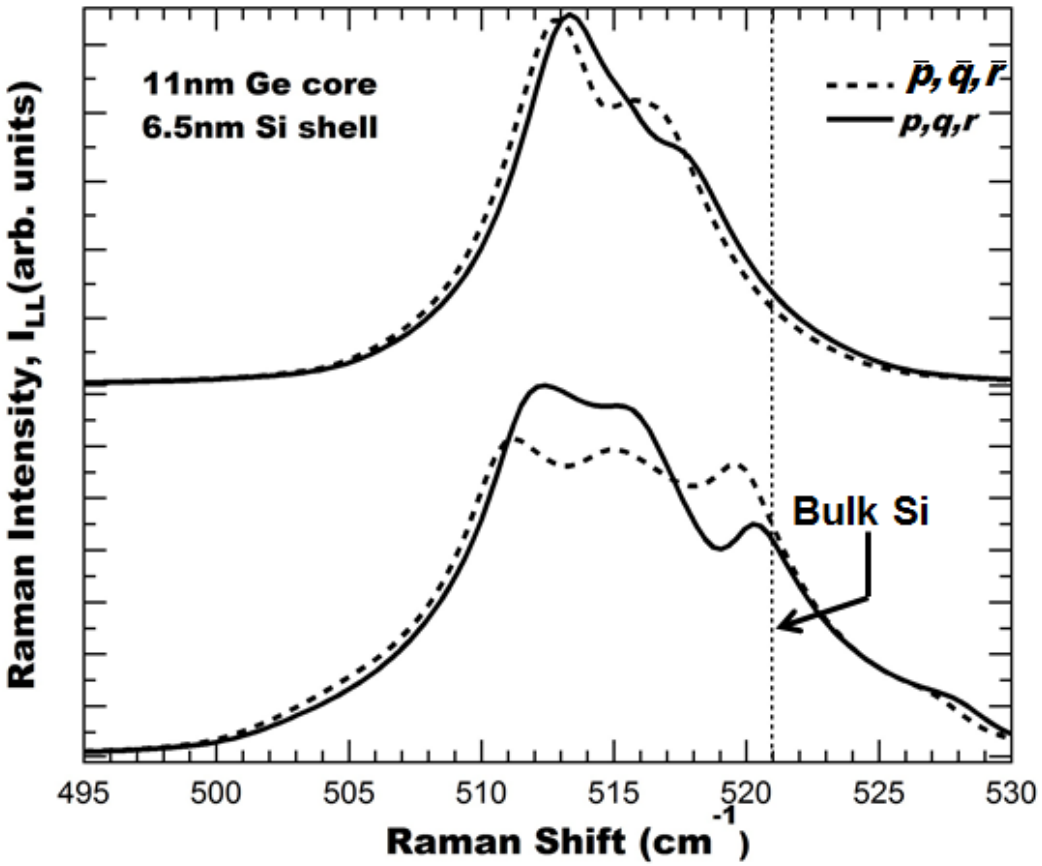

Figure A30 Calculated Raman spectra of the shell region of a <011> Ge-Si core-shell nanowire with D_{core} = 11 nm and t_{shell} = 6.5 nm, for incident and scattered light polarizations parallel to the nanowire axis. The top curves correspond to the analytical strain model with cylindrical geometry. The bottom curves correspond to the numerical strain calculation with realistic geometry. The spectra were calculated using either the full cubic *p,q, r* for Si from Table 5.1 (solid lines) or the Si Voigt-averaged tensor components from Eq. (5.6) (dotted lines). The latter are the same as in Fig. 5.4 and are shown here for easier comparison. All spectra are normalized to the same area. The vertical scale is the same in all panels. The vertical dotted line is the position of the Raman peak from bulk Si.

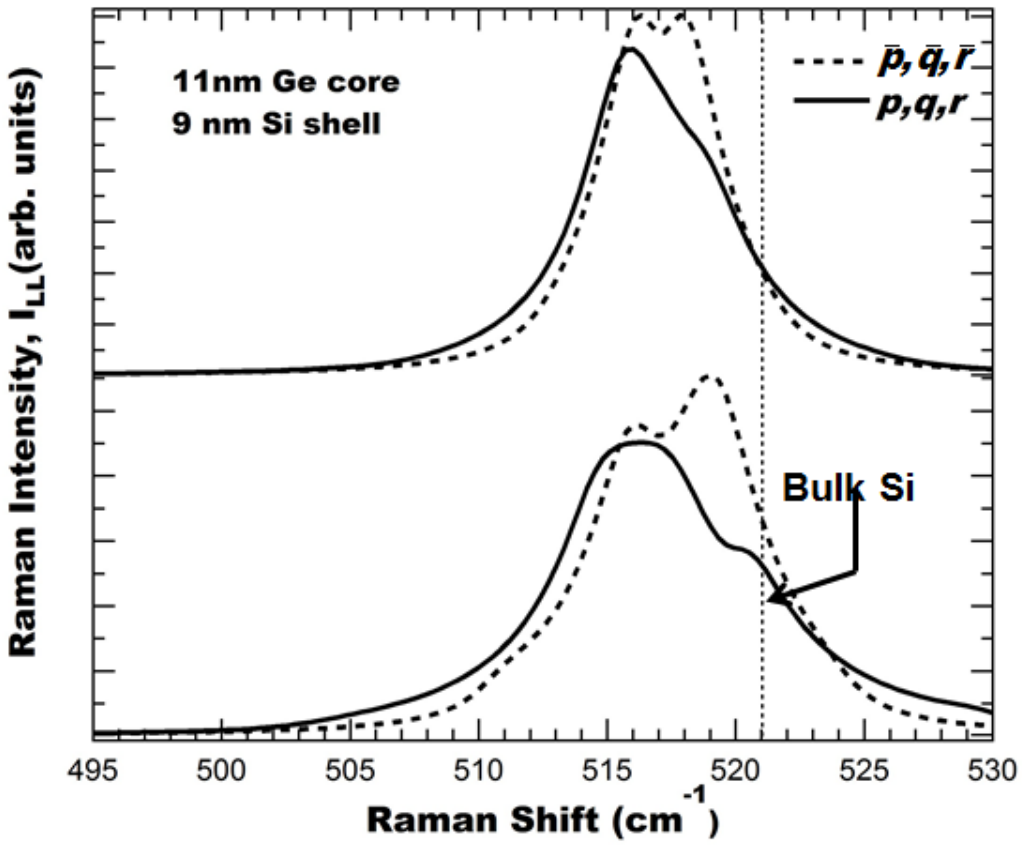

Figure A31 Calculated Raman spectra of the shell region of a <011> Ge-Si core-shell nanowire with D_{core} = 11 nm and t_{shell} = 9.0 nm, for incident and scattered light polarizations parallel to the nanowire axis. The top curves correspond to the analytical strain model with cylindrical geometry. The bottom curves correspond to the numerical strain calculation with realistic geometry. The spectra were calculated using either the full cubic p,q,r for Si from Table 5.1 (solid lines) or the Si Voigt-averaged tensor components from Eq. (5.6) (dotted lines). The latter are the same as in Fig. 5.4 and are shown here for easier comparison. All spectra are normalized to the same area. The vertical scale is the same in all panels. The vertical dotted line is the position of the Raman peak from bulk Si.

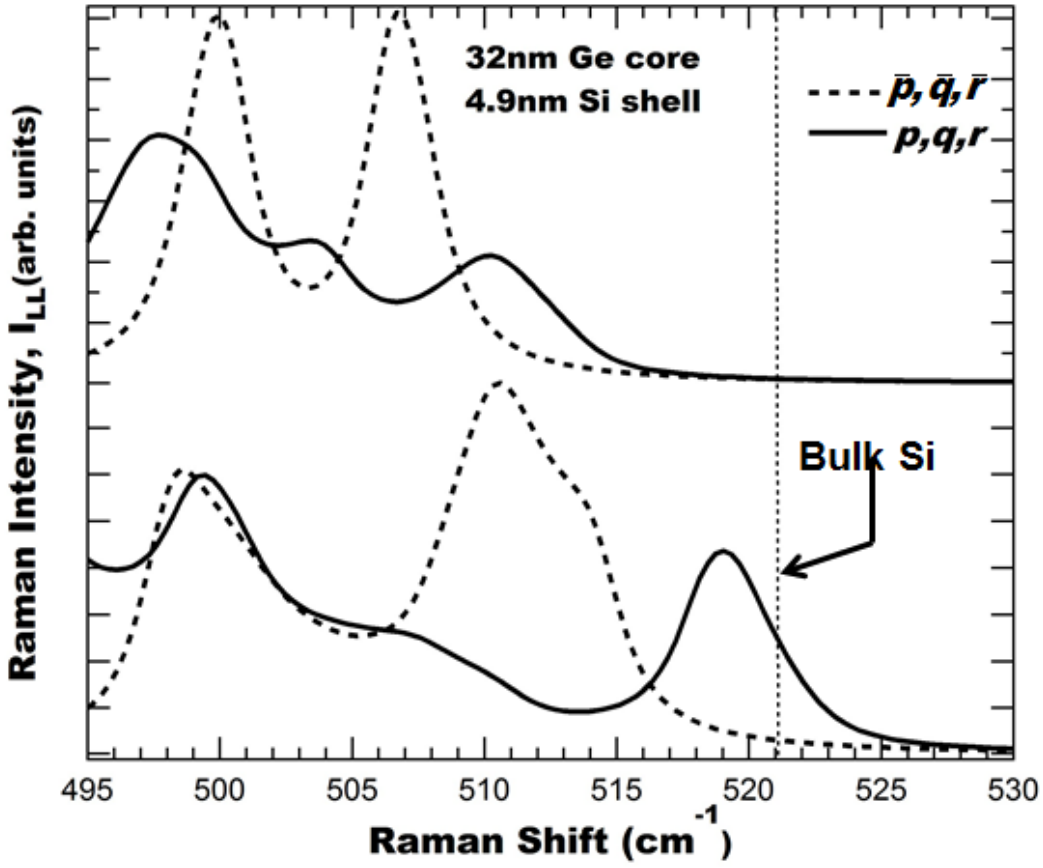

Figure A32 Calculated Raman spectra of the shell region of a <011> Ge-Si core-shell nanowire with D_{core} = 32 nm and t_{shell} = 4.9 nm, for incident and scattered light polarizations parallel to the nanowire axis. The top curves correspond to the analytical strain model with cylindrical geometry. The bottom curves correspond to the numerical strain calculation with realistic geometry. The spectra were calculated using either the full cubic *p,q, r* for Si from Table 5.1 (solid lines) or the Si Voigt-averaged tensor components from Eq. (5.6) (dotted lines). The latter are the same as in Fig. 5.4 and are shown here for easier comparison. All spectra are normalized to the same area. The vertical scale is the same in all panels. The vertical dotted line is the position of the Raman peak from bulk Si.

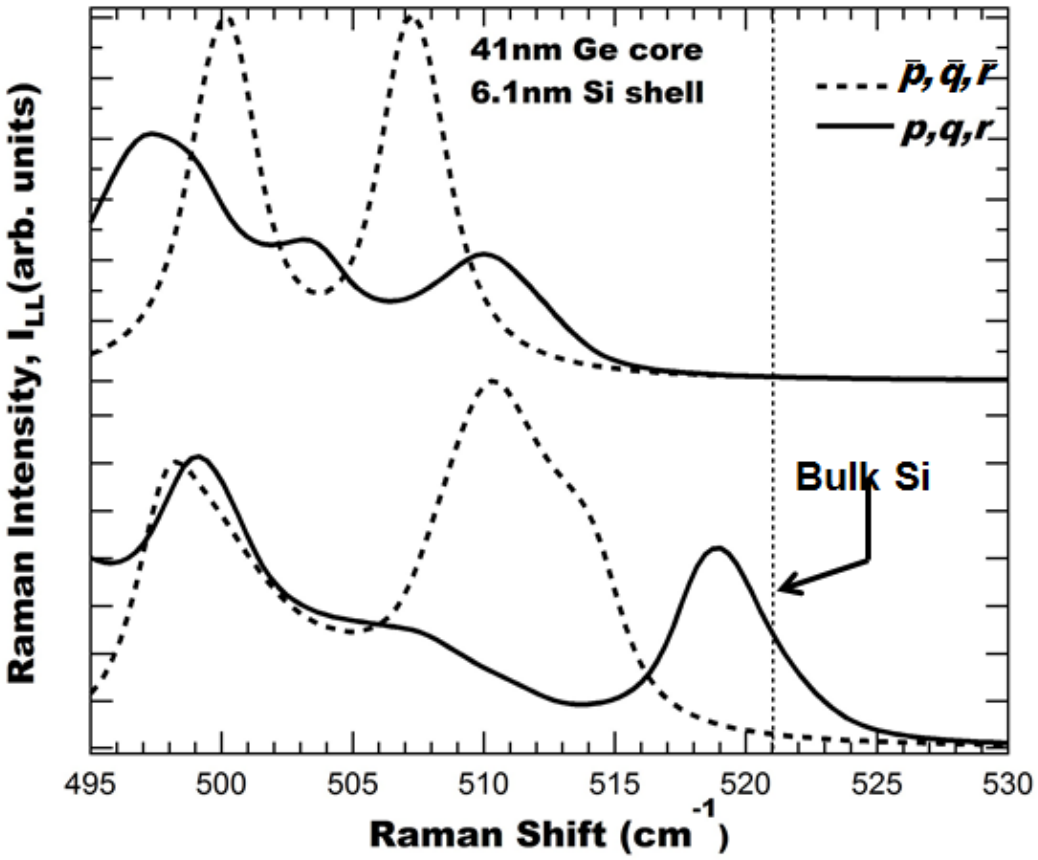

Figure A33 Calculated Raman spectra of the shell region of a <011> Ge-Si core-shell nanowire with D_{core} = 41 nm and t_{shell} = 6.1 nm, for incident and scattered light polarizations parallel to the nanowire axis. The top curves correspond to the analytical strain model with cylindrical geometry. The bottom curves correspond to the numerical strain calculation with realistic geometry. The spectra were calculated using either the full cubic p,q,r for Si from Table 5.1 (solid lines) or the Si Voigt-averaged tensor components from Eq. (5.6) (dotted lines). The latter are the same as in Fig. 5.4 and are shown here for easier comparison. All spectra are normalized to the same area. The vertical scale is the same in all panels. The vertical dotted line is the position of the Raman peak from bulk Si.

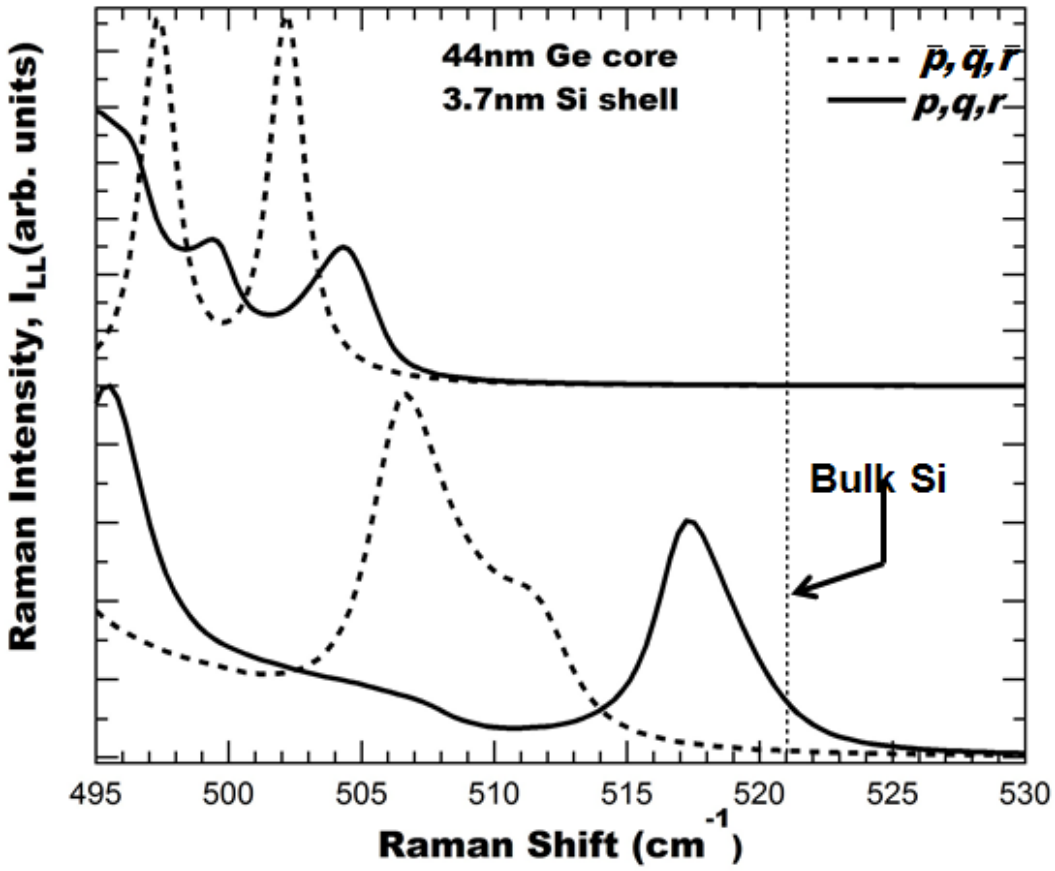

Figure A34 Calculated Raman spectra of the shell region of a <011> Ge-Si core-shell nanowire with D_{core} = 44 nm and t_{shell} = 3.7 nm, for incident and scattered light polarizations parallel to the nanowire axis. The top curves correspond to the analytical strain model with cylindrical geometry. The bottom curves correspond to the numerical strain calculation with realistic geometry. The spectra were calculated using either the full cubic p, q, r for Si from Table 5.1 (solid lines) or the Si Voigt-averaged tensor components from Eq. (5.6) (dotted lines). The latter are the same as in Fig. 5.4 and are shown here for easier comparison. All spectra are normalized to the same area. The vertical scale is the same in all panels. The vertical dotted line is the position of the Raman peak from bulk Si.

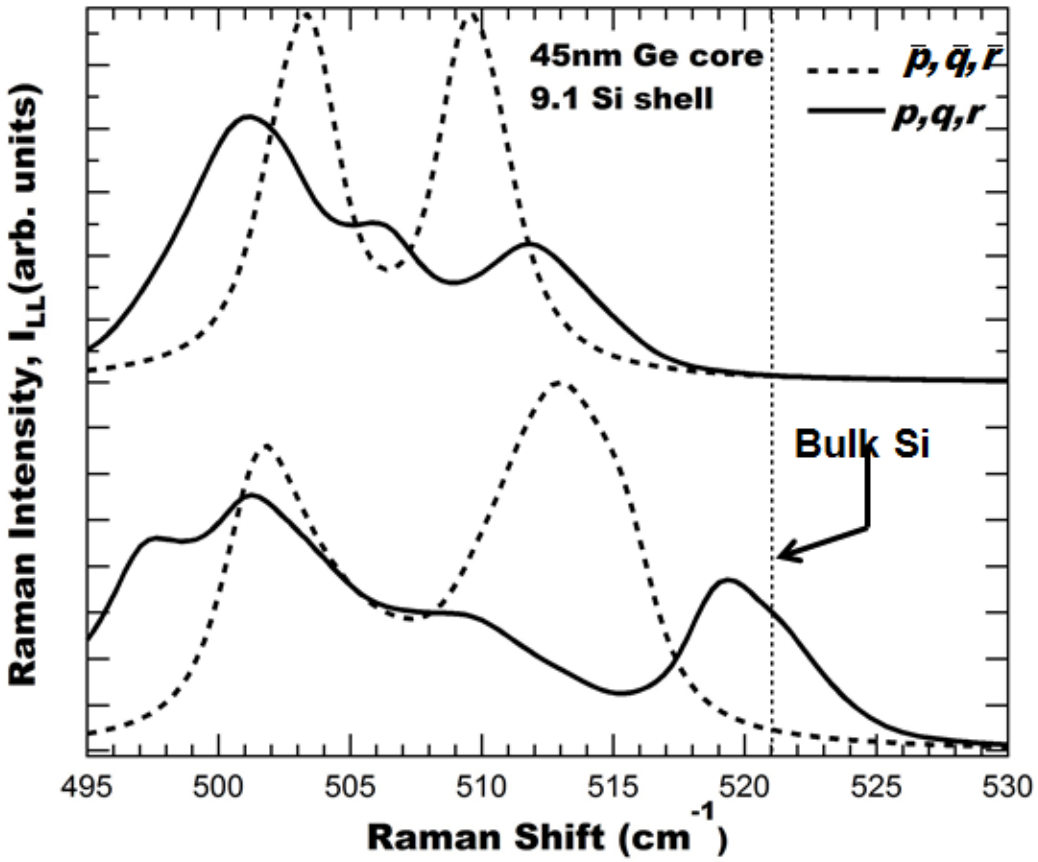

Figure A35 Calculated Raman spectra of the shell region of a <011> Ge-Si core-shell nanowire with D_{core} = 45 nm and t_{shell} = 9.1 nm, for incident and scattered light polarizations parallel to the nanowire axis. The top curves correspond to the analytical strain model with cylindrical geometry. The bottom curves correspond to the numerical strain calculation with realistic geometry. The spectra were calculated using either the full cubic p,q,r for Si from Table 5.1 (solid lines) or the Si Voigt-averaged tensor components from Eq. (5.6) (dotted lines). The latter are the same as in Fig. 5.4 and are shown here for easier comparison. All spectra are normalized to the same area. The vertical scale is the same in all panels. The vertical dotted line is the position of the Raman peak from bulk Si.

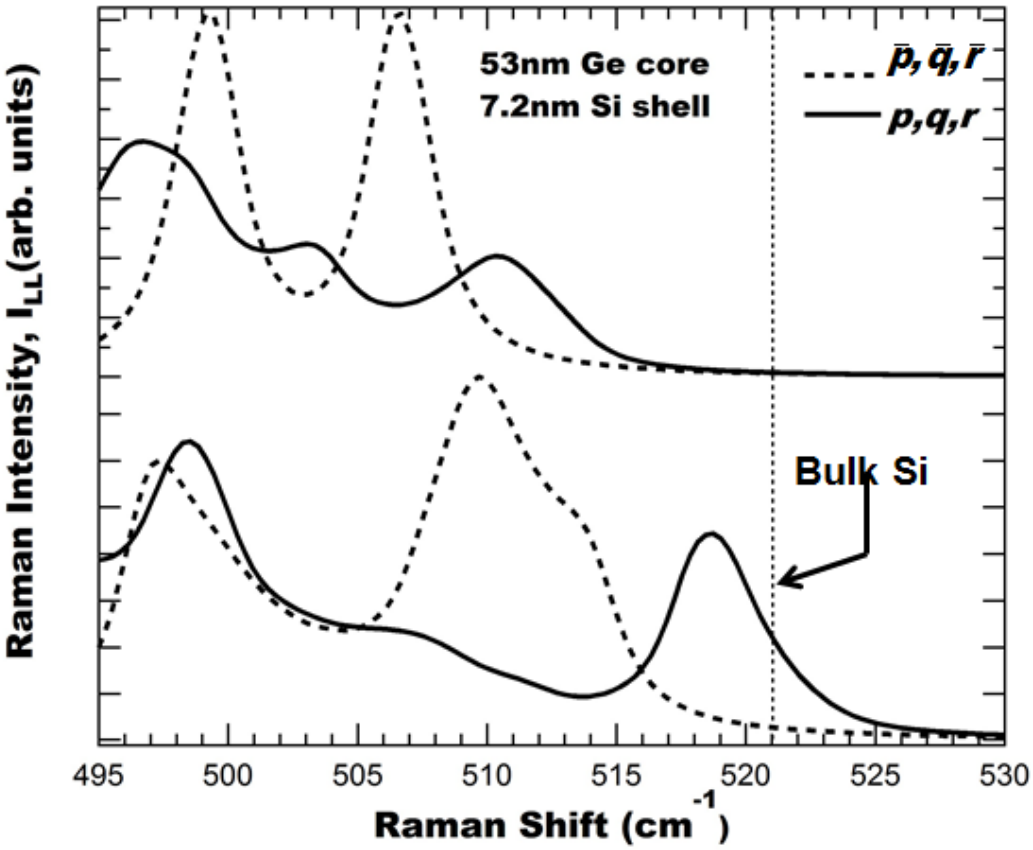

Figure A36 Calculated Raman spectra of the shell region of a <011> Ge-Si core-shell nanowire with D_{core} = 45 nm and t_{shell} = 9.1 nm, for incident and scattered light polarizations parallel to the nanowire axis. The top curves correspond to the analytical strain model with cylindrical geometry. The bottom curves correspond to the numerical strain calculation with realistic geometry. The spectra were calculated using either the full cubic p,q,r for Si from Table 5.1 (solid lines) or the Si Voigt-averaged tensor components from Eq. (5.6) (dotted lines). The latter are the same as in Fig. 5.4 and are shown here for easier comparison. All spectra are normalized to the same area. The vertical scale is the same in all panels. The vertical dotted line is the position of the Raman peak from bulk Si.

APPENDIX VI

GRAPHS FOR SHELL RAMAN SPECTRA IN

LT_1, T_1T_2, AND T_2T_2 POLARIZATIONS

Graphs of the Raman spectra of the shell region of a <011> Ge-Si core-shell nanowires are shown in Appendix VI. Incident and scattered light polarizations are indicated in the three different panels. The convention is L = <011>, T_1 = <100>, and $T_2 = <01\bar{1}>$. The top curves correspond to the analytical strain model with cylindrical geometry. The bottom curves correspond to the numerical strain calculation with realistic geometry. All spectra were calculated using cubic symmetry Si *p,q, r* phonon deformation potential tensor components from Table 5.I. All spectra are normalized to the same area. The vertical scale is the same in all panels. The vertical dotted line is the position of the Raman peak in bulk Si. The above instructions follow for all the graphs shown in Appendix VI.

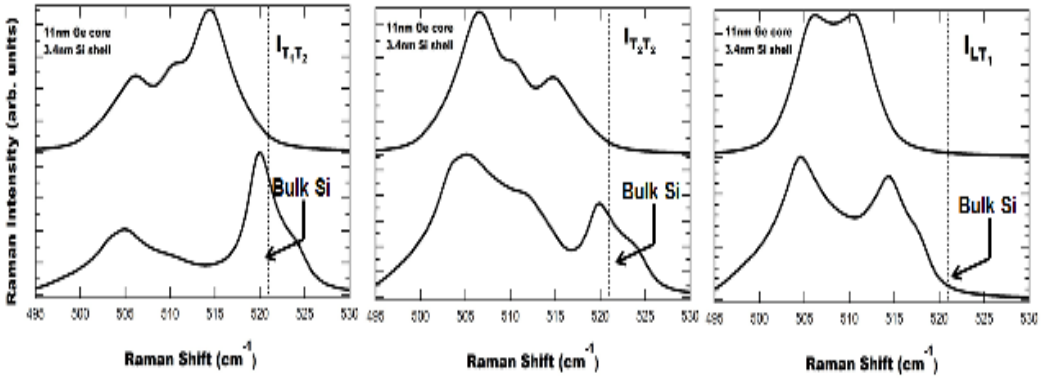

Figure A37 Calculated Raman spectra of the shell region of a <011> Ge-Si core-shell nanowire with D_{core} = 11 nm and t_{shell} = 3.4 nm. Incident and scattered light polarizations are indicated in the three different panels. The convention is L = <011>, T_1 = <100>, and $T_2 = <01\bar{1}>$.

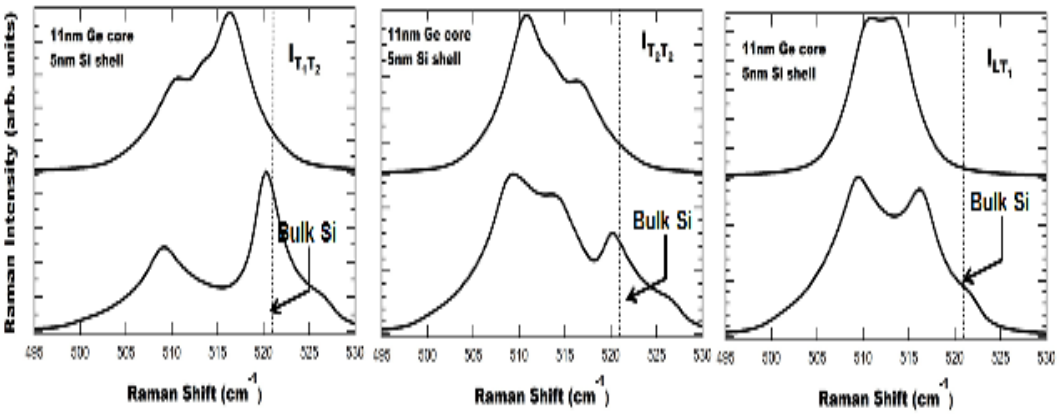

Figure A38 Calculated Raman spectra of the shell region of a <011> Ge-Si core-shell nanowire with D_{core} = 11 nm and t_{shell} = 5.0 nm. Incident and scattered light polarizations are indicated in the three different panels. The convention is L = <011>, T_1 = <100>, and T_2 = $< 01\bar{1} >$.

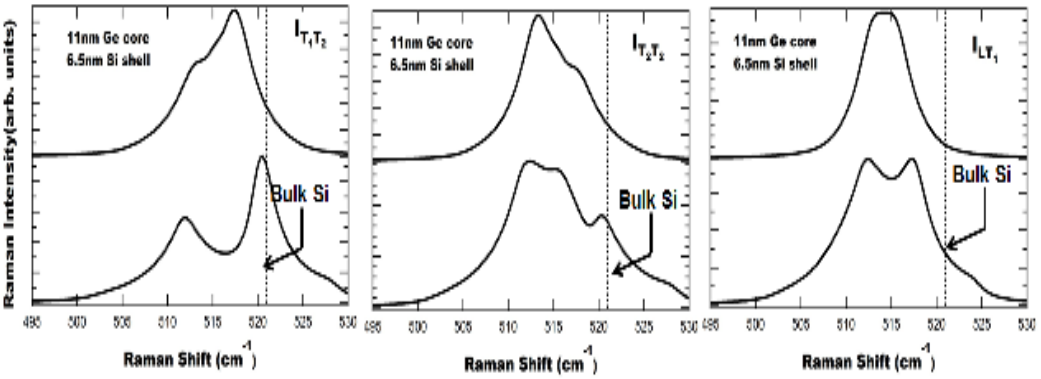

Figure A39 Calculated Raman spectra of the shell region of a <011> Ge-Si core-shell nanowire with D_{core} = 11 nm and t_{shell} = 6.5 nm. Incident and scattered light polarizations are indicated in the three different panels. The convention is L = <011>, T_1 = <100>, and T_2 = $< 01\bar{1} >$.

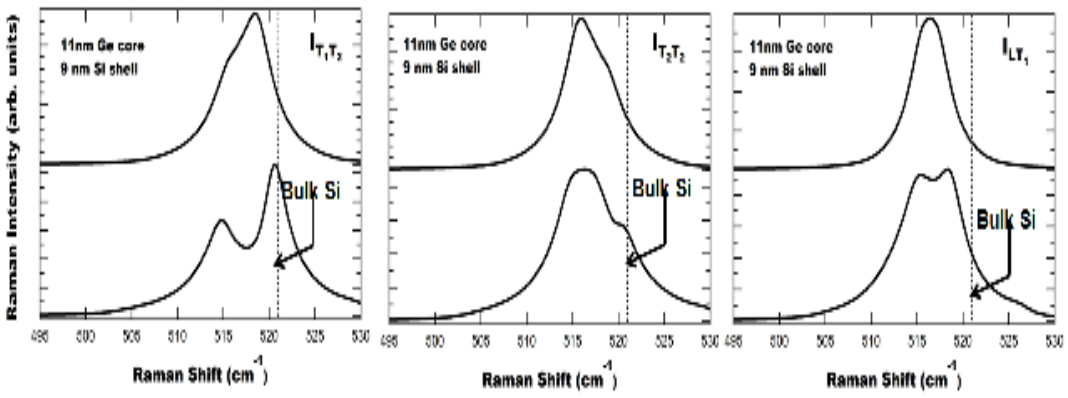

Figure A40 Calculated Raman spectra of the shell region of a <011> Ge-Si core-shell nanowire with D_{core} = 11 nm and t_{shell} = 9 nm. Incident and scattered light polarizations are indicated in the three different panels. The convention is L = <011>, T_1 = <100>, and $T_2 = < 01\bar{1} >$.

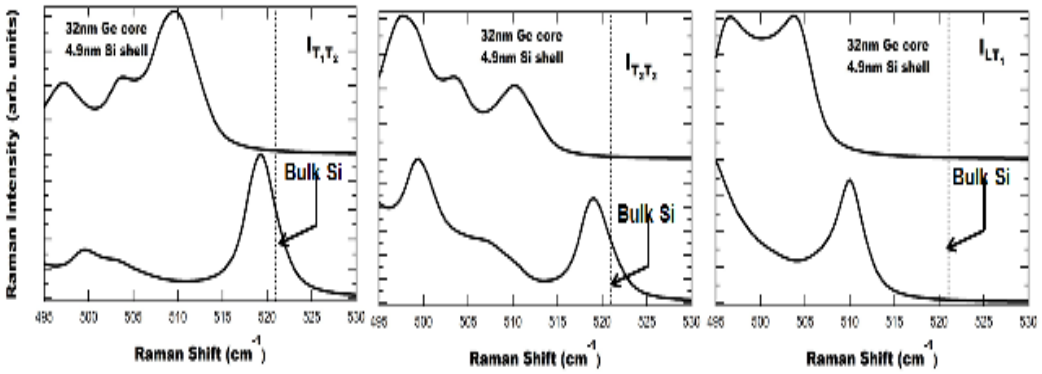

Figure A41 Calculated Raman spectra of the shell region of a <011> Ge-Si core-shell nanowire with D_{core} = 32 nm and t_{shell} = 4.9 nm. Incident and scattered light polarizations are indicated in the three different panels. The convention is L = <011>, T_1 = <100>, and $T_2 = < 01\bar{1} >$.

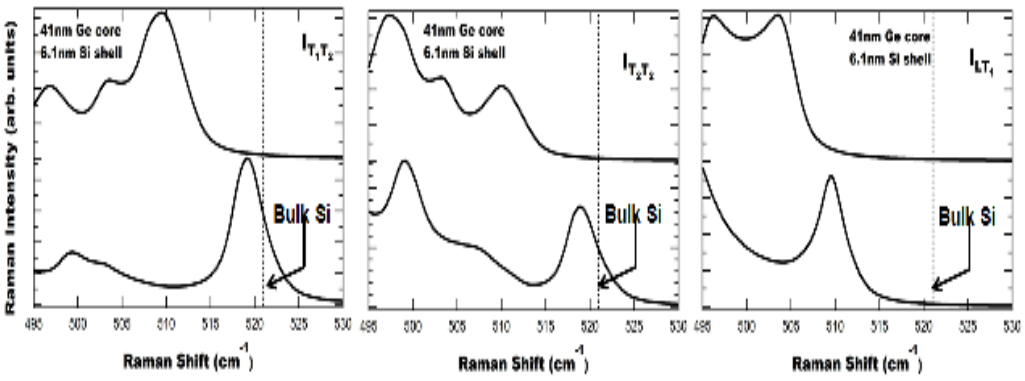

Figure A42 Calculated Raman spectra of the shell region of a <011> Ge-Si core-shell nanowire with D_{core} = 41 nm and t_{shell} = 6.1 nm. Incident and scattered light polarizations are indicated in the three different panels. The convention is L = <011>, T_1 = <100>, and $T_2 = < 01\bar{1} >$.

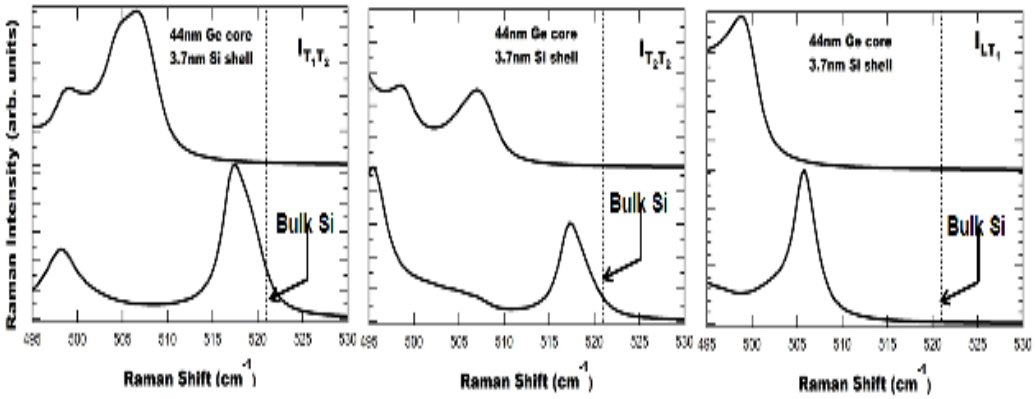

Figure A43 Calculated Raman spectra of the shell region of a <011> Ge-Si core-shell nanowire with D_{core} = 44 nm and t_{shell} = 3.7 nm. Incident and scattered light polarizations are indicated in the three different panels. The convention is L = <011>, T_1 = <100>, and $T_2 = < 01\bar{1} >$.

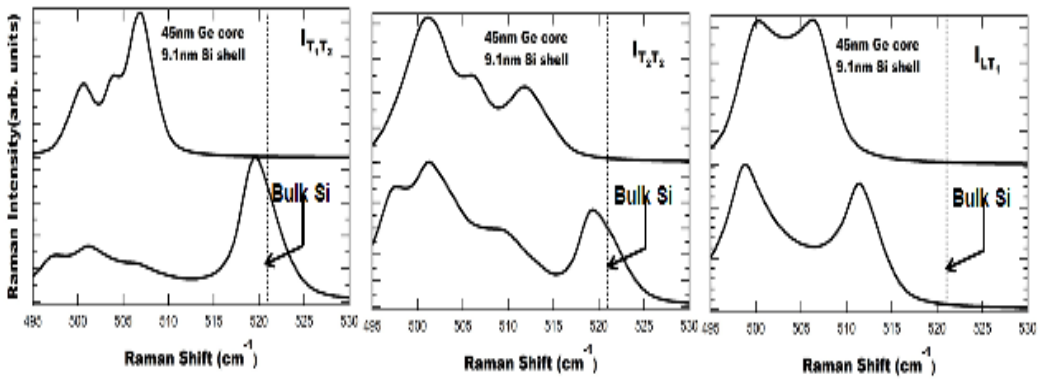

Figure A44 Calculated Raman spectra of the shell region of a <011> Ge-Si core-shell nanowire with D_{core} = 45 nm and t_{shell} = 9.1 nm. Incident and scattered light polarizations are indicated in the three different panels. The convention is L = <011>, T_1 = <100>, and $T_2 = < 01\bar{1} >$.

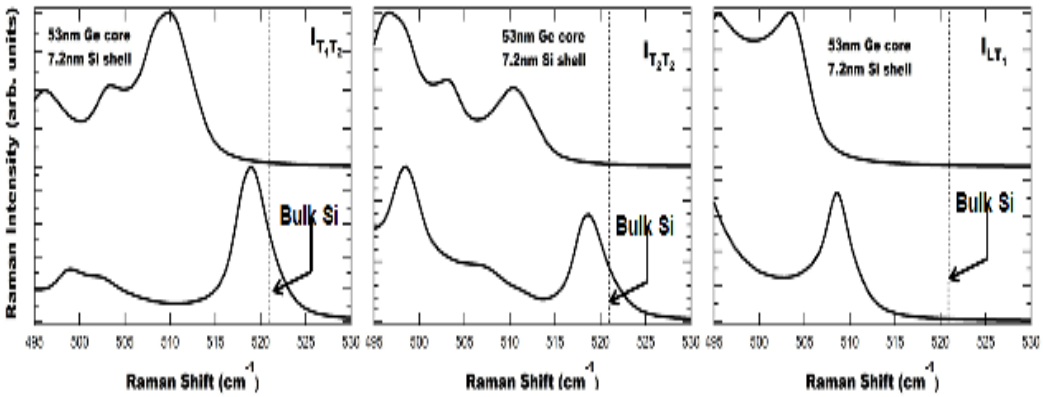

Figure A45 Calculated Raman spectra of the shell region of a <011> Ge-Si core-shell nanowire with D_{core} = 53 nm and t_{shell} = 7.2 nm. Incident and scattered light polarizations are indicated in the three different panels. The convention is L = <011>, T_1 = <100>, and $T_2 = < 01\bar{1} >$.